Classical and Quantum Gravity

PAPER • **OPEN ACCESS**

Characterizing gravitational wave detector networks: from A♯ to cosmic explorer

To cite this article: Ish Gupta *et al* 2024 *Class. Quantum Grav.* **41** 245001

OPEN ACCESS
IOP Publishing
Classical and Quantum Gravity
Class. Quantum Grav. **41** (2024) 245001 (68pp) https://doi.org/10.1088/1361-6382/ad7b99

Characterizing gravitational wave detector networks: from A♯ to cosmic explorer

Ish Gupta[1,*], Chaitanya Afle[2], K G Arun[1,3], Ananya Bandopadhyay[2], Masha Baryakhtar[4], Sylvia Biscoveanu[5], Ssohrab Borhanian[6], Floor Broekgaarden[7], Alessandra Corsi[8], Arnab Dhani[9], Matthew Evans[5], Evan D Hall[5], Otto A Hannuksela[10], Keisi Kacanja[2], Rahul Kashyap[1], Sanika Khadkikar[1], Kevin Kuns[5], Tjonnie G F Li[11,12], Andrew L Miller[13,14], Alexander Harvey Nitz[2], Benjamin J Owen[8], Cristiano Palomba[15], Anthony Pearce[8], Hemantakumar Phurailatpam[10], Binod Rajbhandari[8], Jocelyn Read[16], Joseph D Romano[8], Bangalore S Sathyaprakash[1,17], David H Shoemaker[5], Divya Singh[1], Salvatore Vitale[5], Lisa Barsotti[5], Emanuele Berti[18], Craig Cahillane[2], Hsin-Yu Chen[19], Peter Fritschel[5], Carl-Johan Haster[20], Philippe Landry[21], Geoffrey Lovelace[16], David McClelland[22], Bram J J Slagmolen[22], Joshua R Smith[16], Marcelle Soares-Santos[23], Ling Sun[22], David Tanner[24], Hiro Yamamoto[25] and Michael Zucker[5,25]

[1] Institute for Gravitation and the Cosmos, Department of Physics, Pennsylvania State University, University Park, PA 16802, United States of America
[2] Department of Physics, Syracuse University, Syracuse, NY 13244, United States of America
[3] Chennai Mathematical Institute, Chennai, India
[4] Department of Physics, University of Washington, Seattle, WA 98195, United States of America
[5] LIGO Laboratory, Massachusetts Institute of Technology, Cambridge, MA 02139, United States of America
[6] Theoretisch-Physikalisches Institut, Friedrich-Schiller-Universität Jena, Jena 07743, Germany

[*] Author to whom any correspondence should be addressed.

[7] Center for Astrophysics, Harvard & Smithsonian, Cambridge, MA 02138, United States of America
[8] Department of Physics and Astronomy, Texas Tech University, Lubbock, TX 79409, United States of America
[9] Max Planck Institute for Gravitational Physics (Albert Einstein Institute), Potsdam 14476, Germany
[10] Department of Physics, The Chinese University of Hong Kong, Shatin, New Territories, Hong Kong Special Administrative Region of China, People's Republic of China
[11] Department of Physics and Astronomy, Institute for Theoretical Physics, KU Leuven, B-3001 Leuven, Belgium
[12] Department of Electrical Engineering (ESAT), STADIUS, KU Leuven, B-3001 Leuven, Belgium
[13] Nikhef—National Institute for Subatomic Physics, 1098 XG Amsterdam, The Netherlands
[14] Institute for Gravitational and Subatomic Physics, Utrecht University, 3584 CC Utrecht, The Netherlands
[15] INFN, Sezione di Roma, I-00185 Roma, Italy
[16] Nicholas and Lee Begovich Center for Gravitational Wave Physics and Astronomy, California State University Fullerton, Fullerton, CA 92831, United States of America
[17] Gravity Exploration Institute, School of Physics and Astronomy, Cardiff University, Cardiff CF24 3AA, United Kingdom
[18] Department of Physics and Astronomy, Johns Hopkins University, Baltimore, MD 21218, United States of America
[19] Department of Physics, The University of Texas at Austin, Austin, TX 78712, United States of America
[20] Department of Physics and Astronomy, University of Nevada Las Vegas, Las Vegas, NV 89154, United States of America
[21] Canadian Institute for Theoretical Astrophysics, University of Toronto, Toronto, ON M5S 3H8, Canada
[22] OzGrav-ANU, Centre for Gravitational Astrophysics, College of Science, The Australian National University, Canberra ACT 2601, Australia
[23] Department of Physics, University of Michigan, Ann Arbor, MI 48109, United States of America
[24] Department of Physics, University of Florida, Gainesville, FL 32611, United States of America
[25] LIGO Laboratory, California Institute of Technology, Pasadena, CA 91125, United States of America

E-mail: ishgupta@psu.edu

Received 4 February 2024; revised 5 June 2024
Accepted for publication 16 September 2024
Published 8 November 2024

Abstract

Gravitational-wave observations by the laser interferometer gravitational-wave observatory (LIGO) and Virgo have provided us a new tool to explore the Universe on all scales from nuclear physics to the cosmos and have the massive potential to further impact fundamental physics, astrophysics, and cosmology for decades to come. In this paper we have studied the science capabilities of

a network of LIGO detectors when they reach their best possible sensitivity, called A$^\sharp$, given the infrastructure in which they exist and a new generation of observatories that are factor of 10 to 100 times more sensitive (depending on the frequency), in particular a pair of L-shaped cosmic explorer (CE) observatories (one 40 km and one 20 km arm length) in the US and the triangular Einstein telescope with 10 km arms in Europe. We use a set of science metrics derived from the top priorities of several funding agencies to characterize the science capabilities of different networks. The presence of one or two A$^\sharp$ observatories in a network containing two or one next generation observatories, respectively, will provide good localization capabilities for facilitating multimessenger astronomy (MMA) and precision measurement of the Hubble parameter. Two CE observatories are indispensable for achieving precise localization of binary neutron star events, facilitating detection of electromagnetic counterparts and transforming MMA. Their combined operation is even more important in the detection and localization of high-redshift sources, such as binary neutron stars, beyond the star-formation peak, and primordial black hole mergers, which may occur roughly 100 million years after the Big Bang. The addition of the Einstein Telescope to a network of two CE observatories is critical for accomplishing all the identified science metrics including the nuclear equation of state, cosmological parameters, the growth of black holes through cosmic history, but also make new discoveries such as the presence of dark matter within or around neutron stars and black holes, continuous gravitational waves from rotating neutron stars, transient signals from supernovae, and the production of stellar-mass black holes in the early Universe. For most metrics the triple network of next generation terrestrial observatories are a factor 100 better than what can be accomplished by a network of three A$^\sharp$ observatories.

Keywords: cosmic explorer, Einstein telescope, gravitational waves, next generation

Contents

1. Introduction

Over the past eight years since their first discovery, the laser interferometer gravitational-wave observatory [1] (LIGO) in the U.S. and the Virgo observatory [2] in Europe have observed $\sim\mathcal{O}(100)$ binary black hole (BBH) mergers and a handful of neutron star binary mergers [3] during the first three science runs O1-O3. The fourth science run (O4, Advanced LIGO and Virgo sensitivity [1]) and the fifth (O5, A+ sensitivity [4]) over the next two to seven years will add hundreds more to the catalog of compact binary coalescences. LIGO and Virgo will eventually be joined by KAGRA [5] and LIGO-India [6] to make many more detections and discoveries. These detections will enable electromagnetic (EM) follow-up observations,

multi-messenger astronomy, compact binary population inferences, ultra-dense matter phenomenology and cosmological studies.

The LIGO and Virgo collaborations have already developed plans for further improvements in sensitivity beyond O5 that will fully exploit what is possible at existing facilities. In particular, the A$^\sharp$ (pronounced A-sharp) concept [7] is expected to improve the sensitivity by a factor of two compared to A+ strain sensitivity [4]. Accomplishing sensitivity levels significantly greater than those currently envisaged will require new facilities, with longer interferometer arms, but marginal improvements in detector technology, as described in the NSF-funded Horizon Study [8] for the cosmic explorer (CE) project[26]. Einstein telescope (ET) is a similar concept currently considered for funding in Europe [9–12]. We shall refer to CE and ET as next-generation observatories or XG for short.

The National Science Foundation (NSF) has appointed a sub-committee[27] of the Mathematical and Physical Sciences Advisory Committee (MPSAC) to *assess and recommend configurations for a U.S. GW detection network that can operate at a sensitivity approximately an order of magnitude greater than that of LIGO A+ by the middle of the next decade*[27]. The sub-committee has invited White Papers from the community addressing *science motivation and key science objectives, technical description of the proposed concept(s) and how different aspects are associated with key science, current and new technologies needed, risks, timelines, and approximate cost assessment, any synergies or dependencies on other multi-messenger facilities (existing or future)*[28]. The CE project conducted a trade study to assess the relative performances of plausible detector networks operating in the 2030 s and summarized the findings in the White paper [13] (hereby referred to as the WP) submitted in response to that call. The present document provides the details of the trade study including the populations considered, the methodology used, and the results obtained. It serves as the technical basis for what is reported in the project's submission.

Gravitational-wave (GW) observations can address questions across multiple disciplines from general relativity to relativistic astrophysics, nuclear physics to dark matter searches and cosmology to beyond the standard model of particle physics. They can do this by observing BBH coalescences from an epoch when the Universe was still assembling its first stars, binary neutron stars (BNSs) far beyond redshifts when the star formation in the Universe was at its peak, stochastic backgrounds produced in the primordial Universe, new sources and phenomena such as supernovae, stellar quakes and rapidly rotating neutron stars and, very likely, new phenomena and sources not imagined by anyone so far. To realize the full potential of GW astronomy, it is necessary to build longer detectors with sensitivity levels that are at least an order of magnitude better than those of A+ detectors. In this tech report, we describe the science that can be accomplished at the limit of current facilities and how future observatories like CE can vastly transform the field of GW astronomy, while answering many of the pressing problems in high-energy physics, astronomy and cosmology.

To this end, we consider eight different networks, described in section 2 and summarized in table 3, each consisting of three observatories belonging to one of four classes: **0 XG:** three A$^\sharp$ LIGO detectors, two in the US and one in India (HLA), **1 XG:** two A$^\sharp$ LIGO detectors, in the US or India, and one CE observatory of 40 km or 20 km arm-length (HLET, 20LA, 40LA) **2 XG:** one A$^\sharp$ LIGO detector in the US together with two next generation observatories

[26] Visit the CE project website https://dcc.ligo.org/LIGO-T2200287/public for news and sensitivity curves.

[27] Membership of the sub-committee can be found at www.nsf.gov/mps/phy/nggw-members.jsp and NSF's charge to the sub-committee is at: www.nsf.gov/mps/advisory/subcommittee_charges/mpsac-nggw-charge_signed.pdf.

[28] The call for White Papers can be found at www.nsf.gov/mps/phy/nggw/WhitePaperCall2.pdf.

(20LET, 40LET, 2040A), or **3 XG:** three next generation observatories (4020ET). The results of the trade study are summarized in table 1, listed under the five key science themes that are discussed at length in section 5. Our study concludes that *a network of three next generation observatories composed of a 40 km arm-length CE, a 20 km arm-length CE and a 10 km a side ET triangle is two orders-of-magnitude better than the planned A+ network in respect of almost every metric considered in this study.* More precisely, for most metrics the numbers in the last column of table 1 for a network 3 XG observatories are a factor 100 better than those in the second column corresponding to a network of 3 A$^\sharp$ observatories. A brief account of our findings is given below.

1.1. Black holes and neutron stars throughout cosmic time

A network of XG observatories will build a survey of black hole mergers from epochs before the Universe was assembling its first stars and observe double neutron star mergers and neutron star-black hole (NSBH) mergers far beyond redshifts when the star formation rate was at its peak. Four key metrics for this theme are listed in table 1. In particular, a network consisting of at least one XG observatory will observe hundreds of black hole mergers at $z > 10$, but a network consisting of at least two XG observatories is necessary to observe BBHs at $z > 10$ and definitively say if a sub-population exists at those redshifts. Similarly, a network of two XG observatories is key to observing neutron star mergers at $z > 1$ and measuring their masses accurately enough to conclude that they are neutron stars. Moreover, XG observatories have the unique opportunity to detect intermediate-mass black hole binaries up to $z\sim5$, accurately measure their mass- and redshift-distribution.

1.2. Multimessenger astrophysics and dynamics of dense matter

Mergers of double neutron star and NSBH binaries involve dense matter in relativistic motion and observing them in the EM window will require accurate 3D localization and alerts from GW observatories. Seven rows in table 1 illustrate the power of XG observatories in accomplishing all the science goals under this theme. Golden BNS mergers such as GW170817 would be observed with a signal-to-noise ratio (SNR) $> 10^3$ several times a year. Several tens of high-fidelity signals will be localized to $\Delta\Omega < 1\,\mathrm{deg}^2$, enabling deeper insight into the physics r-process kilonova, tens of thousands will be localized to within $10\,\mathrm{deg}^2$ to study jet afterglows produced by merger remnants and hundreds will be detected and localized to within $100\,\mathrm{deg}^2$ 10 min before merger, providing pre-merger alerts for EM follow-up. Tens of thousands of events will be localized to within $100\,\mathrm{deg}^2$ at $z > 2$ providing an opportunity to correlate every short gamma-ray burst (GRBs) with BNS mergers. Finally, hundreds of high-fidelity signals will enable precision measurement of the neutron star radius and the equation of state (EoS) of dense matter.

1.3. New probes of extreme astrophysics

Next generation observatories will not be limited to observing just compact binary mergers. They will detect new classes of transient signals, e.g. from core-collapse supernovae and magnetar flares to continuous waves from rapidly rotating pulsars. We expect the network of 3 XG observatories to detect 20 pulsars with ellipticities of 10^{-9} or smaller and detect 25 pulsars in less than 2 years. The A$^\sharp$ network will detect a handful of such signals in several years of operation. Continuous waves from neutron stars would provide first hints of the physics of

Table 1. Comparison of eight different detector networks against five key science goals defined in the text. The comparison uses several metrics defined in column 1 for each science goal, followed by what's accomplished by each network in eight columns corresponding to the eight networks considered in this study (see, table 3). Each network has 3 observatories and falls into one of four classes: 0 next generation observatories in column 2, 1 such observatory in columns 3–5, two such observatories in columns 6-8 and three such observatories in column 9. Networks that contain 2 or fewer XG observatories are populated with one or more A$^\sharp$ observatories. We choose a network signal-to-noise ratio (SNR) of 10 as the cut-off for confident detection. The yearly rates mentioned in the table (and referred to in this work) correspond to calendar times scaled by the inverse of the duty cycle of the studied network. If the duty cycle achieved by a network is 50%, then a year of observation for that network will correspond to two calendar years.

	Network Performance							
	0 XG	1 XG			2 XG			3 XG
Science Goal Requirements	HLA	HLET	20LA	40LA	20LET	40LET	4020A	4020ET
BHs and NSs throughout cosmic time								
Measure mass function, determine formation scenarios:								
$N_{\rm BNS}$/yr, $z \geqslant 1$, $\delta z/z \leqslant 0.2$, $\delta m_1/m_1 \leqslant 0.3$	0	0	0	0	0	7	22	81
Detect the (injected) second Gaussian feature:								
$N_{\rm BNS}$/yr, $m_1 \geqslant 1.5\,{\rm M}_\odot$, $\delta m_1/m_1 \leqslant 0.1$	0	37	9	24	68	105	58	155
Unveiling the elusive population of IMBH:								
$N_{\rm IMBBH}$/yr, $z \geqslant 3$, $\delta z/z \leqslant 0.2$, $\delta m_1/m_1 \leqslant 0.2$	6	430	150	190	840	870	510	890
High-z BBH formation channels and mass function:								
$N_{\rm BBH}$/yr $z \geqslant 10$, $\delta z/z \leqslant 0.2$ $\delta m_1/m_1 \leqslant 0.2$	0	12	6	35	65	140	110	230
MMA and dynamics of dense matter								
GW170817-like golden sample:								
$N_{\rm BNS}$/yr $z \leqslant 0.06$, $\Delta\Omega \leqslant 0.1\,{\rm deg}^2$	0	0	0	0	0	1	1	7
r-process and kilonova-triggered follow up:								
$N_{\rm BNS}$, $0.06 < z \leqslant 0.1$, $\Delta\Omega \leqslant 1\,{\rm deg}^2$	1	8	6	6	26	47	32	71
Jet afterglows, large-FOVs or small-FOV mosaicking:								
$N_{\rm BNS}$/yr, $0.1 < z \leqslant 2$, $\Delta\Omega \leqslant 10\,{\rm deg}^2$	260	1000	780	890	6000	9200	3900	27 000
Mapping GRBs to progenitors up to star-formation peak:								
$N_{\rm BNS}$/yr, $z > 2$, $\Delta\Omega \leqslant 100\,{\rm deg}^2$	0	2	19	37	6200	25 000	3700	66 000
Pre-merger alerts 10 min before merger								
$N_{\rm BNS}$/yr, $\Delta\Omega \leqslant 100\,{\rm deg}^2$	0	20	0	0	200	400	200	700

(Continued.)

Table 1. (Continued.)

	Network Performance							
	0 XG	1 XG			2 XG			3 XG
Science Goal Requirements	HLA	HLET	20LA	40LA	20LET	40LET	4020A	4020ET
NS EoS constraints:								
$N_{\rm BNS}$/yr, SNR$\geqslant 100$	0	48	39	220	120	350	350	480
$N_{\rm BNS}$/yr, $\Delta R < 0.1$ km	0	160	20	72	280	450	320	740
New Probes of Extreme Astrophysics								
Pulsars with ellipticity 10^{-9} detectable in 1 year	1	3	3	5	5	11	9	21
Years to detect 25 pulsars with ellipticity 10^{-9}	12	3.5	3.7	2.3	2.2	1.7	1.7	1.3
Fundamental physics and precision cosmology								
Constrain graviton mass:								
$N_{\rm BNS}$/yr, $z \geqslant 5$	0	0	0	84	0	340	580	880
$N_{\rm BBH}$/yr, $z \geqslant 5$	19	2500	2200	3900	3880	4700	4500	5100
Probing rare events:								
$N_{\rm BBH}$/yr, SNR > 100	17	1900	1300	5000	3700	7500	6900	9500
$N_{\rm BBH}$/yr, SNR > 1000	1	2	1	5	4	7	7	10
Precision tests of GR (IMR and QNM):								
BBH root sum square total SNR	2400	11 000	9800	16 000	15 000	20 000	19 000	22 000
BBH root sum square post-inspiral SNR	1900	5800	5300	8100	7800	9900	9500	11 000
$N_{\rm BBH}$/yr, post-inspiral SNR > 100	6	319	290	1200	790	1900	1700	2500

(Continued.)

Table 1. (Continued.)

Cosmology and tests of GR:								
$N_{\rm BNS}$/yr, $z \leqslant 0.5$, $\delta d_L/d_L \leqslant 0.1$ and $\Delta\Omega \leqslant 10\,{\rm deg}^2$	14	270	63	71	1100	1600	790	4800
$N_{\rm BBH}$/yr, $\delta d_L/d_L \leqslant 0.1$, $\Delta\Omega \leqslant 1\,{\rm deg}^2$	69	490	290	350	2200	3300	1300	6800
Lensed BNS events/yr:	1	25	11	65	47	91	87	110
Physics beyond the standard model								
Stochastic signal $\Omega_{\rm GWBG}$ in units of 10^{-10}	2	0.03	0.5	0.3	0.03	0.02	0.06	0.02
Dark matter assisted NS implosions:$N_{\rm BBH}$/yr	0	2000	1200	4600	4200	8000	6300	9700
Primordial black hole mergers: $N_{\rm pBBH}$/yr, $z > 25$, $\Delta z/z < 0.2$:	0	0	0	0	8	17	3	28
Pop III black hole mergers $z > 10$, $\Delta z/z < 0.1$: $N_{\rm PopIII}$/yr:	0	2	0	9	38	110	74	360
Max distance (Mpc) to detectable axion clouds in BHs	0.13	0.73	0.82	1.34	0.60	1.60	1.87	1.66

neutron-star crust and an independent (from binary mergers) confirmation of the EoS of cold dense matter.

1.4. Fundamental physics and precision cosmology

General relativity has been a highly successful theory in explaining laboratory experiments and astronomical observations. Yet, due to some of its conceptual problems (e.g. the black hole singularity and the information paradox), it is largely expected that the theory will prove to be incompatible with high-precision observations of black holes and neutron stars in the era of XG observatories. Signals from BNSs and black holes at redshifts larger than 5 will help constrain massive graviton and other theories that require GWs to travel at sub- or super-luminal speeds. Thousands of BBH events with SNR >100 and cumulative SNRs of more than 20 000 from the entire population of observed BBH mergers in a network of 2 XG observatories will subject general relativity to stringent tests.

Binary coalescences are standard sirens allowing precision measurement of the luminosity distance to sources. Thousands of well-localized BBHs and neutron stars will allow exquisite measurement of the Hubble constant and other cosmological parameters.

1.5. Physics beyond the standard model

The standard model of particle physics is in excellent agreement with results from the collider experiments and yet there are several conceptual problems, e.g. strong CP problem and QCD axions, which seem to suggest physics beyond the standard model. Gravitational observations could discover the presence of axion clouds around black holes affecting their spin distributions or the accumulation of weakly interacting massive particles in neutron stars converting them to black holes. A network of XG observatories will provide direct or indirect evidence of the existence of dark matter, probe the nature of dark energy and either detect or set stringent limits on the stochastic backgrounds from the early Universe such as the electroweak phase transition or cosmic strings. Next generation observatories are sensitive to energy density in stochastic backgrounds and could detect them with $SNR > 3$ at a fiducial frequency of $f_{\rm ref} = 25\,\mathrm{Hz}$ if $\Omega_{\rm GWBG} \geqslant 10^{-12}$.

A network of two CE observatories will herald a remarkable enhancement in sensitivity, surpassing A$^\sharp$ detectors by approximately an order of magnitude, especially at frequencies below 100 Hz. Individually, in a network with A$^\sharp$ detectors, they can detect the majority of the cosmic population of BBH mergers and $\mathcal{O}(10^5)$ BNS and NSBH mergers every year. The 20 km detector can be optimized to measure the post-merger signal from BNSs, which will reveal useful insights into the physical processes involved in the dynamically evolving post-merger remnant [14]. However, the true scientific potential is realized through the synergistic capabilities of both observatories, proving pivotal in realizing the objectives outlined in table 1. A network with both the 20 km and 40 km observatories will not only prove indispensable in measuring the mass spectrum of BNS systems, it will also enable precise sky-localization of BNS mergers, facilitating detection of multi-band EM counterparts, which is the cornerstone of multimessenger astronomy (MMA). Such a network will also have the capability to impose stringent constraints on the EoS of dense matter, by achieving sub-100 m precision in measuring the neutron star radius for dozens of events annually. Additionally, the ability to detect signals from high-redshift GW sources, e.g. primordial black holes that are detectable at redshifts surpassing 25, underscores the vital role played by the two CE observatories in advancing our understanding of the cosmos across diverse cosmic epochs.

The rest of the paper is organized as follows. In section 2 we introduce the list of observatories considered in this study and their strain sensitivity and networks composed of those observatories. Section 3 provides the assumptions we make about the cosmic population of binary sources. This is followed by a discussion of the Fisher information matrix approach followed in this study in section 4. This section relies on a number of tables and figures to illustrate the detection and measurement capabilities of different detector networks. Finally, in section 5 we provide a detailed account of the science questions that are of broad interest and how A$^\sharp$ and future XG observatories can probe those questions.

2. GW observatory network configurations

In this section, we summarize the list of GW detectors that are expected to be available over the next two decades. We start with detectors with the best sensitivities that could be installed in LIGO facilities, followed by networks that include one or more XG observatories consisting of CE and/or ET. The collection of network configurations studied is intended to be sufficiently broad without being unduly complex: broad enough to gauge all plausible network configurations but not so complex as to consider every possible scenario. Indeed, we are aided by research indicating that the critical feature of a future GW network is the number of next-generation detectors present for most of the science metrics, while their locations are of secondary importance [15]. For the localization metrics, however, the network area has a large effect on the performance, once the network composition is optimized. To this end, we consider the following observatories:

2.1. CE observatories (CE-A, CE-B)

Since the locations of the CE observatories have yet to be determined, we selected two fiducial locations for CE; CE-A off the coast of Washington state, and CE-B off the coast of Texas. These locations are intentionally unphysical to avoid impacting our ability to find a potential home for CE, but close enough to a wide range of potential sites to be representative from the point of view of GW science (see table 2). The CE-A location is considered in both the 40 km and the 20 km lengths, while the CE-B location hosts only a 20 km observatory. The strain sensitivity of the two choices is shown in figure 1.

2.2. Existing LIGO sites (LHO, LLO, LAO)

In order to focus on the science enabled by CE beyond what is possible in the current facilities, we model the LIGO detectors in an upgraded form (known as 'A$^\sharp$', [7], and essentially equivalent in sensitivity to 'Voyager' [26]) that approximately represents the limit to what is achievable in the LIGO facilities. Furthermore, in addition to the LIGO Hanford (LHO) and LIGO Livingston (LLO) detectors, we also consider LIGO Aundha (LAO) at A$^\sharp$ sensitivity, as it is expected to be operational starting in the early 2030 s. The currently projected strain sensitivity of A$^\sharp$ is shown in figure 1.

2.3. ET

The ET is a planned next-generation GW observatory in Europe [9]. It is currently envisioned as an underground triangular facility with 10 km arm length, housing six interferometers (however, other configurations and their scientific potentials have also been studied in [27]). The targeted timeline calls for first observations by the mid-2030 s. The underground location,

Table 2. Position and orientation of the detectors. Latitudes (Longitudes) are positive in the northern hemisphere (East of the Greenwich meridian). The orientation is the angle north of east of the x-arm (Note: here we follow the same convention used in Bilby [16–18], which is different from what is used in [19, 20], where the orientations of the detectors are clockwise rotations from the local north). For L-shaped detectors, the x-arm is defined as the one that completes a right-handed coordinate system together with the other arm and the local, outward, vertical direction. For ET, the x-arm is defined such that the two other arms lay westward of it.

Detector	Latitude	Longitude	Orientation
CE-A	$46°00'00''$	$-125°00'00''$	$260.0°$
CE-B	$29°00'00''$	$-94°00'00''$	$200.0°$
ET	$40°31'00''$	$+9°25'00''$	$90.0°$
LLO	$30°33'46.4196''$	$-90°46'27.2654''$	$197.7165°$
LHO	$46°27'18.5280''$	$-119°24'27.5657''$	$125.9994°$
LAO	$19°36'47.9017''$	$+77°01'51.0997''$	$117.6157°$

Table 3. We consider four classes of networks containing, zero to three next-generation (XG) observatories. Each network is given a name to facilitate comparisons. The HLA network sets the stage, representing the baseline from which CE return on investment can be assessed. 20LA and 40LA represent a single CE operating in the context of an upgraded 2G network while HLET is a single ET operating together with LLO and LHO. 4020A is the CE reference configuration, operating with an A$^\sharp$ LIGO Aundha, while 20LET and 40LET represent a single CE operating with LLO and ET. 4020ET is the reference CE configuration operating with ET. Reproduced with permission from [13].

Number of XG Observatories	Network Name	Detectors in the network
None	HLA	LHO, LLO, LAO
1 XG	HLET	LHO, LLO, ET
	20LA	CE-A 20 km, LLO, LAO
	40LA	CE-A 40 km, LLO, LAO
2 XG	4020A	CE-A 40 km, CE-B 20 km, LAO
	40LET	CE-A 40 km, LLO, ET
	20LET	CE-A 20 km, LLO, ET
3 XG	4020ET	CE-A 40 km, CE-B 20 km, ET

which is strongly preferred in Europe, suppresses the expected seismic disturbances, thereby reducing the Newtonian noise that limits terrestrial GW facilities a low frequencies (c.f. the difference between CE and ET below 8 Hz is depicted in figure 1).

ET's adoption into the European Strategy Forum on Research Infrastructure (ESFRI) road map has affirmed the observatory's role in the future of GW physics astronomy. Nevertheless, we present network configurations that do not include ET to inform the value of US investment in the absence of ET. Our models for each of these network nodes are described below and shown in table 3.

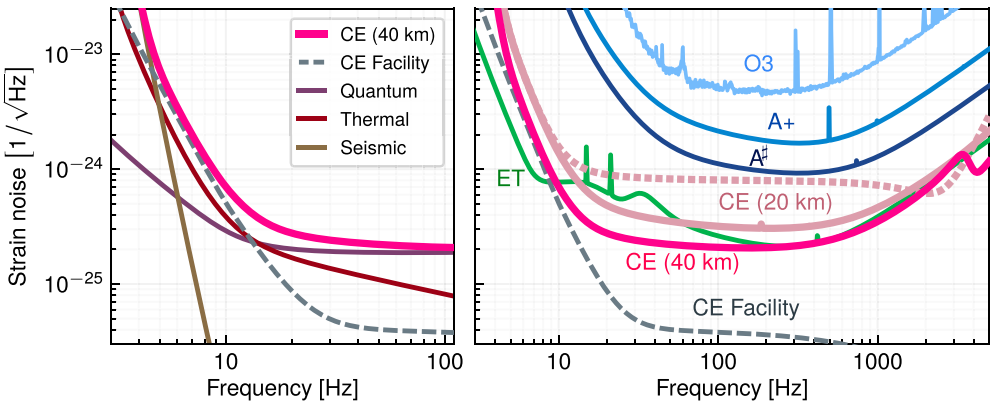

Figure 1. *Left:* estimated spectral sensitivity (solid black) of cosmic explorer (CE) and the known fundamental sources of noise that contribute to this total (other curves). *Right:* comparison of spectral sensitivities of O3 [21], LIGO A+ [22], LIGO A$^\sharp$ [23], Einstein Telescope [24] (a triangular arrangement of six interferometric detectors), and 20 km and 40 km versions of cosmic explorer [25]. The facility limit for cosmic explorer is also indicated. (Reproduced from the WP). Reproduced with permission from [13].

3. Population of compact binaries

3.1. BBHs

To analyze the science capabilities of the different detector network configurations, we simulate populations of various types of compact binary mergers and evaluate the detection and measurement abilities of the networks for these populations. There are still large uncertainties in the properties that characterize these populations due to the low number of detections at present. Therefore, the populations we described below are intended to represent plausible, but not necessarily exact, realizations of the true populations. This is sufficient for the purposes of this work as our goal is not to predict the actual detection rates but, instead, to compare the capabilities of different networks for the chosen populations.

3.1.1. Local population. The local population of BBH mergers is consistent with what has been inferred up to GWTC-3 [3, 28]. One difference is that we do not consider precession for any of the populations. As precession, in general, is expected to improve the estimation of parameters [29], the measurability estimates presented in this work will be on the conservative side. Specifically, for the local population we use:

- **Primary mass**: `POWER LAW + PEAK` [28] model with the following values for the model parameters: $\alpha = -3.4$, $m_{\rm min} = 5\,{\rm M}_\odot$, $m_{\rm max} = 87\,{\rm M}_\odot$, $\lambda = 0.04$, $\mu_{\rm peak} = 34\,{\rm M}_\odot$, $\sigma_{\rm peak} = 3.6$, $\delta_m = 4.8\,{\rm M}_\odot$.
- **Mass ratio**: $p(q) \propto q^\beta$ with $\beta = 1.1$, and enforcing $m_{\rm min} = 5\,{\rm M}_\odot$.
- **Spin magnitude**: independently and identically distributed (IID) spins following a beta distribution (see, e.g. [30]) with $\alpha_\chi = 2$, $\beta_\chi = 5$ (see equation (10) in [30]), but restricted to aligned spins.

- **Redshift**: merger rate following the Madau–Dickinson star formation rate [31, 32],

$$\psi\left(z|\gamma,\kappa,z_p\right)=\frac{(1+z)^{\gamma}}{1+\left(\frac{1+z}{1+z_p}\right)^{\kappa}}, \tag{1}$$

  with $\gamma=2.7$, $z_p=1.9$, and $\kappa=5.6$. We choose a local merger rate density of $24\,\mathrm{Gpc}^{-3}\,\mathrm{yr}^{-1}$ [33].

3.1.2. Population III black holes. We also consider a population of high-redshift BBHs, representing BBHs formed from Pop-III stars. As no uncontroversial detection of these objects exists, the uncertainty on their parameters is substantial. We use:

- **Primary mass**: a fixed value of $20\,\mathrm{M}_{\odot}$.
- **Mass ratio**: a fixed value of 0.9.
- **Spin magnitude**: same as the local BBH population.
- **Redshift**: the merger rate follows the distribution introduced in [34] (equation (C15)) with $a_{III}=0.66$, $b_{III}=0.3$ and $z_{III}=11.6$.

3.1.3. Primordial black holes. In addition, we consider a population of even higher redshift sources that could be representative of primordial black holes. For these too, our knowledge of the masses and spins of the companion black holes is very limited. Nonetheless, we use:

- **Primary and secondary mass**: the lognormal distribution of [35] (equation (1)) centered at $M_c=30\,\mathrm{M}_{\odot}$ and with $\sigma=0.3\,\mathrm{M}_{\odot}$.
- **Spin magnitude**: zero spins.
- **Redshift**: merger rate distribution that increases as the age of the Universe decreases ([35], equation (5)).

While the prescriptions above fix the characteristics for each formation channel, for Pop III and primordial black holes we need two more parameters to fix the relative importance of these channels. We follow [34, 35] and work with $N_{\mathrm{III}}=2400$ and $N_{\mathrm{pbh}}=600$ mergers per year in the two channels.

3.1.4. Intermediate mass BBHs. We would also like to know how well the next generation of GW observatories can characterize a population of intermediate-mass BBH (IMBBHs) binaries, especially with the improved sensitivity at low frequencies. We use:

- **Masses**: a power-law distribution for the two masses with $\alpha=-2.5$. Further, we choose the smallest and largest masses in the distribution to be $m_{\mathrm{min}}=100\,\mathrm{M}_{\odot}$ and $m_{\mathrm{max}}=1000\,\mathrm{M}_{\odot}$, respectively. Masses larger than about $10^3\,\mathrm{M}_{\odot}$ are not likely to be observed by next-generation observatories as they could merge well before reaching the sensitivity of CE or ET.
- **Spins**: the spins for both the BHs are chosen to follow a uniform distribution between $[-0.9, 0.9]$.
- **Redshift**: same as the local BBH population, but with a local merger rate density of $1\,\mathrm{Gpc}^{-3}\,\mathrm{yr}^{-1}$.

3.2. BNSs

We simulate a single population of BNSs, whose merger rate peaks at cosmic noon, and is consistent with the local merger rate as measured by the LIGO-Virgo-KAGRA (LVK) Collaboration. We choose the following parameters:

- **Primary and secondary mass**: a double Gaussian distribution, $p(m) = w\mathcal{N}(\mu_L, \sigma_L) + (1 - w)\mathcal{N}(\mu_R, \sigma_R)$. We use parameters equal to the median values of [36]: $\mu_L = 1.35\,\mathrm{M}_\odot$, $\sigma_L = 0.08\,\mathrm{M}_\odot$, $\mu_R = 1.8\,\mathrm{M}_\odot$, $\sigma_R = 0.3\,\mathrm{M}_\odot$, and $w = 0.64$. Each normal distribution is independently truncated and normalized in the range $[1, 2.2]$ $\mathrm{M}_\odot$. The neutron stars chosen from one Gaussian distribution are allowed to pair with neutron stars from the same Gaussian distribution.
- **Spin magnitude**: uniform in the range $[0, 0.1]$.
- **Redshift**: same as local BBHs, but with a local merger rate density of 320 Gpc^{-3} yr^{-1} [33].
- **EoS**: we use `APR4` [37] as the EoS of the neutron star. Note that the maximum mass of the NS listed above corresponds to the maximum mass allowed by the `APR4`.

While there is some evidence that the population probed by LVK via GWs differs from the galactic neutron-star population from which this bimodal mass distribution is derived, simulating a structured mass distribution allows us to verify if and how precisely XG observatories can characterize the population (see table 1).

3.3. NSBH mergers

Due to low number of detections, the properties of NSBH mergers are not well known. Because of this uncertainty, we will adopt a semi-agnostic approach to define the population for NSBH mergers. The specifications are as follows:

- **Black hole mass**: the `POWER LAW + PEAK` distribution, same as the primary mass of the local BBH population.
- **Neutron star mass**: uniform between [1,2.2] $\mathrm{M}_\odot$.
- **Spins**: for the BH, the spin is assumed to be aligned with the orbital angular momentum and follows a Gaussian distribution with $\mu = 0$ and $\sigma = 0.2$. The NS is assumed to be slowly spinning, following a uniform distribution between $[-0.1, 0.1]$.
- **Redshift**: same as the local BBH population, but with a local merger rate density of 45 Gpc^{-3} yr^{-1} [28, 38].

For all other GW parameters for all the cases (i.e. sky location, orbital orientation, polarization angle, coalescence time and phase) we use uninformative distributions. We assume all sources are quasi-circular, i.e. we ignore orbital eccentricity.

4. Detection and parameter estimation

Having introduced different network configurations and population models, we next wish to address the detectability of these source classes and how precisely the parameters of these sources can be extracted with different detector configurations. Detectability is quantified in terms of the SNR ρ defined as

$$\rho^2 = 4 \int_{f_{\mathrm{low}}}^{f_{\mathrm{upper}}} \frac{|\tilde{h}_A|^2}{S_n^{\mathrm{A}}} \mathrm{d}f, \tag{2}$$

where $\tilde{h}_A$ is the waveform of the signal at detector A, $S_n^{\rm A}$ is the one-sided noise power spectral density (PSD) of detector A and $f_{\rm low}$ and $f_{\rm upper}$ denote the lower and upper cut of frequencies of the integration.

Similarly, we use the Fisher information matrix to compute the statistical uncertainties associated with measuring binary parameters. The Fisher matrix Γ_{ab} is related to the derivatives of the waveform with respect to the set of source parameters $\boldsymbol{\lambda}$ as

$$\Gamma_{ab} = 2\int_{f_{\rm low}}^{f_{\rm upper}} \frac{\tilde{h}_{{\rm A},a}\tilde{h}^{\star}_{{\rm A},b} + \tilde{h}^{\star}_{{\rm A},a}\tilde{h}_{{\rm A},b}}{S_n^{\rm A}}\,{\rm d}f, \tag{3}$$

where $\star$ denotes the operation of complex conjugation and the comma denotes differentiation with respect to various elements of the parameter space $\boldsymbol{\lambda}$. The inverse of the Fisher matrix is called covariance matrix Σ_{ab} and the square root of the diagonal elements provides the 1σ (68% CL) uncertainty range for the measurement of different parameters for a given detector A

$$\sigma_a = \sqrt{\Sigma_{aa}}. \tag{4}$$

All measurement uncertainties mentioned here are at 68% credibility except the angular resolution $\Delta\Omega$, which is reported at 90% credibility.

The Fisher matrix estimates are applicable primarily in the high-SNR or linear signal approximation limit [39]. Generally, measurement errors estimated using this method are expected to be underestimations compared to those obtained through Bayesian analysis, even for systems detected with SNRs around 20 [40]. The 90%-credible sky-area is underestimated by the Fisher approach for a threshold SNR of 12, although there is a broad agreement between the Fisher and Bayesian estimates for a threshold SNR of 25 [41]. However, studies have shown discrepancies in this trend, finding that the Fisher matrix method can overestimate errors for intrinsic parameters [42] (also see [43] which attributes some of these discrepancies to truncation effects). Dupletsa *et al* [44] compared Fisher and Bayesian estimates for GWTC-3 events and found the Fisher errors to be larger than the Bayesian ones for intrinsic parameters, and that including priors on these parameters when calculating the Fisher errors reduces the difference. As we do not include priors when performing the Fisher analysis, the error estimates on intrinsic parameters presented in this work may be conservative.

For the computation of errors, we use `GWBENCH` [45], a publicly available Python-based software that computes the Fisher matrix for various waveform families available in the LIGO algorithms library (LAL) [46]. Fisher matrix is then numerically inverted to deduce the statistical errors associated with the measurement of various parameters in the waveform. `GWBENCH` can perform parameter estimation for different combinations of detector networks, thereby facilitating a detailed assessment of their performance.

Here, we use the IMRPhenomXHM [47] waveform to deduce errors in the case of BBHs and NSBHs whereas we use IMRPhenomPV2_NRtidalv2 [48] for BNSs. The former is a non-processing waveform that covers the inspiral-merger-ringdown phases of a compact binary merger and has higher-order spherical harmonic modes. On the other hand, IMRPhenmPV2_NRtidalv2 has only the leading $\ell = 2, m = 2$ mode of the gravitational waveform but accounts for tidal effects up to 6PN order.

The parameter space spanned by BBH and NSBH signals is given by

$$\boldsymbol{\lambda} = \{\mathcal{M}, \eta, \chi_{1z}, \chi_{2z} D_L, \iota, \alpha, \delta, \psi, t_c, \phi_c\}, \tag{5}$$

which denote chirp mass ($\mathcal{M} = (m_1 m_2)^{0.6}/(m_1 + m_2)^{0.2}$), symmetric mass ratio ($\eta = m_1 m_2/(m_1 + m_2)^2$), projections of the spins of the primary and secondary along the orbital angular momentum axis, luminosity distance to the source, inclination angle, right ascension and declination, polarization angle, time and phase at coalescence, respectively (see section IIB of [49] for details). For BNS systems, in addition to these parameters, effective tidal deformability $\lambda_{\rm eff}$ is added as an additional parameter to be estimated. The lower cut-off frequency is taken to be 5 Hz for all the network configurations. The upper cut-off frequency for all cases is the frequency above which the signal has no power.

Using `GWBENCH` we next study the detection efficiency and detection rates of various classes of sources introduced earlier for the different detector configurations. We then discuss the parameter uncertainties and their implications for astrophysics and fundamental physics.

4.1. Detection efficiency and detection rate

The detection efficiency $\epsilon(z)$ of an observatory is a function of the luminosity distance or, equivalently, redshift. It is the fraction of all events at a redshift z that are observed with an expected SNR greater than a preset threshold SNR. Instead of an SNR threshold, one could define the efficiency at a fixed false alarm rate but in the Fisher matrix approach the two are equivalent. We quote the efficiency at two different SNR thresholds: a network SNR $\rho_* = 10$ and $\rho_* = 100$, where the SNR of a network is root-mean-square SNR obtained for all the detectors in the network. In addition, we also require each detector in the network to record a minimum SNR of 5 to say that it is detected. An SNR of $\rho = 10$ serves as the smallest SNR at which a confident detection can be made while an SNR of $\rho = 100$ is an SNR at which exquisite measurement can be made.

The detection efficiency of different detector networks is reported in figure 2 and in table 4. The left panels of figure 2 show the detection efficiency as a function of redshift while the right panels show the detection rate per year for BNS, NSBH and BBH populations, respectively. The grey region shows the error bars due to the uncertainties in their current merger rates. Table 4 quantifies the capabilities even better in terms of redshift reach as well as the number of detections that these configurations can make based on our current understanding of their rates.

With an SNR of 10, 50% of the BNS merger may be detected at a redshift of 1.7 with the 4020ET 3 XG network, whereas an HLA network can observe these sources only up to a redshift of 0.18, almost a factor of 10 smaller. There is unlikely to be any BNS detection with an SNR above 100 with HLA whereas it is seen that $\mathcal{O}(100)$ such detections could be made with the 4020ET network per year.

Similarly, for NSBH mergers, compared to a redshift reach of 0.18(0.04) at an SNR of 10(100) with HLA, the 4020ET network can see up to a redshift of 4.5(0.3), which highlights the benefits XG detectors bring in. Also, given our current rates, it is unlikely that an HLA network would detect any NSBH merger with an SNR above 100 whereas a 4020ET network is likely to detect $\mathcal{O}(100)$ of these. Performance of 1 XG and 2 XG detectors lie in between these two extremes which may see $\mathcal{O}(1)$ and $\mathcal{O}(10)$ such sources per year, respectively.

It is impressive to note that the 4020ET network, which has a redshift reach of 27 with an SNR threshold of 10, would detect almost all BBHs within the horizon of $z = 5$. On the other hand, the detectability of BBHs is complete only up to a redshift of 0.01 for the HLA network. The 4020ET network would see around 6000 BBHs per year which has an SNR of 100 or above. This will provide us with an unprecedented opportunity to probe the diverse classes of BBHs and infer their astrophysical properties and formation mechanism, among other things.

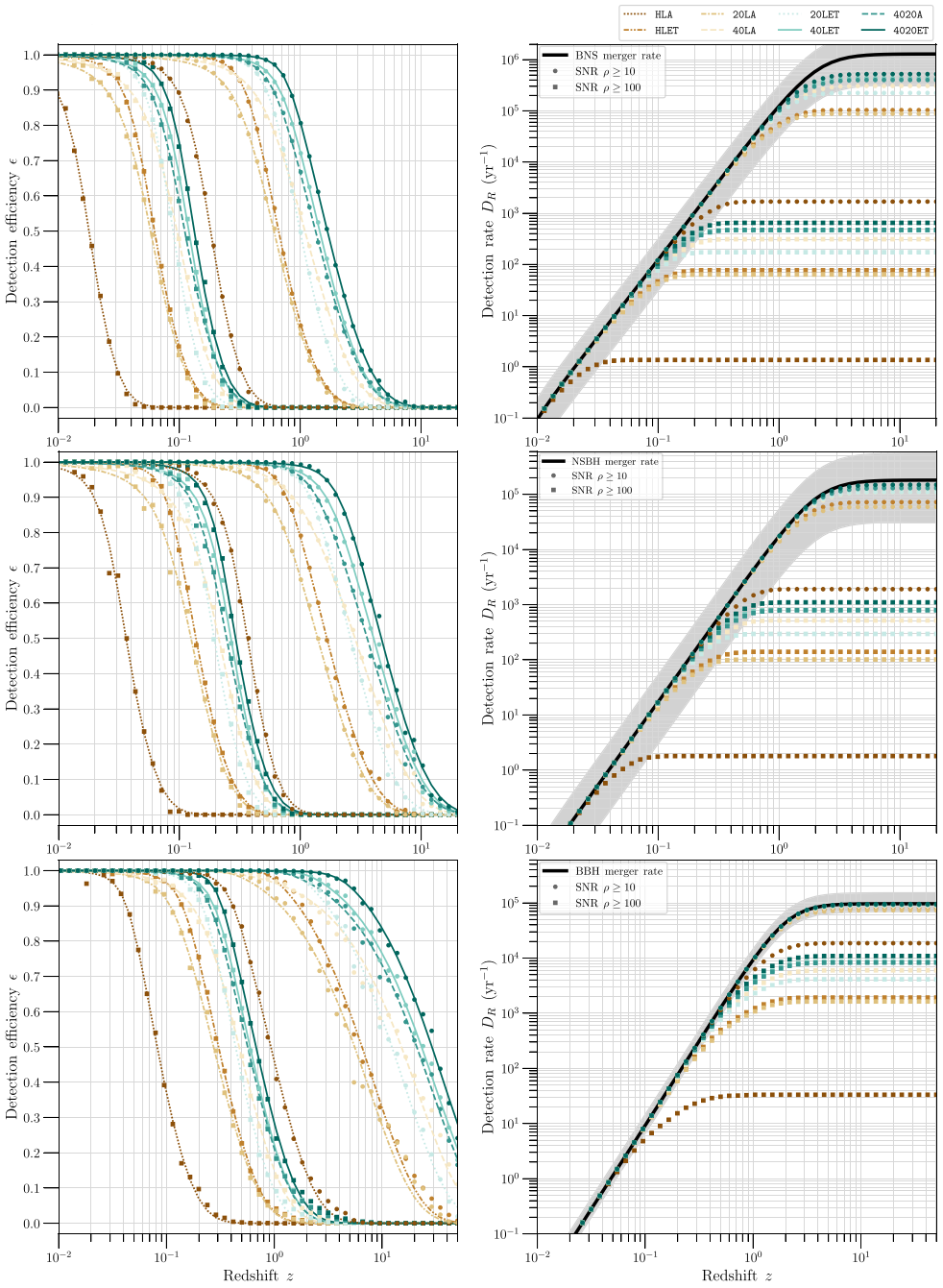

Figure 2. The network efficiency (left panels) and detection rate (right panels) for the eight GW detector networks. For each network, we plot the efficiency and rate at two threshold SNRs, one at 10 (circles) and the other at 100 (squares). Solid lines in the left panels are the *best-fit* sigmoid functions of the efficiency. Black solid lines on the right are the total merger rate and the gray shaded area is the variation in the rate due to the uncertainty in the local merger rate density determined from current observations [28, 33]. From top to bottom, the panels correspond to BNS, NSBH and BBH systems.

Table 4. The redshift reach z at which the detection efficiency of a network is 50% corresponding to binary merger events for the eight detector networks (column 1) for threshold SNRs of $\rho_* = 10$ and $\rho_* = 100$ (columns 2 and 3) are listed together with the number events every year with SNRs greater than 10 (column 4), 30 (column 5), and 100 (column 6). The lower and upper bounds in these columns are calculated using the uncertainty in the local merger rate density as determined by current observations.

Network	$z(\rho_* = 10)$	$z(\rho_* = 100)$	$N(\rho > 10)$	$N(\rho > 30)$	$N(\rho > 100)$
BNS: cosmic merger rate is $1.2^{+2.0}_{-0.9} \times 10^6$ yr^{-1}					
HLA	0.18	0.018	$1.3^{+1.9}_{-1.0} \times 10^3$	$2.7^{+6.6}_{-2.3} \times 10^1$	0
HLET	0.66	0.062	$8.5^{+13.0}_{-6.4} \times 10^4$	$2.5^{+3.9}_{-1.9} \times 10^3$	$4.8^{+7.4}_{-3.7} \times 10^1$
20LA	0.61	0.058	$7.1^{+11.0}_{-5.4} \times 10^4$	$2.1^{+3.1}_{-1.6} \times 10^3$	$3.9^{+6.7}_{-3.3} \times 10^1$
40LA	1.1	0.096	$2.7^{+4.1}_{-2.0} \times 10^5$	$1.1^{+1.7}_{-0.8} \times 10^4$	$2.2^{+3.3}_{-1.8} \times 10^2$
20LET	1	0.089	$1.9^{+2.9}_{-1.4} \times 10^5$	$5.9^{+9.0}_{-4.4} \times 10^3$	$1.2^{+1.9}_{-1.0} \times 10^2$
40LET	1.4	0.12	$3.9^{+5.9}_{-2.9} \times 10^5$	$1.7^{+2.6}_{-1.2} \times 10^4$	$3.5^{+5.5}_{-2.9} \times 10^2$
4020A	1.3	0.11	$3.6^{+5.5}_{-2.7} \times 10^5$	$1.7^{+2.6}_{-1.3} \times 10^4$	$3.5^{+5.6}_{-2.9} \times 10^2$
4020ET	1.7	0.13	$4.7^{+7.2}_{-3.5} \times 10^5$	$2.3^{+3.6}_{-1.8} \times 10^4$	$4.8^{+7.7}_{-3.9} \times 10^2$
NSBH: cosmic merger rate is $1.8^{+3.8}_{-1.5} \times 10^5$ yr^{-1}					
HLA	0.36	0.036	$1.5^{+3.1}_{-1.2} \times 10^3$	$3.6^{+9.2}_{-3.3} \times 10^1$	$0.0^{+1.0}_{-0.0} \times 10^0$
HLET	1.5	0.13	$5.9^{+12.4}_{-4.8} \times 10^4$	$3.7^{+8.2}_{-3.1} \times 10^3$	$8.4^{+17.2}_{-7.2} \times 10^1$
20LA	1.4	0.12	$5.3^{+11.3}_{-4.4} \times 10^4$	$3.2^{+7.1}_{-2.7} \times 10^3$	$7.4^{+14.6}_{-6.7} \times 10^1$
40LA	2.8	0.21	$1.0^{+2.2}_{-0.9} \times 10^5$	$1.5^{+3.3}_{-1.3} \times 10^4$	$3.9^{+8.0}_{-3.2} \times 10^2$
20LET	2.5	0.19	$9.8^{+20.7}_{-8.1} \times 10^4$	$8.8^{+19.1}_{-7.3} \times 10^3$	$2.2^{+4.3}_{-1.8} \times 10^2$
40LET	3.8	0.26	$1.3^{+2.7}_{-1.1} \times 10^5$	$2.2^{+4.7}_{-1.8} \times 10^4$	$6.1^{+12.0}_{-5.1} \times 10^2$
4020A	3.5	0.24	$1.2^{+2.6}_{-1.0} \times 10^5$	$2.2^{+4.6}_{-1.8} \times 10^4$	$6.1^{+12.3}_{-5.1} \times 10^2$
4020ET	4.5	0.28	$1.4^{+3.0}_{-1.2} \times 10^5$	$2.9^{+6.2}_{-2.4} \times 10^4$	$8.4^{+17.1}_{-7.1} \times 10^2$
BBH: cosmic merger rate is $9.6^{+5.7}_{-2.8} \times 10^4$ yr^{-1}					
HLA	0.92	0.083	$1.6^{+9.3}_{-0.5} \times 10^4$	$1.1^{+6.3}_{-0.3} \times 10^3$	$1.7^{+1.2}_{-0.5} \times 10^1$
HLET	6.3	0.3	$7.7^{+4.5}_{-2.2} \times 10^4$	$2.3^{+1.3}_{-0.7} \times 10^4$	$1.6^{+9.0}_{-0.5} \times 10^3$
20LA	5.6	0.28	$7.1^{+4.1}_{-2.1} \times 10^4$	$2.1^{+1.2}_{-0.6} \times 10^4$	$1.3^{+7.3}_{-0.4} \times 10^3$
40LA	15	0.47	$8.5^{+4.9}_{-2.5} \times 10^4$	$4.3^{+2.5}_{-1.2} \times 10^4$	$5.0^{+3.0}_{-1.5} \times 10^3$
20LET	12	0.43	$8.9^{+5.2}_{-2.6} \times 10^4$	$3.8^{+2.3}_{-1.1} \times 10^4$	$3.3^{+2.0}_{-1.0} \times 10^3$
40LET	22	0.60	$9.2^{+5.4}_{-2.7} \times 10^4$	$5.5^{+3.2}_{-1.6} \times 10^4$	$7.3^{+4.3}_{-2.2} \times 10^3$
4020A	20	0.56	$9.1^{+5.3}_{-2.7} \times 10^4$	$5.1^{+3.0}_{-1.5} \times 10^4$	$6.9^{+4.0}_{-2.0} \times 10^3$
4020ET	27	0.67	$9.5^{+5.5}_{-2.8} \times 10^4$	$6.1^{+3.6}_{-1.8} \times 10^4$	$9.2^{+5.4}_{-2.7} \times 10^3$

Networks with 1 XG and 2 XG networks can also detect hundreds to a couple of thousands of these golden BBHs.

4.2. Measurement uncertainty of source parameters

We are now in a position to study the statistical uncertainties with which different compact binary parameters will be estimated by various detector networks. Figures 3–5 summarize our results for BBH, BNS and NSBH populations, respectively.

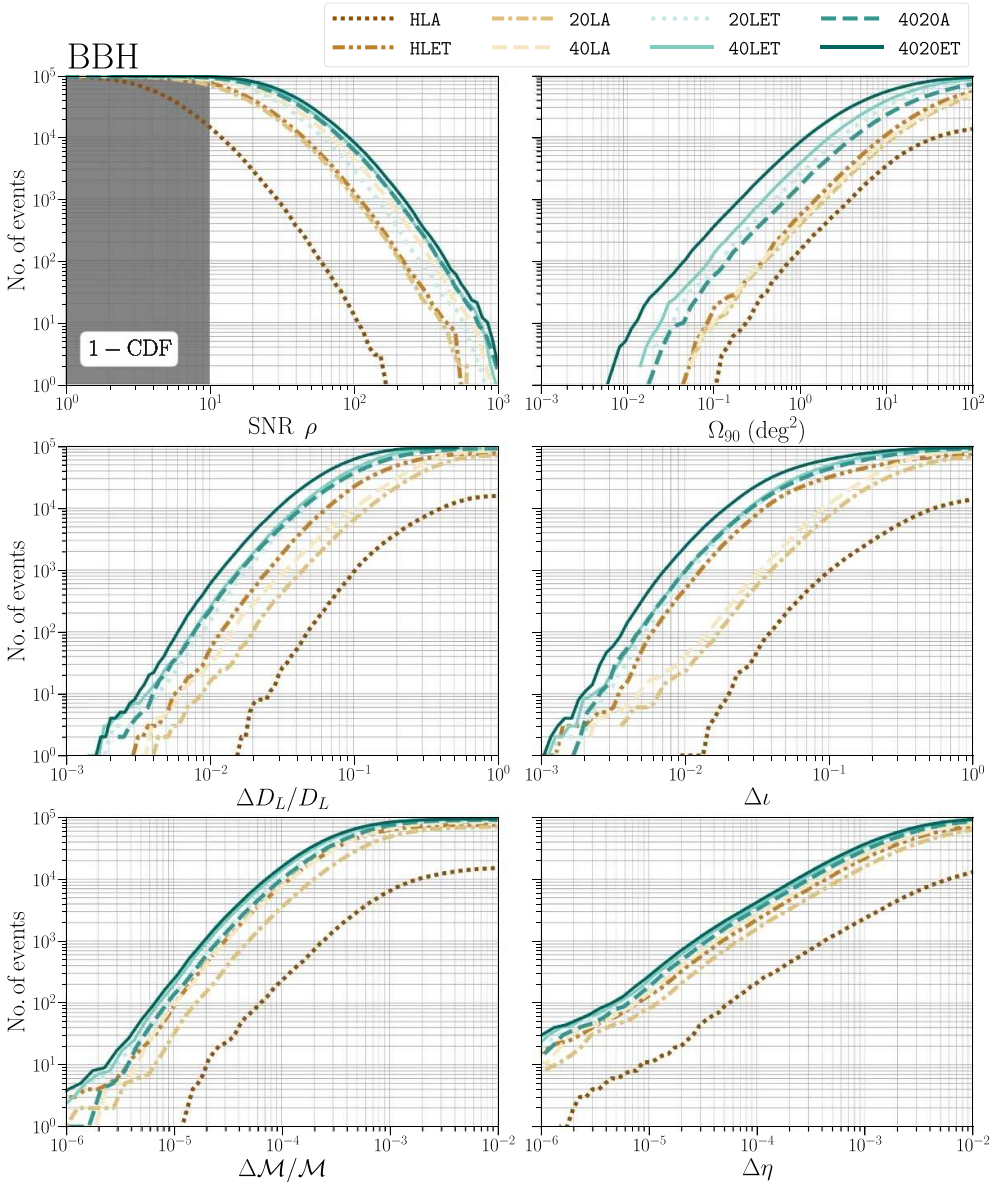

Figure 3. The scaled cumulative density function plots showing the trends in SNR ρ and sky-localization $\Delta\Omega$ of the detected BBH events. It also shows the plots for fractional errors in chirp mass and luminosity distance, i.e. $\Delta\mathcal{M}/\mathcal{M}$ and $\Delta D_L/D_L$, and absolute errors in inclination angle, and symmetric mass ratio, i.e. $\Delta\iota$ and $\Delta\eta$, respectively.

4.2.1. BBHs. Figure 3 shows the number of detections as a function of SNR, errors in source localization, luminosity distance, inclination angle, chirp mass and symmetric mass ratio for the population we synthesized and analyzed for different network configurations. Overall, as expected, the performance of the 3 XG network is the best followed by 2 XG, 1 XG and 0

XG clearly suggesting the crucial role 3G detectors will play in the precision measurement of source parameters.

It is seen that a 4020ET network would detect $\mathcal{O}(10)$ events with an SNR of 1000. These high-fidelity sources are going to play an extremely crucial role in astrophysics, cosmology and fundamental physics as they facilitate very precise inference of source parameters. The number of high-fidelity sources in a 1 XG or 0 XG network is considerably less whereas 2 XG numbers would fare comparably with 3 XG, though the numbers are slightly less. In parameter inference, the 3 XG network performs significantly better for the angular resolution and moderately better for luminosity distance and inclination angle measurements compared to the second-best configuration 40LET thereby underscoring the importance of a 3 XG network.

Regarding individual measurements, it is interesting to note that a golden subpopulation of $\mathcal{O}(100)$ BBHs would allow the measurement of chirp mass and symmetric mass ratio of $\mathcal{O}(10^{-5})$ by a 3 XG network. Similarly, the 4020ET network would allow localization of a subpopulation of BBHs to $\leqslant 0.01\,\mathrm{deg}^2$ and luminosity distance error $\leqslant 1\%$. These sources could allow precise measurement of Hubble constant [50]. Likewise, the precisely localized subpopulation would also be useful in searching for a potential EM counterpart [51].

4.2.2. BNSs. Figure 4 displays the parameter inference in the context of BNS mergers using various network configurations. The trends in terms of various detector networks remain as in the case of BBHs where 3 XG network performs the best followed by 2 XG, 1 XG and 0 XG networks. In terms of sources with SNR higher than 100, 3 XG and 2 XG configurations fare comparably as they detect a few hundred sources. A 3 XG network may be able to localize around 100 BNS mergers to about $0.2\,\mathrm{deg}^2$ whereas the best-localized 100 sources by a 2 XG network may have an angular resolution which is a factor of 3 worse at $0.6\,\mathrm{deg}^2$. Likewise, 3 XG detectors will measure luminosity distance of about 100 sources to less than 2% and the performance of a 2 XG network is comparable though slightly worse, as expected.

The inference of inclination angle is very important in this case as it may help in better understanding the structure of the relativistic jets potentially associated with these mergers and may be of immense help in the multimessenger modeling of BNS mergers. It is impressive to note that both 3 XG and 2 XG detectors will be able to measure $\Delta\iota \leqslant 0.01\,\mathrm{deg}$ for about 100 sources. The mass measurement uncertainties are even more exquisite as a few tens of sources with 3 XG detectors will permit measurement of chirp mass to $10^{-4}\%$ and close to 100 sources will be able to measure $\Delta\eta \leqslant 10^{-5}$. These mass measurements would potentially be the most precise measurements of NS masses. These measurements also carry a lot of importance for understanding the equation of the state of the neutron stars as well as in the measurement of their radii.

4.2.3. Neutron star–black holes. NSBH mergers, like BNS mergers, are of importance because a subset of them would be multimessenger sources. In terms of performance hierarchy, the trends seen in figure 5 for NSBHs are similar to that of BBH and BNSs. The number of events with an SNR of 100 or above is close to 1000 with 3 XG and 2 XG networks while it is around 100 with 1 XG networks. High-fidelity NSBHs with SNR above 400, which will be important for cosmology, multimessenger follow-up and distinguishing astrophysical formation channels [52], are of the order of 10 even with 3 XG and 2 XG networks.

The number of sources that are localized to better than $0.02\,\mathrm{deg}^2$ is close to 100 for 3 XG while it is of the order of a few tens for 2 XG and even lesser for 1 XG. Similar trends are seen for luminosity distance, where $\mathcal{O}(100)$ sources would allow better than 1% measurement of luminosity distance with 3 XG and comparable, but slightly less, number of sources with 2

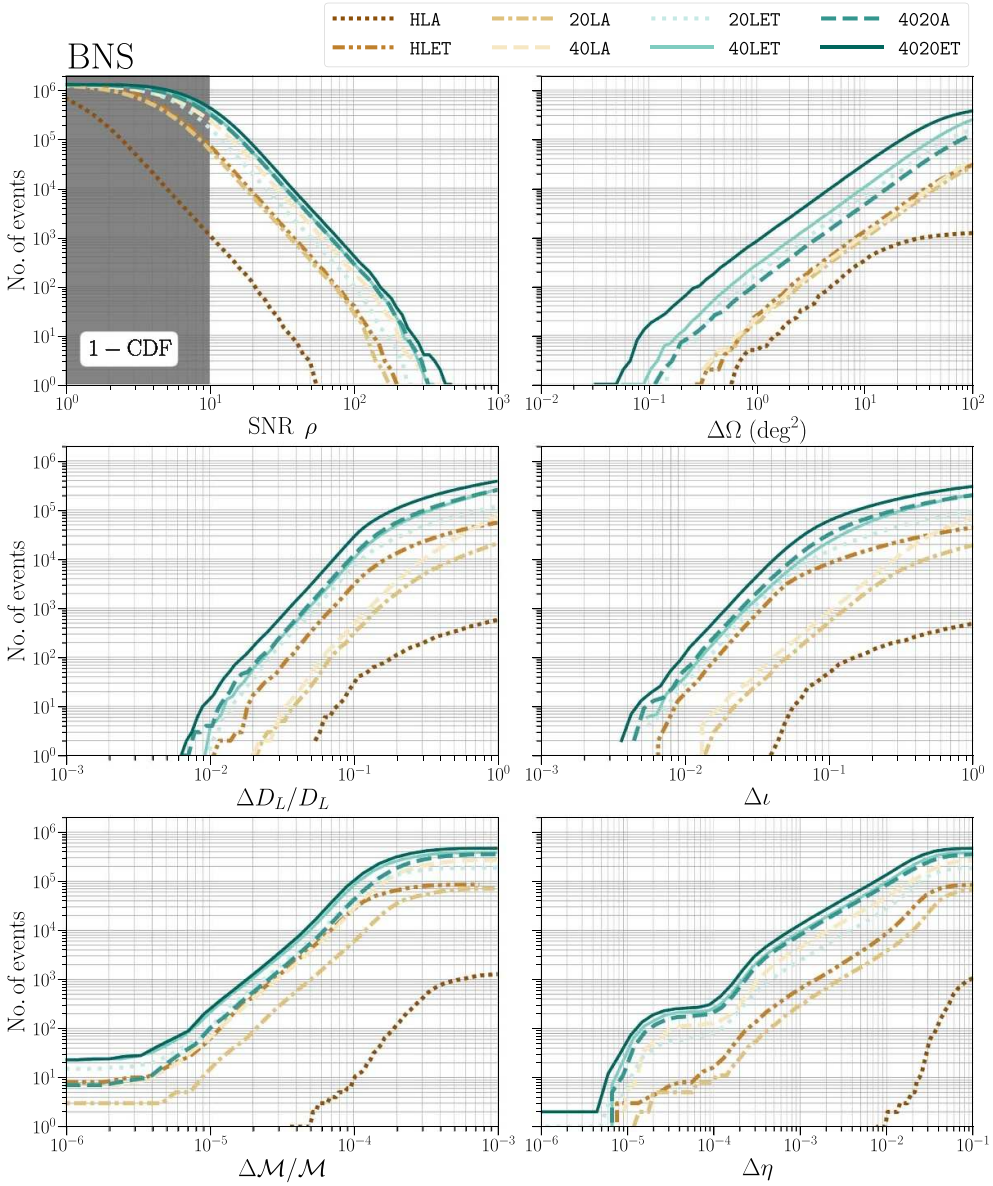

Figure 4. The scaled cumulative density function plots showing the trends in SNR ρ and sky-localization $\Delta\Omega$ of the detected BNS events. It also shows the plots for fractional errors in chirp mass and luminosity distance, i.e. $\Delta\mathcal{M}/\mathcal{M}$ and $\Delta D_L/D_L$, and absolute errors in inclination angle, and symmetric mass ratio, i.e. $\Delta\iota$ and $\Delta\eta$, respectively.

XG. The inclination angle may be estimated to be better than 0.01 deg for 100 sources with 3 XG and 2 XG networks. Regarding mass measurements, again, around 100 sources will permit measurement of chirp mass and symmetric mass ratio to better than 10^{-5}. These measurements will be crucial for inferring the NS EoS as well as understanding the 'low mass gap' black holes with masses less than $5M_\odot$ which are not observed in galactic x-ray binaries.

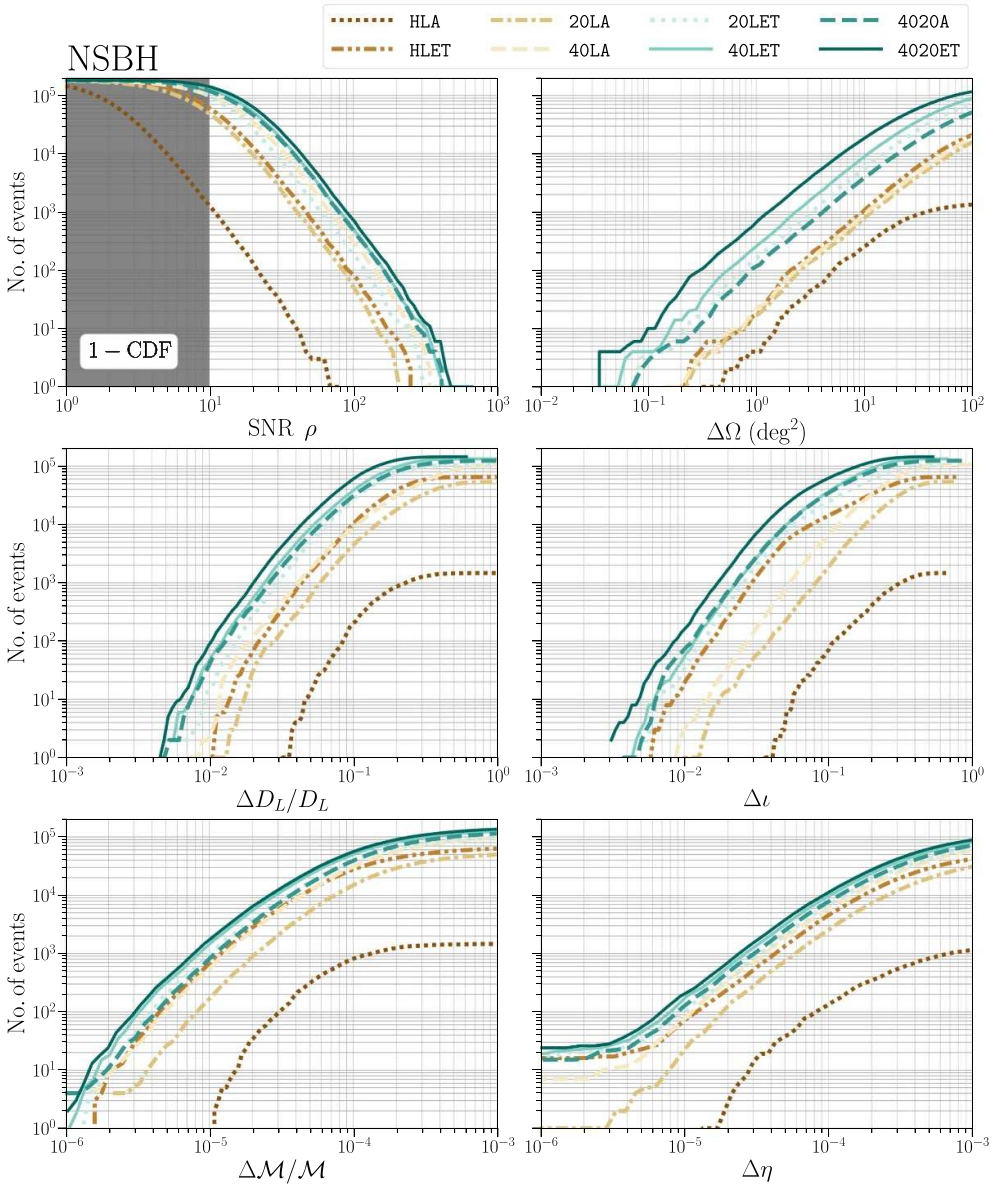

Figure 5. The scaled cumulative density function plots showing the trends in SNR ρ and sky-localization $\Delta\Omega$ of the detected NSBH events. It also shows the plots for fractional errors in chirp mass and luminosity distance, i.e. $\Delta\mathcal{M}/\mathcal{M}$ and $\Delta D_L/D_L$, and absolute errors in inclination angle, symmetric mass ratio, and spins of the BH and the NS i.e. $\Delta\iota$, and $\Delta\eta$, respectively.

To summarize, for all the three classes of populations any combination of networks with at least one 3G detector performs significantly better than three detectors at $A^\sharp$ sensitivity with 4020ET, a network with two CE and one ET, being the winner in all the metrics considered.

Table 5. The field of view (FOV) of some of the existing and planned (in italics) electromagnetic (EM) telescopes. The space telescopes are in bold and will operate for a limited lifetime of the Cosmic Explorer facility.

Telescope	FOV (deg^2)
Rubin [53, 54]	9.6
EUCLID [55]	0.54
Athena [56]	0.35
Roman [57, 58]	0.28
ngVLA [59] (2.4 GHz; FWHM)	0.17
Chandra x-ray [60]	0.15
Lynx [61]	0.13
Swift-XRT [62]	0.12
Keck [63]	0.11
GMT [64]	0.11
ELT[a]	0.03
Jansky VLA [65] (3 GHz; FWHM)	0.0625

[a] For a brief description of the extremely large telescope see www.eso.org/sci/publications/messenger/archive/no.127-mar07/messenger-no127-11-19.pdf

4.3. 3D localization of sources and early-warning

In addition to the source parameters, one can also infer the sky location and the luminosity distance associated with the source from the GW data. Precise localization of the source is critical for multiple science objectives. Assuming that the cosmology is known, accurate distance estimation enables the calculation of source-frame masses of the binary objects, which are important for unraveling the mass spectrum and distinguishing between formation channels (see section 5.1). Localization of the source plays a crucial role in enabling MMA (see section 5.2) and inference of cosmological parameters (see section 5.4). The localization of the source from GW observations is communicated to EM telescopes, which allows them to capture EM transients that may follow the binary merger. While the field of view (FOV) of EM telescopes is, in general, smaller than 10 deg^2 (see table 5), they can cover multiple patches in the sky to observe large sky areas. Thus, precise localization and timely communication are necessary to facilitate MMA.

Table 6 shows the number of BBH detections every year for varying precision of sky-localization and luminosity distance measurement. Without any XG detectors, a network with three A$^\sharp$ detectors is only able to localize $\sim 1\%$ of all BBH mergers to a smaller area than 100 deg^2 in the sky. Having just one XG detector enhances this fraction to $\sim 50\%$, whereas a network with three XG detectors is able to localize $\sim 95\%$ of all BBH mergers to $\Delta\Omega \leqslant 100\,\mathrm{deg}^2$. Further, networks with at least two XG detectors localize $\mathcal{O}(1000)$ BBH events every year to better than $1\,\mathrm{deg}^2$, which is an order of magnitude more events compared to a network containing only one XG detector. In addition, figure 6 also shows that only networks with three XG detectors are able to localize events to $\Delta\Omega \leqslant 0.1\,\mathrm{deg}^2$. This metric is of particular relevance to host-galaxy identification, as the number of galaxies lying within an observation volume scales linearly with sky area.

The luminosity distance measurement is also aided by the improved sensitivity of the XG detectors. For a network with three A$^\sharp$ detectors, we can expect about 100 BBH mergers every year for which the error in luminosity distance is within 10%. However, luminosity distance cannot be measured to 1% precision for any of the events. For networks with two or more XG detectors, not only will they detect thousands of BBH mergers every year for which $\Delta D_L/D_L \leqslant$

Table 6. The number of BBH detections per year for the eight detector networks with 90%-credible sky area less than 10, 1, 0.1 and 0.01 deg^2 and fractional error in luminosity distance less than 0.1 and 0.01.

Metric	$\Delta\Omega(\mathrm{deg})^2$					$\Delta D_L/D_L$	
Quality	$\leqslant 100$	$\leqslant 10$	$\leqslant 1$	$\leqslant 0.1$	$\leqslant 0.01$	$\leqslant 0.1$	$\leqslant 0.01$
HLA	$1.3^{+7.8}_{-0.4}\times 10^4$	$3.1^{+2.0}_{-0.9}\times 10^3$	$1.3^{+7.2}_{-0.4}\times 10^2$	$1.0^{+4.0}_{-0.0}\times 10^0$	0	$8.4^{+4.5}_{-2.4}\times 10^2$	0
HLET	$5.2^{+3.0}_{-1.5}\times 10^4$	$9.9^{+5.8}_{-2.9}\times 10^3$	$4.8^{+2.7}_{-1.4}\times 10^2$	$1.4^{+1.2}_{-0.8}\times 10^1$	0	$2.1^{+1.2}_{-0.6}\times 10^4$	$4.2^{+2.2}_{-1.4}\times 10^1$
20LA	$4.4^{+2.5}_{-1.3}\times 10^4$	$7.3^{+4.3}_{-2.1}\times 10^3$	$3.4^{+2.0}_{-1.0}\times 10^2$	$8.0^{+5.0}_{-6.0}\times 10^0$	0	$5.9^{+3.3}_{-1.7}\times 10^3$	$1.3^{+5.0}_{-0.5}\times 10^1$
40LA	$4.8^{+2.8}_{-1.4}\times 10^4$	$8.1^{+4.8}_{-2.4}\times 10^3$	$3.8^{+2.3}_{-1.1}\times 10^2$	$9.0^{+6.0}_{-7.0}\times 10^0$	0	$9.0^{+5.2}_{-2.6}\times 10^3$	$2.8^{+1.2}_{-0.7}\times 10^1$
20LET	$8.1^{+4.7}_{-2.3}\times 10^4$	$2.9^{+1.7}_{-0.8}\times 10^4$	$2.3^{+1.4}_{-0.7}\times 10^3$	$6.6^{+4.3}_{-2.3}\times 10^1$	0	$3.6^{+2.1}_{-1.1}\times 10^4$	$1.2^{+7.0}_{-0.4}\times 10^2$
40LET	$8.5^{+5.0}_{-2.5}\times 10^4$	$3.7^{+2.1}_{-1.1}\times 10^4$	$3.4^{+2.1}_{-1.0}\times 10^3$	$1.1^{+6.8}_{-0.4}\times 10^2$	$0.0^{+1.0}_{-0.0}\times 10^0$	$4.1^{+2.4}_{-1.2}\times 10^4$	$2.1^{+1.2}_{-0.7}\times 10^2$
4020A	$7.0^{+4.1}_{-2.0}\times 10^4$	$2.1^{+1.2}_{-0.6}\times 10^4$	$1.4^{+8.9}_{-0.4}\times 10^3$	$5.2^{+3.3}_{-2.2}\times 10^1$	0	$3.4^{+2.0}_{-1.0}\times 10^4$	$1.9^{+1.2}_{-0.5}\times 10^2$
4020ET	$9.1^{+5.3}_{-2.7}\times 10^4$	$5.2^{+3.0}_{-1.5}\times 10^4$	$7.6^{+4.5}_{-2.2}\times 10^3$	$3.1^{+1.8}_{-0.9}\times 10^2$	$5.0^{+5.0}_{-3.0}\times 10^0$	$5.9^{+3.4}_{-1.7}\times 10^4$	$5.1^{+2.8}_{-1.5}\times 10^2$

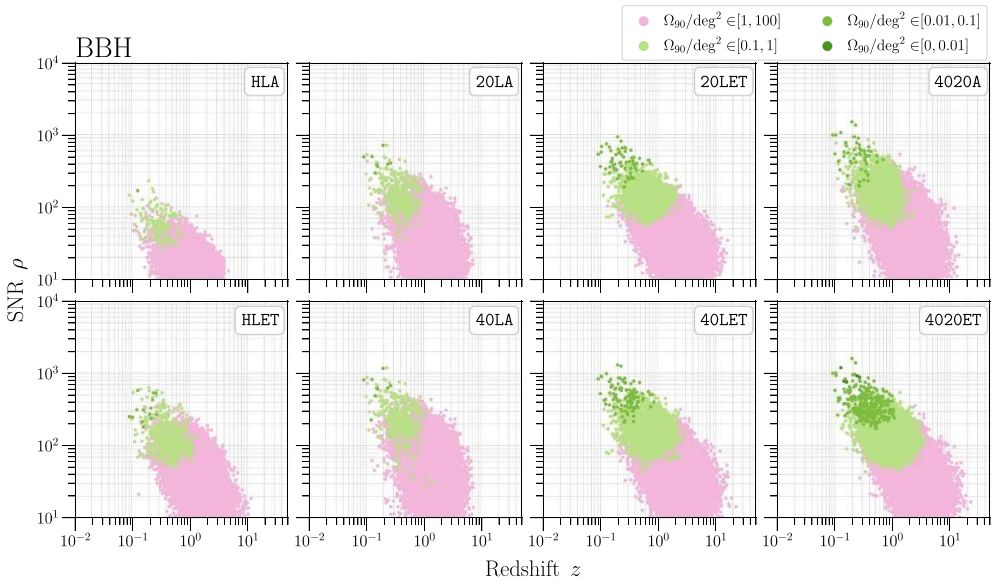

Figure 6. Plot showing the relationship between SNR ρ, sky localization $\Delta\Omega$ and the redshift z for events belonging to the Pop-1 population, corresponding to the eight GW detector networks. Each marker is an event detected by the corresponding detector network in an observation time of 1 year. The color of the marker conveys how well that event can be localized in the sky using GW observation.

0.1, but they will also detect tens of events for which luminosity distance is measured to sub-percent precision.

For compact binary mergers involving one or more NS, localization is important to facilitate EM follow-up. GRBs, if they occur, can be detected up to large distances. In table 7, we give the number of BNS mergers, and the median and maximum redshifts corresponding to a particular $\Delta\Omega$ threshold. With networks that have just one XG detector, BNS events can be localized to $100\,\mathrm{deg}^2$ in the sky up to a redshift of $z = 2.2$. At a similar redshift, 4020ET can localize the event to $1\,\mathrm{deg}^2$, and events as far as $z = 8.8$ can be localized to $100\,\mathrm{deg}^2$. Thus, XG detector networks will be capable of informing EM telescopes with precise sky localizations even for far-away events allowing them to follow up, and potentially observe, GRBs that accompany BNS mergers [66].

Considering the specifications of the current and planned EM telescopes, kilonovae are not expected to be detected beyond $z = 0.5$ [27, 49]. Thus, for BNS and NSBH mergers, we select the sub-population of events that lie within $z = 0.5$ and look at the ability of the different detector networks in terms of 3D localization as well as early-warning alerts. In particular, figures 7 and 8 show the localization of BNS and NSBH events belonging to the sub-population, respectively. The corresponding numbers are presented in tables 8 and 9. While a network with three A$^\sharp$ observatories will detect 1000 BNS and NSBH mergers every year that are localized to within $100\,\mathrm{deg}^2$, a network with at least two XG observatories will detect almost all BNS and NSBH mergers within $z = 0.5$ with this precision. We do not see a considerable improvement in the number of events detected with $\Delta\Omega \leqslant 100\,\mathrm{deg}^2$ when going from networks with one XG observatory to a network with three XG observatories. A drastic improvement is only seen when we consider smaller localizations, e.g. networks with one XG

Table 7. # of BNS mergers every year, and the median and maximum redshift up to which the events are detected associated with the particular $\Delta\Omega$ criteria. These numbers were calculated using the median local merger rates for BNS (320 $\mathrm{Gpc^3 yr^{-1}}$).

	0 XG	1 XG			2 XG			3 XG
Quantity	HLA	HLET	20LA	40LA	20LET	40LET	4020A	4020ET
				$\Delta\Omega \leqslant 1\,\mathrm{deg}^2$				
Number	5	24	17	18	160	250	100	754
Median z	0.06	0.09	0.07	0.08	0.10	0.13	0.11	0.19
Maximum z	0.10	0.16	0.13	0.13	0.23	0.287	0.243	0.503
				$\Delta\Omega \leqslant 10\,\mathrm{deg}^2$				
Number	320	1200	870	980	6200	9400	4000	28 000
Median z	0.15	0.21	0.22	0.20	0.36	0.41	0.33	0.60
Maximum z	0.36	0.53	0.52	0.53	1.1	1.30	1.06	2.12
				$\Delta\Omega \leqslant 100\,\mathrm{deg}^2$				
Number	1200	28 000	25 000	34 000	150 000	230 000	110 000	360 000
Median z	0.21	0.60	0.63	0.68	1.03	1.19	0.98	1.35
Maximum z	0.52	2.12	2.23	2.23	3.68	5.89	3.65	8.80

observatory detect $\mathcal{O}(10)$ events with $\Delta\Omega \leqslant 1\,\mathrm{deg}^2$, networks with two or more XG observatories detect $\mathcal{O}(100)$ such events. A similar trend is seen for luminosity distance errors, where networks with only one XG observatory detect $\mathcal{O}(1)$ events for which luminosity distance is measured to sub-percent precision, whereas this number increases to $\mathcal{O}(10)$ events for a three-XG network. ET is particularly good at sky localization due to its better low-frequency sensitivity compared to others as signals last longer in its sensitivity band, which in turn causes amplitude modulation due to the changing antenna pattern in the direction of the source.

Another important step towards increasing the efficiency of the EM follow-up is the timely communication of the localization of the merger event to EM telescopes. BNS and NSBH mergers can remain in the sensitive band of the GW networks long enough such that the telescopes can be alerted about the merger even before the detection. However, the earlier the alert is sent, the lesser the amount of information that was extracted from the GW signal, leading to worse sky localization compared to if the alert was sent at the time of merger. This results in the trade-off between how early an alert is sent, and how well the event can be localized at that time. In figures 9 and 10, we show the number of events BNS and NSBH events for which the threshold SNR for detection is already achieved 60 s, 120 s, 300 s, and 600 s before the merger, and the corresponding SNR and $\Delta\Omega$ for these events at that time. We assume that the early-warning alerts are communicated when the threshold is reached. The corresponding numbers are listed in tables 10 and 11. We see that the prospects of sending early-warning alerts with the A$^\sharp$ network are not promising, with only 10 BNS events and no NSBH events for which the alert can be sent 1 minute before the merger. This improves drastically for networks with two or more XG detectors, where the alerts can be sent 60 s prior to the merger for $\mathcal{O}(1000)$ BNS and NSBH detections, for each of which $\Delta\Omega \leqslant 100\,\mathrm{deg}^2$. In fact, for the same sky localization, alerts can be sent for $\mathcal{O}(100)$ BNS mergers and $\mathcal{O}(10)$ NSBH mergers 10 min before the merger.

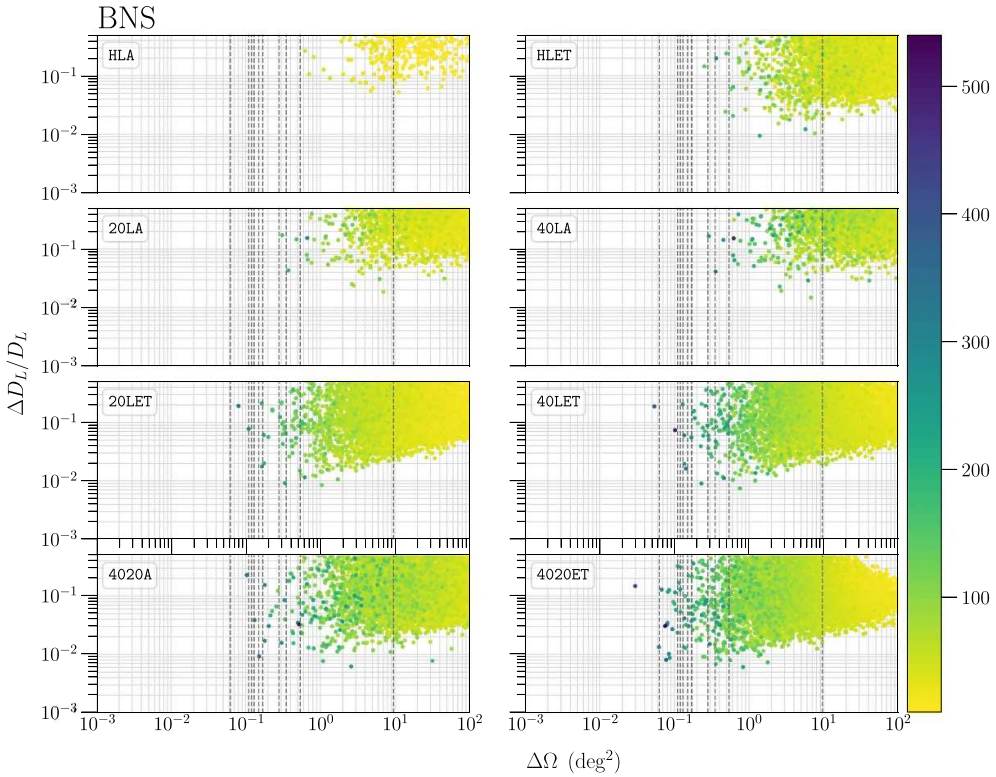

Figure 7. The figure shows the relationship between the fractional error in the luminosity distance $\Delta D_L/D_L$, 90%-credible sky area $\Delta\Omega$ and the SNR (denoted by the color bar) for BNS events up to $z = 0.5$. Each of these events, detected in an observation span of 1 year, appears as a spot placed according to the associated measurement errors in luminosity distance and sky position. The color of the dots represents the SNR with which that particular event was detected in a GW detector network. The vertical dotted lines correspond to the FOV of the EM telescopes listed in table 5.

5. Open science questions uniquely addressed by GW observations

A number of White Papers and design study reports have documented the scientific potential of current and future GW observatories. For recent reviews see the following [67–69]. In this section, we summarize the science questions of interest to a diverse community of physicists and astronomers and could be addressed by GW observations. In later sections, we will match these questions to specific networks that can answer them effectively.

5.1. Black holes and neutron stars throughout the cosmos

The improved sensitivities of the next-generation networks will not only allow the detection of compact binaries up to larger distances but will also result in the improved estimation of binary parameters (see section 4). The precise measurement of binary parameters is essential to infer the source properties which will inform us about the formation of such binaries. There is already some evidence that the observed variety of source properties is likely the result of multiple astrophysical formation channels [70–73]. The peak of the mass function, and its

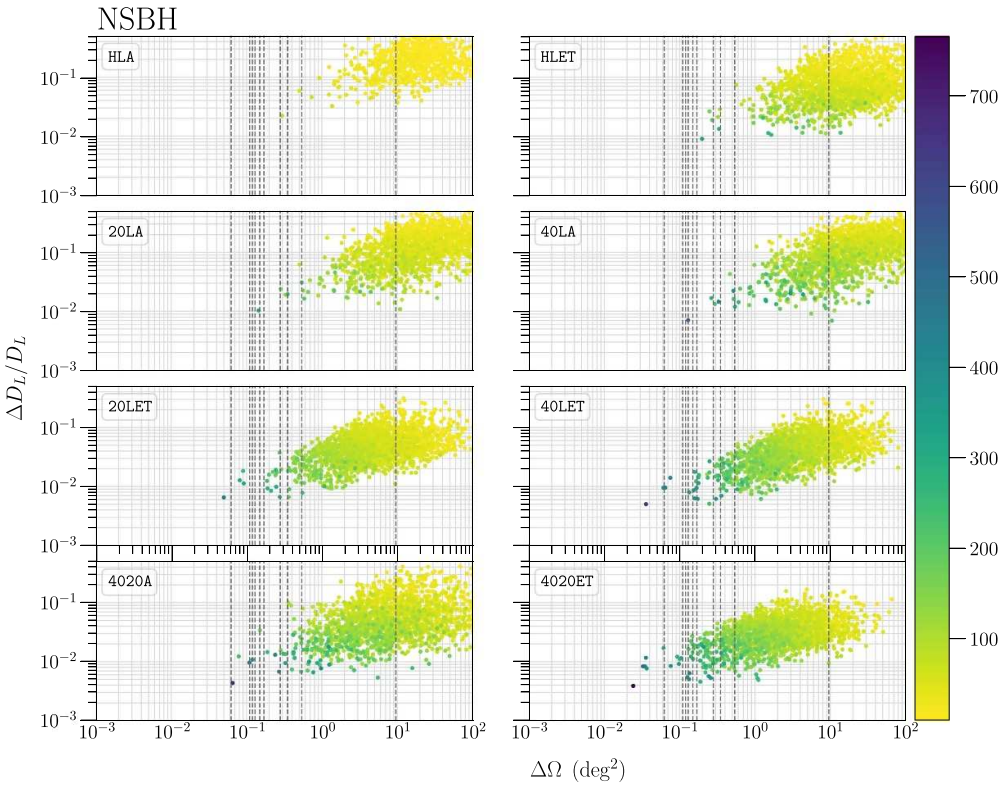

Figure 8. The figure shows the relationship between the fractional error in luminosity distance $\Delta D_L/D_L$, 90%-credible sky area $\Delta\Omega$ and the SNR (denoted by the color bar) of NSBH events for which $z<0.5$. Each of these events, detected in an observation span of 1 year, appears as a spot placed according to the associated measurement errors in luminosity distance and sky position. The color of the dots represents the SNR with which that particular event was detected in a GW detector network. The vertical dotted lines correspond to the FOV of multiple EM telescopes listed in table 5.

variation with redshift, contains crucial clues about binary evolution and the final stages of the life of massive stars [74–80].

5.1.1. BBH, BNS and NSBH mergers. From figure 2 and table 4, we see that a network with no XG detectors will only observe $\sim$0.1%, 1% and 15% of the cosmic BNS, NSBH and BBH population, respectively. This is drastically improved for a network with 2 CE detectors, detecting $\sim$30%, 66% and 95% of all BNS, NSBH and BBH mergers, respectively. Further, a network with at least 2 XG detectors will be able to detect BNS systems up to the peak of the star formation rate ($z\sim2$), and NSBH mergers well beyond it. In fact, BBH mergers with such a network can be observed beyond $z=20$, i.e. even prior to 200 Myr after the Big Bang. It is important to note that CE40 really shines compared to CE20 and ET when it comes to detecting events at large distances. This is evident in table 4, where the reach and the detection rates for 40LA are better than not just 20LA and HLET, but even the 20LET network. The improvement in the depth of observation will provide information about the delay time distribution between the formation and the merger of the compact binary [81], and thereby

Table 8. For the BNS sub-population with events for which $z < 0.5$, the table lists the number of detections per year for the eight detector networks with 90%-credible sky area $\Delta\Omega < 10$, 1, 0.1 and 0.01 deg^2 and fractional error in luminosity distance $\Delta D_L/D_L < 0.1$ and 0.01.

Metric	$\Delta\Omega(\mathrm{deg})^2$					$\Delta D_L/D_L$	
Quality	$\leqslant$100	$\leqslant$10	$\leqslant$1	$\leqslant$0.1	$\leqslant$0.01	$\leqslant$0.1	$\leqslant$0.01
HLA	$1.2^{+1.8}_{-0.9} \times 10^3$	$3.2^{+4.7}_{-2.5} \times 10^2$	$5.0^{+11.0}_{-5.0} \times 10^0$	0	0	$2.6^{+4.2}_{-2.3} \times 10^1$	0
HLET	$1.0^{+1.5}_{-0.8} \times 10^4$	$1.2^{+1.8}_{-0.9} \times 10^3$	$2.4^{+4.7}_{-2.1} \times 10^1$	$0.0^{+3.0}_{-0.0} \times 10^0$	0	$2.3^{+3.4}_{-1.7} \times 10^3$	$1.0^{+2.0}_{-1.0} \times 10^0$
20LA	$8.6^{+13.3}_{-6.4} \times 10^3$	$8.6^{+12.9}_{-6.8} \times 10^2$	$1.7^{+3.3}_{-1.5} \times 10^1$	0	0	$2.4^{+4.2}_{-1.9} \times 10^2$	0
40LA	$9.8^{+15.1}_{-7.3} \times 10^3$	$9.7^{+14.6}_{-7.6} \times 10^2$	$1.8^{+3.8}_{-1.6} \times 10^1$	0	0	$3.1^{+5.4}_{-2.4} \times 10^2$	$0.0^{+2.0}_{-0.0} \times 10^0$
20LET	$1.5^{+2.3}_{-1.1} \times 10^4$	$4.9^{+7.4}_{-3.7} \times 10^3$	$1.6^{+2.4}_{-1.3} \times 10^2$	$1.0^{+6.0}_{-1.0} \times 10^0$	0	$4.4^{+6.9}_{-3.3} \times 10^3$	$2.0^{+6.0}_{-2.0} \times 10^0$
40LET	$1.6^{+2.4}_{-1.2} \times 10^4$	$6.3^{+9.7}_{-4.8} \times 10^3$	$2.5^{+3.8}_{-2.0} \times 10^2$	$1.0^{+9.0}_{-1.0} \times 10^0$	0	$4.9^{+7.7}_{-3.7} \times 10^3$	$2.0^{+9.0}_{-2.0} \times 10^0$
4020A	$1.4^{+2.1}_{-1.0} \times 10^4$	$3.4^{+5.3}_{-2.6} \times 10^3$	$9.7^{+15.7}_{-7.7} \times 10^1$	$0.0^{+4.0}_{-0.0} \times 10^0$	0	$4.5^{+6.9}_{-3.4} \times 10^3$	$4.0^{+11.0}_{-4.0} \times 10^0$
4020ET	$1.6^{+2.5}_{-1.2} \times 10^4$	$1.0^{+1.5}_{-0.8} \times 10^4$	$7.5^{+11.4}_{-5.8} \times 10^2$	$1.3^{+2.9}_{-1.2} \times 10^1$	$0.0^{+2.0}_{-0.0} \times 10^0$	$8.5^{+13.1}_{-6.4} \times 10^3$	$1.2^{+2.2}_{-1.2} \times 10^1$

Table 9. For the NSBH sub-population with events for which $z < 0.5$, the table lists the number of detections per year for the eight detector networks with 90%-credible sky area $\Delta\Omega < 10$, 1, 0.1 and 0.01 deg^2 and fractional error in luminosity distance $\Delta D_L/D_L < 0.1$ and 0.01.

Metric	$\Delta\Omega(\mathrm{deg})^2$					$\Delta D_L/D_L$	
Quality	$\leqslant 100$	$\leqslant 10$	$\leqslant 1$	$\leqslant 0.1$	$\leqslant 0.01$	$\leqslant 0.1$	$\leqslant 0.01$
HLA	$9.4^{+19.7}_{-8.1} \times 10^2$	$2.2^{+5.3}_{-1.9} \times 10^2$	$4.0^{+13.0}_{-4.0} \times 10^0$	0	0	$1.4^{+3.6}_{-1.3} \times 10^2$	0
HLET	$2.0^{+4.3}_{-1.7} \times 10^3$	$6.9^{+15.0}_{-6.0} \times 10^2$	$1.6^{+6.8}_{-1.6} \times 10^1$	$0.0^{+1.0}_{-0.0} \times 10^0$	0	$1.5^{+3.2}_{-1.3} \times 10^3$	$1.0^{+17.0}_{-1.0} \times 10^0$
20LA	$1.9^{+4.1}_{-1.6} \times 10^3$	$5.3^{+11.0}_{-4.5} \times 10^2$	$1.5^{+4.4}_{-1.5} \times 10^1$	0	0	$7.4^{+16.0}_{-6.3} \times 10^2$	$0.0^{+6.0}_{-0.0} \times 10^0$
40LA	$2.0^{+4.2}_{-1.6} \times 10^3$	$5.8^{+12.3}_{-5.0} \times 10^2$	$1.8^{+5.5}_{-1.8} \times 10^1$	0	0	$9.7^{+20.7}_{-8.2} \times 10^2$	$3.0^{+31.0}_{-3.0} \times 10^0$
20LET	$2.3^{+4.9}_{-1.9} \times 10^3$	$1.6^{+3.4}_{-1.3} \times 10^3$	$1.4^{+3.4}_{-1.2} \times 10^2$	$4.0^{+7.0}_{-4.0} \times 10^0$	0	$2.1^{+4.5}_{-1.7} \times 10^3$	$1.4^{+6.1}_{-1.3} \times 10^1$
40LET	$2.3^{+4.9}_{-1.9} \times 10^3$	$1.8^{+3.8}_{-1.5} \times 10^3$	$2.3^{+5.4}_{-2.0} \times 10^2$	$4.0^{+10.0}_{-4.0} \times 10^0$	0	$2.1^{+4.6}_{-1.8} \times 10^3$	$3.5^{+11.4}_{-2.8} \times 10^1$
4020A	$2.2^{+4.8}_{-1.8} \times 10^3$	$1.3^{+2.6}_{-1.1} \times 10^3$	$1.0^{+2.2}_{-0.9} \times 10^2$	$2.0^{+4.0}_{-2.0} \times 10^0$	0	$1.8^{+4.0}_{-1.6} \times 10^3$	$2.3^{+9.1}_{-2.0} \times 10^1$
4020ET	$2.3^{+4.9}_{-1.9} \times 10^3$	$2.1^{+4.5}_{-1.7} \times 10^3$	$5.0^{+10.9}_{-4.2} \times 10^2$	$9.0^{+46.0}_{-9.0} \times 10^0$	0	$2.3^{+4.9}_{-1.9} \times 10^3$	$6.2^{+19.8}_{-5.4} \times 10^1$

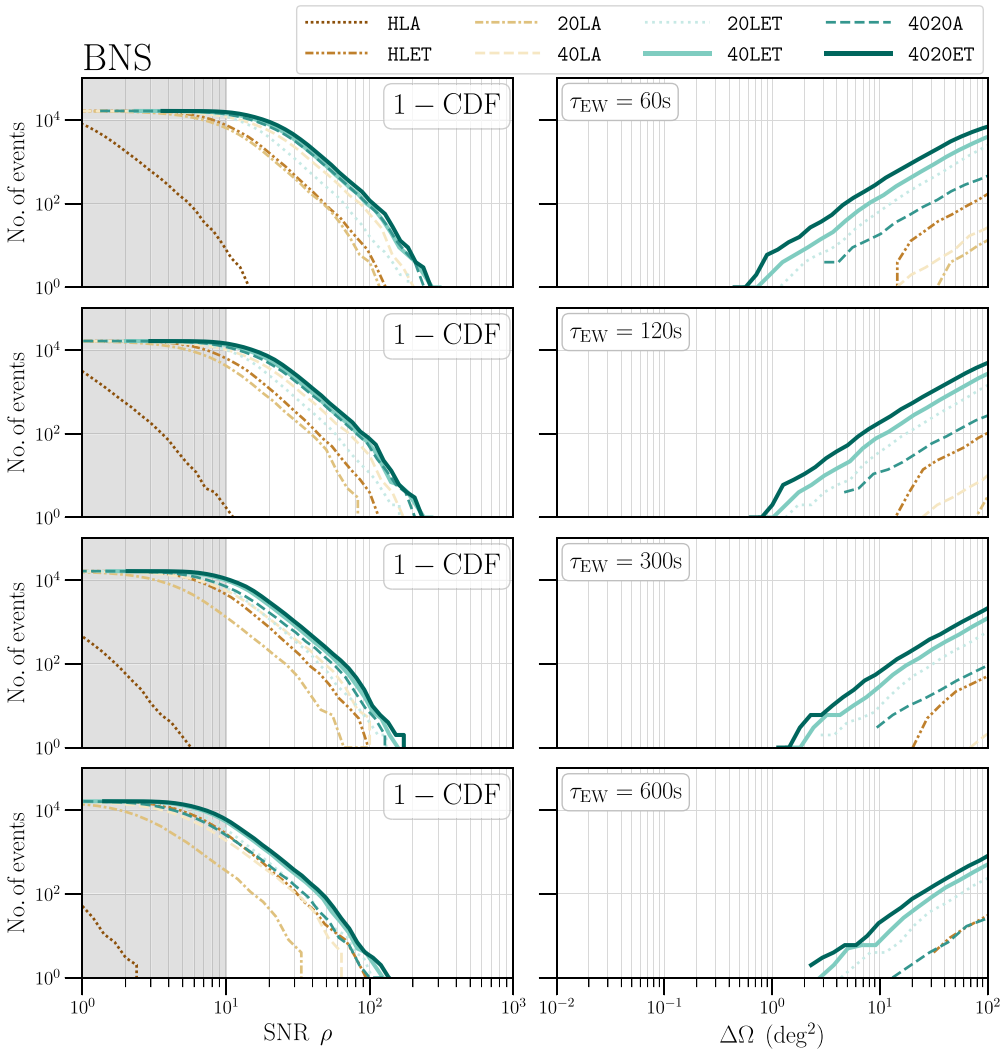

Figure 9. The scaled CDF plots for BNS events belonging to the multimessenger subpopulation for which early-warning alerts can be sent 1 min, 2 min, 5 min, and 10 min before their respective mergers.

allow the inference of the history of chemical evolution in the Universe beyond the reach of multi-messenger astronomy [82].

Apart from the detection itself, the source-frame masses of compact objects can be measured with unprecedented precision with the help of XG detectors. From table 1, we note that only a network with at least 2 XG detectors can detect BNS mergers beyond $z \geqslant 1$ such that the uncertainty in the redshift and the source-frame mass measurements is within 20% and 30%, respectively. Such measurements are important in order to measure the mass function associated with this class of binaries close to the star formation peak. Similarly, astrophysical channels for the formation and merger of BBH systems at high redshifts can be studied using GW detections with precise mass measurements for BBH systems beyond $z = 10$. Table 1 shows that the number of such mergers increases from 0 to $\mathcal{O}(10)$ to $\mathcal{O}(100)$ every year with a

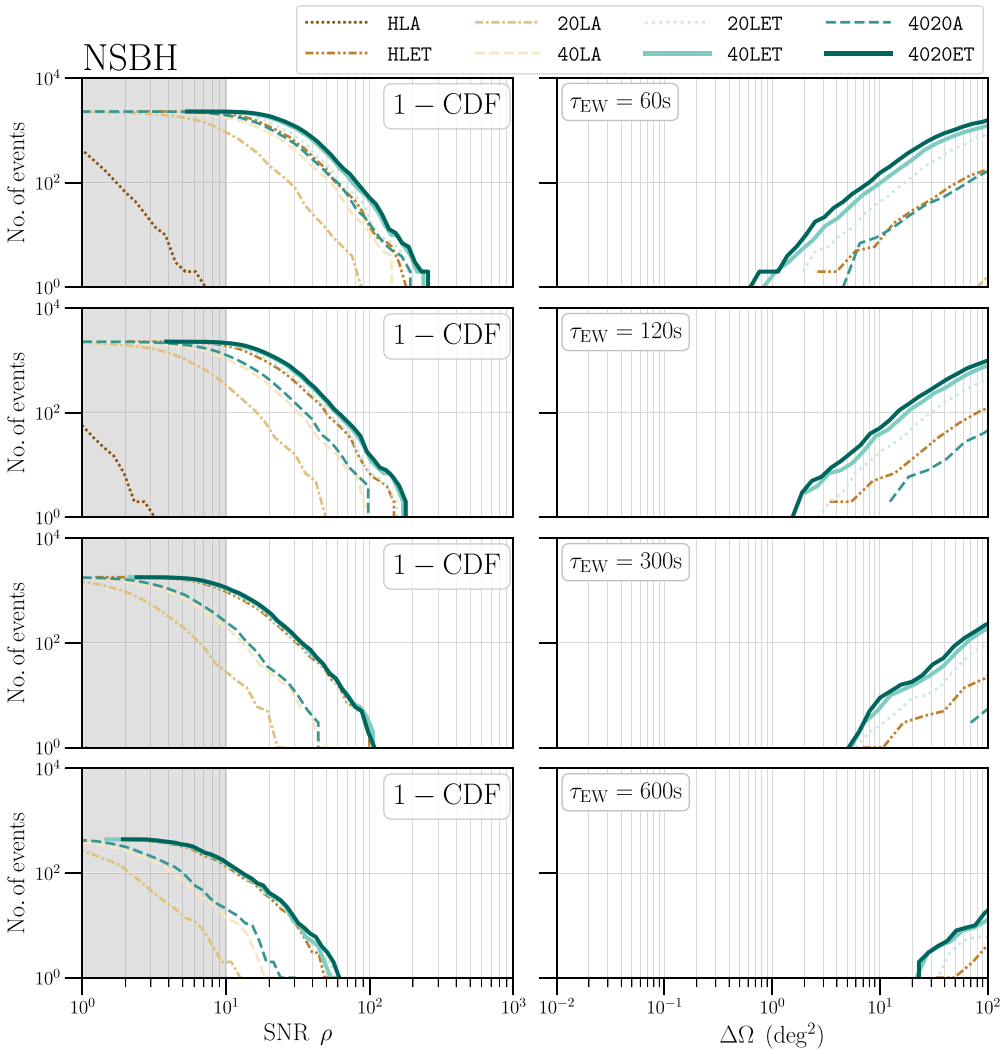

Figure 10. The scaled CDF plots for NSBH events belonging to the multimessenger subpopulation for which early-warning alerts can be sent 1 min, 2 min, 5 min, and 10 min before their respective mergers.

network with no XG, 1 XG and 3 XG detectors, respectively. In addition, recall that we chose the mass spectrum of the BNS population to follow a double Gaussian (see section 3) in order to see if the second Gaussian feature $(\mu = 1.8\,\mathrm{M}_\odot, \sigma = 0.3\,\mathrm{M}_\odot)$ could be inferred with GW detections. From table 1, we conclude that for BNS systems with $m_1 \geqslant 1.5\,\mathrm{M}_\odot$, only networks with at least 1 XG detector can detect systems such the source-frame mass of the primary component is measured to better than 10% precision.

5.1.2. IMBBH, Pop-III BBH and PBH mergers. Constraining the BH mass function above 50 $\mathrm{M}_\odot$ will allow for a better understanding of the pair instability supernova mass gap (and of the nuclear physics processes that lead to it) [83, 84]; the rate of hierarchical mergers [85, 86];

Table 10. The number of BNS detections per year for the GW detector networks for which an EW alert can be sent 60 s, 120 s, 300 s and 600 s before the merger, with 90%-credible sky area measured to be better than 100, 10, 1 deg^2 at the time when the alert is sent.

EW Time	$\tau_{\rm EW} = 60$ s			$\tau_{\rm EW} = 120$ s		
$\Delta\Omega\,(\mathrm{deg}^2)$	$\leqslant$100	$\leqslant$10	$\leqslant$1	$\leqslant$100	$\leqslant$10	$\leqslant$1
HLA	$0.0^{+1.0}_{-0.0} \times 10^0$	0	0	0	0	0
HLET	$1.3^{+2.4}_{-1.1} \times 10^2$	$1.0^{+10.0}_{-1.0} \times 10^0$	0	$8.3^{+15.7}_{-6.9} \times 10^1$	$1.0^{+5.0}_{-1.0} \times 10^0$	0
20LA	$5.0^{+10.0}_{-4.0} \times 10^0$	0	0	$2.0^{+1.0}_{-1.0} \times 10^0$	0	0
40LA	$7.0^{+19.0}_{-6.0} \times 10^0$	0	0	$3.0^{+6.0}_{-2.0} \times 10^0$	0	0
20LET	$2.0^{+3.2}_{-1.6} \times 10^3$	$4.9^{+9.7}_{-4.0} \times 10^1$	$1.0^{+3.0}_{-1.0} \times 10^0$	$1.2^{+1.8}_{-0.9} \times 10^3$	$3.0^{+5.5}_{-2.4} \times 10^1$	$0.0^{+2.0}_{-0.0} \times 10^0$
40LET	$3.4^{+5.2}_{-2.6} \times 10^3$	$1.2^{+1.9}_{-0.9} \times 10^2$	$2.0^{+4.0}_{-2.0} \times 10^0$	$2.3^{+3.5}_{-1.7} \times 10^3$	$7.4^{+12.0}_{-6.3} \times 10^1$	$1.0^{+2.0}_{-1.0} \times 10^0$
4020A	$3.7^{+6.2}_{-2.8} \times 10^2$	$1.5^{+2.3}_{-1.2} \times 10^1$	0	$2.2^{+3.1}_{-1.7} \times 10^2$	$1.1^{+1.0}_{-0.9} \times 10^1$	0
4020ET	$6.3^{+9.4}_{-4.7} \times 10^3$	$2.7^{+4.5}_{-2.1} \times 10^2$	$5.0^{+12.0}_{-4.0} \times 10^0$	$4.4^{+6.6}_{-3.3} \times 10^3$	$1.5^{+2.6}_{-1.2} \times 10^2$	$1.0^{+4.0}_{-1.0} \times 10^0$
EW Time	$\tau_{\rm EW} = 300$s			$\tau_{\rm EW} = 600$s		
$\Delta\Omega\,(\mathrm{deg}^2)$	$\leqslant$100	$\leqslant$10	$\leqslant$1	$\leqslant$100	$\leqslant$10	$\leqslant$1
HLA	0	0	0	0	0	0
HLET	$4.2^{+7.9}_{-3.5} \times 10^1$	$0.0^{+2.0}_{-0.0} \times 10^0$	0	$2.4^{+4.3}_{-1.9} \times 10^1$	$0.0^{+1.0}_{-0.0} \times 10^0$	0
20LA	0	0	0	0	0	0
40LA	0	0	0	0	0	0
CE20LET	$4.7^{+7.6}_{-3.6} \times 10^2$	$7.0^{+26.0}_{-6.0} \times 10^0$	0	$2.0^{+3.2}_{-1.6} \times 10^2$	$4.0^{+11.0}_{-4.0} \times 10^0$	0
40LET	$1.0^{+15.9}_{-0.8} \times 10^3$	$2.2^{+53.0}_{-1.7} \times 10^1$	$0.0^{+1.0}_{-0.0} \times 10^0$	$4.1^{+6.7}_{-3.2} \times 10^2$	$6.0^{+22.0}_{-5.0} \times 10^0$	0
4020A	$6.2^{+8.5}_{-5.2} \times 10^1$	$2.0^{+0.0}_{-2.0} \times 10^0$	0	$1.9^{+2.0}_{-1.6} \times 10^1$	0	0
4020ET	$1.8^{+28.6}_{-1.4} \times 10^3$	$5.2^{+9.3}_{-4.3} \times 10^1$	$0.0^{+2.0}_{-0.0} \times 10^0$	$6.8^{+11.2}_{-5.3} \times 10^2$	$1.5^{+3.7}_{-1.2} \times 10^1$	$0.0^{+1.0}_{-0.0} \times 10^0$

and IMBH [87, 88]. Massive BBH systems can also result from high-redshift formation channels, e.g. PBHs created during the inflationary epoch of the Universe [89–92], and Pop III stars [93]. The mass functions of both PBH and remnants of Pop III stars are uncertain; but they might be the seeds that formed the supermassive BHs found at the centers of most galaxies [87, 94–97]. Thus, detecting these mergers will allow us to explore one of the most pressing open questions in galaxy and structure formation.

The major hurdle in detecting IMBBH systems or binaries at large redshifts is the large detector-frame chirp mass, which leads to low merger frequencies. These mergers lie predominantly in the range where the detectors are less sensitive. The low-frequency ($\sim$10 Hz) sensitivity increases by more than an order of magnitude when going from A$^\sharp$ to XG detectors (see figure 1), thus, improving the chances of detecting these events. However, the detection itself is only the first step. For IMBBH mergers, we are also interested in seeing if GW networks can precisely measure the source-frame masses so as to unravel the mass spectrum of these events. On the other hand, for PBH and Pop III mergers, along with the source-frame mass, one would also need a precise measurement of the redshift in order to differentiate these high-redshift mergers from IMBBH mergers at $z \leqslant 10$.

Figure 11 shows the error in the source-frame mass of the components of IMBBH mergers as a function of the injected source-frame mass and redshift. Note that while the fractional error on the mass measurement can be as low as $\sim$0.01%, such precision is likely to be achievable only with networks containing at least 2 XG detectors. The A$^\sharp$ network is able to detect $\sim$40% of the mergers, whereas networks with at least 1 XG detector can detect more than 90% of these events, with HLET itself being able to detect $\sim$98%. The stellar performance of ET is attributed to better sensitivities in the $f < 10$ Hz region compared to CE40 and CE20. While

Table 11. The number of NSBH detections per year for the GW detector networks for which an EW alert can be sent 60 s, 120 s, 300 s and 600 s before the merger, with 90%-credible sky area measured to be better than 100, 10, 1 deg^2 at the time when the alert is sent.

EW Time	$\tau_{\rm EW} = 60$ s			$\tau_{\rm EW} = 120$ s		
$\Delta\Omega\,(\mathrm{deg}^2)$	$\leqslant$100	$\leqslant$10	$\leqslant$1	$\leqslant$100	$\leqslant$10	$\leqslant$1
HLA	0	0	0	0	0	0
HLET	$1.6^{+3.2}_{-1.4}\times10^{2}$	$6.0^{+22.0}_{-5.0}\times10^{0}$	0	$9.2^{+20.5}_{-8.2}\times10^{1}$	$3.0^{+10.0}_{-3.0}\times10^{0}$	0
20LA	$0.0^{+1.0}_{-0.0}\times10^{0}$	0	0	0	0	0
40LA	$0.0^{+1.0}_{-0.0}\times10^{0}$	0	0	0	0	0
20LET	$7.7^{+16.5}_{-6.6}\times10^{2}$	$3.5^{+10.8}_{-3.4}\times10^{1}$	$0.0^{+1.0}_{-0.0}\times10^{0}$	$3.9^{+8.7}_{-3.4}\times10^{2}$	$1.3^{+4.3}_{-1.2}\times10^{1}$	$0.0^{+1.0}_{-0.0}\times10^{0}$
40LET	$1.2^{+2.5}_{-1.0}\times10^{3}$	$8.1^{+20.9}_{-7.2}\times10^{1}$	$2.0^{+4.0}_{-2.0}\times10^{0}$	$7.2^{+15.4}_{-6.2}\times10^{2}$	$3.3^{+10.6}_{-3.0}\times10^{1}$	$0.0^{+1.0}_{-0.0}\times10^{0}$
4020A	$1.3^{+3.1}_{-1.2}\times10^{2}$	$9.0^{+14.0}_{-7.0}\times10^{0}$	0	$3.9^{+10.6}_{-3.2}\times10^{1}$	$0.0^{+3.0}_{-0.0}\times10^{0}$	0
4020ET	$1.5^{+3.3}_{-1.2}\times10^{3}$	$1.3^{+3.1}_{-1.1}\times10^{2}$	$2.0^{+7.0}_{-2.0}\times10^{0}$	$9.3^{+19.8}_{-7.9}\times10^{2}$	$4.8^{+14.1}_{-4.5}\times10^{1}$	$0.0^{+1.0}_{-0.0}\times10^{0}$
EW Time	$\tau_{\rm EW} = 300$s			$\tau_{\rm EW} = 600$s		
$\Delta\Omega\,(\mathrm{deg}^2)$	$\leqslant$100	$\leqslant$10	$\leqslant$1	$\leqslant$100	$\leqslant$10	$\leqslant$1
HLA	0	0	0	0	0	0
HLET	$1.9^{+68.0}_{-1.7}\times10^{1}$	$1.0^{+2.0}_{-1.0}\times10^{0}$	0	$2.0^{+10.0}_{-2.0}\times10^{0}$	$0.0^{+2.0}_{-0.0}\times10^{0}$	0
20LA	0	0	0	0	0	0
40LA	0	0	0	0	0	0
20LET	$7.6^{+19.6}_{-6.8}\times10^{1}$	$2.0^{+7.0}_{-2.0}\times10^{0}$	0	$7.0^{+29.0}_{-7.0}\times10^{0}$	$0.0^{+2.0}_{-0.0}\times10^{0}$	0
40LET	$1.6^{+34.7}_{-1.4}\times10^{2}$	$4.0^{+11.0}_{-4.0}\times10^{0}$	0	$1.1^{+5.2}_{-1.1}\times10^{1}$	$0.0^{+2.0}_{-0.0}\times10^{0}$	0
4020A	$2.0^{+8.0}_{-2.0}\times10^{0}$	0	0	$0.0^{+1.0}_{-0.0}\times10^{0}$	0	0
4020ET	$2.0^{+44.5}_{-1.8}\times10^{2}$	$5.0^{+22.0}_{-5.0}\times10^{0}$	0	$1.7^{+6.1}_{-1.7}\times10^{1}$	$0.0^{+3.0}_{-0.0}\times10^{0}$	0

the CE detectors do not seem to help ET significantly in detecting IMBBH sources, they aid in the precise estimation of component masses.

Figures 12 and 13 show the errors in source-frame components masses and the redshift for PBH systems beyond $z = 25$ and Pop III BBH systems, respectively. It is improbable that a network with no XG detectors will be able to detect any such mergers. In the case of PBH, we see that 40 (45) mergers will be detected every year with 40LET (4020ET) such that the redshift measurement excludes $z = 15$ $(z = 20)$ at the 1σ level. Even one such detection will be the smoking gun evidence in favor of the existence of PBHs. For the Pop III case, we note that CE40 outperforms CE20 and ET. The 40LA network is itself able to detect the furthest simulated merger detected by 4020ET, which occurs around $z = 25$. However, the merit of having more than 1 XG detector in the network becomes apparent when we consider the measurement accuracy of source-frame masses and redshift. Beyond $z = 10$, 40LA detects just 1 event with $\Delta m/m \leqslant 10\%$, whereas 4020A and 4020ET detect $\mathcal{O}(10)$ and $\mathcal{O}(100)$ such events, respectively. In fact, beyond this redshift, 40LA detects $\mathcal{O}(10)$ mergers with $\Delta z/z \leqslant 10\%$, whereas 4020A and 4020ET detect 8 and 40 times as many mergers, respectively.

The era of the XG GW observatories will observe the cosmic population of compact binary mergers like BBH, BNS and NSBH, only a glimpse of which is already seen by current networks. In addition, only networks with XG observatories will be capable of unraveling elusive compact binary populations, like those corresponding to Pop III and primordial BHs, which will greatly improve our understanding of various astrophysical processes involved in star, galaxy and structure formation, and the Universe as a whole.

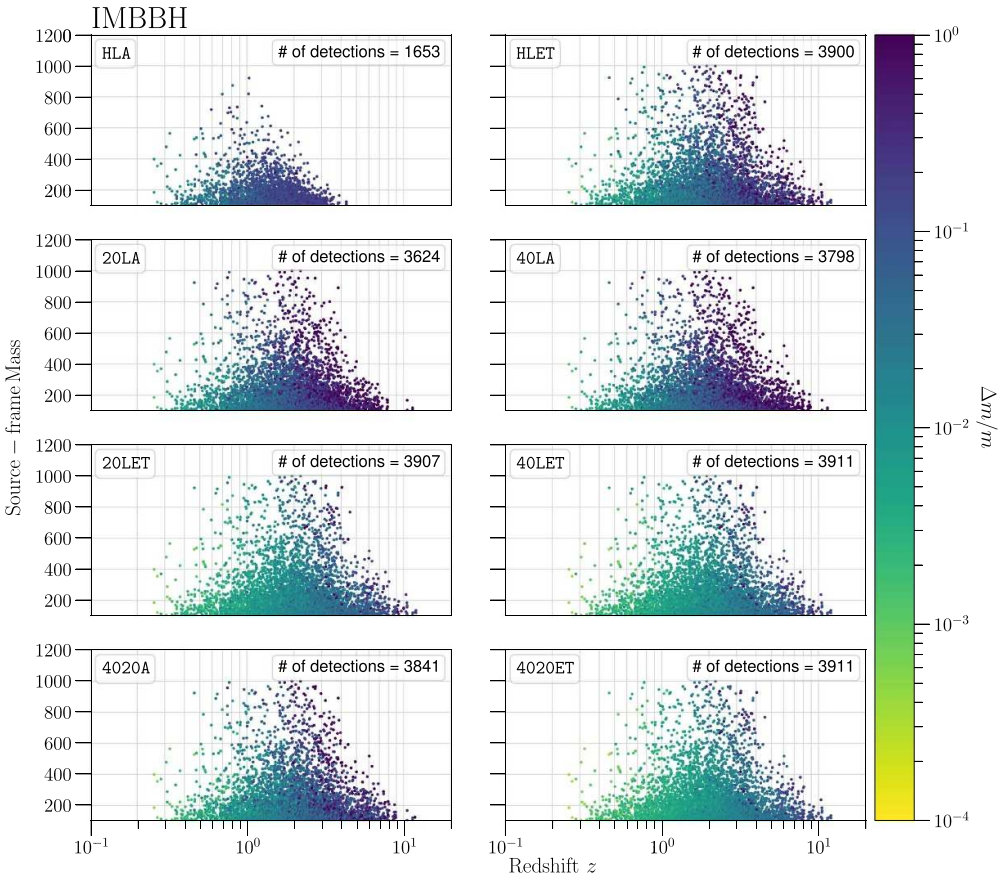

Figure 11. The plot shows the fractional error in the measurement of source-frame component masses for IMBBH mergers as a function of the source-frame mass and the redshift, along with the number of such systems detected by each detector network in the span of 1 year.

5.2. Multimessenger astrophysics and dynamics of dense matter

NSs are among the most exotic objects in the stellar graveyard. They are characterized by a unique relationship between the associated pressure and the energy density, called the EoS. With the EoS, one can link the mass with the radius of the NS by solving the Tolman–Oppenheimer–Volkoff equation. NSs in binary configurations with a companion NS or BH can get tidally disrupted by the gravity of their companion close to the merger. The effect of the disruption on the phase of the GW waveform near merger can be described, to leading order, using the tidal deformability (Λ) of the NS. Λ can be uniquely determined with the knowledge of the EoS and the mass of the NS. Inversely, the measurement of Λ and the mass of the NS from GW observations can be used to obtain constraints on the EoS that governs NS.

The disruption of merging NSs in binaries can result in the production of non-relativistic to mildly-relativistic neutron-rich debris, and relativistic jets. These ejecta can power a variety of EM counterparts, including UV-optical-IR kilonovae, late-time radio flares from fast kilonova tails, GRBs, and their radio-to-x-ray afterglows (e.g. [98–106]). As demonstrated spectacularly

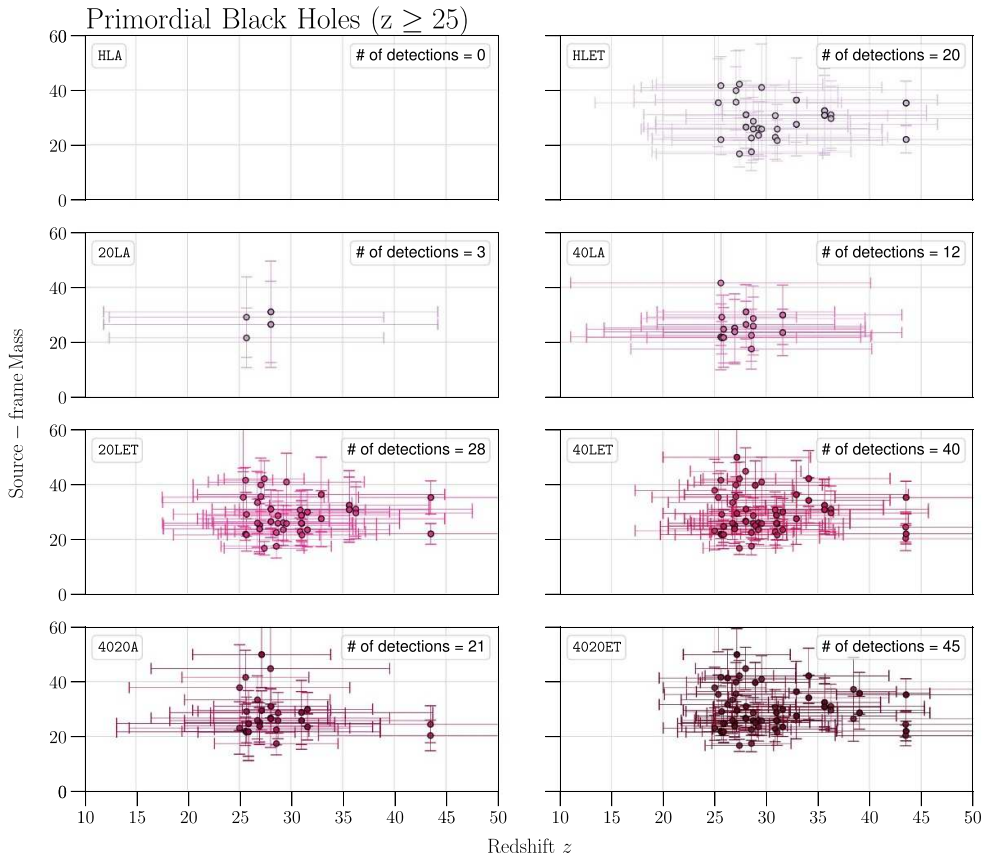

Figure 12. The plot shows the number of primordial black holes lying further than $z = 25$ that are detected by each detector network, along with the measurement errors in the inference of the source-frame masses and the redshift for each event. The numbers correspond to an observation span of 1 year.

by the case of GW170817 [107–109], multi-messenger observations can paint a very detailed picture of BNS progenitors and ejecta [107–124].

In the WP, we have shown how XG GW detectors will enable major breakthroughs in multi-messenger astrophysics and in our understanding of the dynamics of dense matter. In the remainder of this section we summarize our previous findings, highlighting the specific results of the trade study presented here that support the conclusions drawn in the WP.

5.2.1. Multimessenger observations and early warnings. Gamma-ray observations of GW170817 have confirmed that at least some short GRBs are associated with BNS mergers [109, 113, 114]. These observations have also enabled measurement of the time delay between the merger (as determined by the GW signal) and the onset of the GRB emission (as determined by the gamma-ray light curve) [109, 113]. As discussed in [125] (and references therein), this delay encodes key physics of the GRB central engine and the ejecta, besides enabling fundamental physics tests [109].

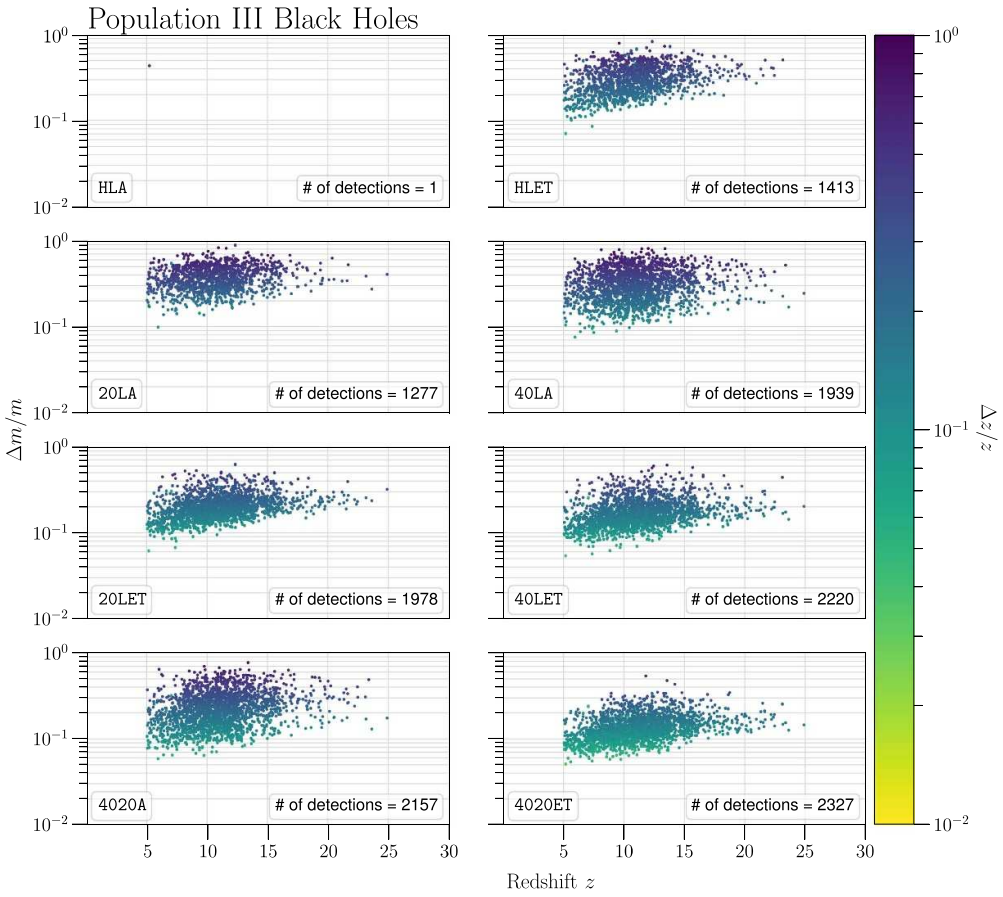

Figure 13. The plot shows the number of Pop-III binary black holes that are detected by each detector network, along with the measurement errors in the inference of redshift as a function of the fractional error in source-frame masses and the redshift corresponding to each event. The numbers correspond to an observation span of 1 year.

As evident from the results reported in table 7, XG detectors will probe GWs from BNS mergers up to the peak of star formation ($z \approx 2$), hence mapping GRBs (and their EM afterglows) to their progenitors, and measuring the GW-GRB time delays in a systematic fashion [109, 113, 114]. We stress that systematically mapping GRBs to their progenitors up to the star formation peak is beyond the reach of 4 km-long GW detectors, and will offer new insight into what physical properties allow for the launch of successful relativistic jets in short GRBs.

XG detectors will also provide exquisite sky localizations ($\lesssim 1\,\mathrm{deg}^2$) for BNS mergers in the local Universe (table 7), hence building a golden sample of GW170817-like events. This golden sample will be critical to explore the diversity of merger outcomes, and map the properties of progenitors and merger remnants to those of their EM counterparts. While 4 km GW detectors can build a sample of GW-kilonova associations in the local Universe taking advantage of wide field-of-view optical telescopes such as Rubin and the Zwicky Transient Facility [58, 126, 127], on theoretical grounds we expect a zoo of EM counterparts to exist, ranging from optically bright and blue kilonovae associated with magnetar remnants and (perhaps) choked jets, to red and dim kilonovae associated with successful jet afterglows (e.g. [117, 128,

129]). The last, when viewed off-axis, could be more easily unveiled at radio wavelengths [115, 130]. The operation of XG observatories will sync with the era of EM telescopes such as the extremely large telescope (ELT) and giant Magellan telescope (GMT) that can probe cosmic distances. Hence, having a few BNS mergers per year with GW sky localizations accessible to the smaller fields of view of the most sensitive EM telescopes [59, 65] (table 5) will probe the diversity of BNS mergers in an optically unbiased way.

Finally, XG detectors will also enable early warnings, thanks to their ability to localize BNSs even before the merger (table 10). This is key to potentially opening new discovery space in multi-messenger astrophysics. In fact, several GRBs are preceded by so-called gamma-ray precursors whose origin remains unclear [131]. Moreover, several theoretical models predict prompt EM emission associated with various mechanisms including NS magnetic field interactions during the inspiral or the collapse of a short-lived NS remnant into a BH (e.g. [132–134] and references therein). These scenarios motivate precise sky localization and early-warning alerts to telescopes before the merger [135, 136].

5.2.2. Measuring the radius of the neutron star. As shown in the WP, XG detectors will revolutionize our knowledge of high-density matter by detecting hundreds of BNS mergers per year with SNR$>$ 100. For these, measurements of NS tides will constrain their radii to better than 100 m, i.e. about one part in a hundred. This will enable population-wide constraints (for the common NS EoS) at the 10 m-level.

Constraining NS radii is of significant importance because it provides crucial insights into the properties of the NS and the nature of matter inside it (for e.g. see [137, 138]). Universal relations are empirical relationships between various physical properties of NSs, which are instrumental in obtaining the NS radii from GW data [108]. GWs contain information on tidal parameters like $\tilde{\Lambda}$, which can be used along with two universal relations to constrain the radius. We describe the procedure for this below.

We use the `GWBENCH` formalism to calculate the covariance matrix of parameters corresponding to BNS events. We use the covariance matrices to generate multi-dimensional Gaussian distribution of the parameters mentioned in section 3.2. The universal relation between symmetric and asymmetric combinations of component tidal deformability, described in [139, 140], is then used to calculate individual tidal deformabilities Λ_1 and Λ_2 from the samples of the combined tidal deformability $\tilde{\Lambda}$ and the mass ratio q. The universal relation between compactness and tidal deformability defined in [140] is used to infer the NS radii from the component tidal deformabilities. EoS-specific corrections have been applied to the tidal deformability and radii distributions which are described in [141].

We combine the events with similar masses to get an effective radius error as a function of mass. For this, we make 20 mass bins from $1\,\mathrm{M}_\odot$ to the maximum mass allowed by the EoS used in our study. We use the $\sqrt{N}$ relationship for combining errors in radii in each mass bin separately [142] and report the cumulative number of events with respect to the radius errors in figure 14.

The present analysis provides preliminary evidence that NS radii can be measured below 1% by using at least one XG detector in combination with the planned upgrades of LIGO-Virgo detectors. CE design with either a 40 km or 20 km arm will observe up to 10% of the BNS events where a radius error is better than 100 m and a few events with errors of even a few tens of meters. With thousands of BNS observations, we are optimistic that a combined error measurement will improve by at least an order of magnitude and aid our understanding of nuclear physics.

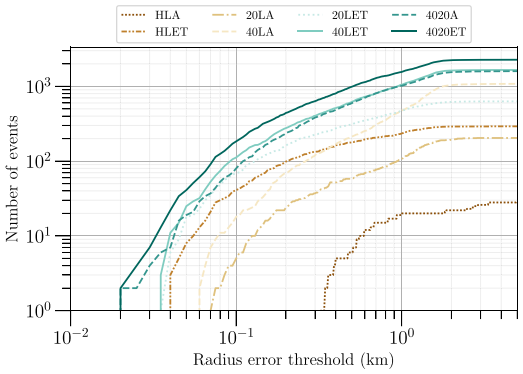

Figure 14. The cumulative number of events as a function of combined radius error of the BNS population for all detector networks. We consider events with SNR greater than 50 for all detectors except for HLA for which we choose the events with SNR above 25.

5.2.3. Post-merger NS physics. XG detectors will unveil post-merger GWs (with network SNR $>$ 5) and, via those detections, provide accurate measurements of the post-merger GW frequencies. These measurements will impact our understanding of the composition and behavior of matter at its most extreme.

To examine the potential of different network configurations to detect the post-merger signal of BNS mergers, we choose a representative signal from the CoRe database; the signal corresponds to a 1.35–1.35 $M_\odot$ merger with an SLy EoS [143]. For each network configuration in this trade study, we simulate a population of neutron star mergers and calculate the sky and orientation averaged detection range at a threshold of SNR $=$ 5. The sky-location and frequency-dependent sensitivity of long-arm detectors [144] are taken into account. For this calculation, we also use the kilohertz-focused configuration [8] of the CE20 observatory which optimizes the post-merger sensitivity. The results are shown in figures 2 and 4 of the WP.

5.3. New sources, new probes and extreme astrophysics

NSs and BHs can emit GWs through a wide variety of mechanisms other than binary mergers and post-mergers [145, 146]. Although not yet detected, these other signals (with durations from a fraction of a second to longer than a human lifetime) have great discovery potential. When detected, especially in combination with signals carried by other messengers, these GW signals will reveal different populations of compact objects and probe extreme astrophysics in a regime largely different from that probed by compact binary mergers and terrestrial colliders. Here we summarize scenarios for detection of and extraction of information from several predicted types of signals. We also note that the history of opening new windows of astronomy indicates that unexpected signals are to be expected.

5.3.1. Continuous waves. Spinning neutron stars produce *continuous GWs,* signals with low amplitude compared to binary mergers but lasting many years [147, 148]. This allows for greatly enhanced detectability with matched filtering and similar techniques. Continuous GW emission likely is dominated by either a mass quadrupole (sustained by elastic or magnetic stresses) or a mass current quadrupole (produced by an unstable or weakly stabilized *r*-mode, a rotational mode with a frequency comparable to the star's spin frequency). Free precession can also produce GWs via a changing mass quadrupole, but based on EM pulsar observations

it is likely to be rare. For a given quadrupole, GW emission is stronger for rapidly rotating NSs [149], and the *r*-mode instability to GW emission [150] is more likely to overcome various dissipation mechanisms at higher frequencies [151]. Continuous GW searches are more sensitive when using the sky location, spin frequency, and other timing information of the source (if known). Sensitivities can be expressed in terms of a *sensitivity depth* [148, 152]

$$\mathcal{D} = \sqrt{S_h}/h_0, \tag{6}$$

where S_h is the noise PSD and h_0 is the intrinsic GW strain defined by [153]. The sensitivity depth factors out the noise amplitude from everything else (methods, amount of data, etc) and is convenient for extrapolating current searches to new detectors as we do here.

Accreting NSs are of particular interest as continuous wave sources since accretion tends to spin them up and to generate asymmetries through electron capture layers and lateral temperature gradients [154, 155], magnetic bottling of accreted material [156], or the GW-driven *r*-mode instability [157]. In fact, one popular theory posits that the spins of accreting neutron stars are limited to relatively low values (compared to the maximum allowed for most equations of state) by the spin-down torque due to GW emission balancing the spin-up torque due to accretion [158]. In this case the GW strain of an accreting neutron star is expected to be proportional to the square-root of the observed x-ray flux [159], meaning that the brightest GW emitters are Sco X-1 and other low mass x-ray binaries with no observed pulsations and thus no confirmed spin frequency [160]. These sources exhibit stochastic x-ray variability, meaning that the accretion torque and spin frequency also fluctuate. Despite these obstacles, a recent GW search [161] achieved a sensitivity comparable to the strain implied by torque balance, even under pessimistic assumptions, albeit only in a narrow frequency band. Extrapolations from this sensitivity are made in [162], which we summarize here. Using the sensitivity depth of [161] (a conservative $39\,\mathrm{Hz}^{-1/2}$) with the network noise curves from table 3 and average bolometric fluxes estimated in [160, 162] finds that the HLA network can detect GWs at the torque balance limit of Sco X-1 at GW frequencies up to about 800 Hz. This corresponds to spin frequencies up to about 400 Hz for mass quadrupole emission or about 550 Hz for *r*-modes. Since accreting neutron stars are known to spin above 700 Hz in some cases, HLA is not guaranteed detection even of Sco X-1. With the 40LA configuration network, CE is sensitive enough to detect at the torque balance limit up to 1400 Hz, high enough to cover almost all known neutron stars. The 4020ET configuration is sensitive up to almost 2 kHz, well beyond the GW frequency of any known neutron star. 4020ET is also sensitive to GX 5–1 and several other neutron stars up to GW frequencies of almost 1 kHz. At this point even non-detection is very interesting since it strongly confronts the torque balance theory.

After accretion ends, the neutron star is believed to become a *millisecond pulsar* with high spin frequency and slow spin-down [163]. The latter indicates a small external magnetic dipole and small internal mass quadrupole by ruling out large torques due to EM radiation and GWs respectively, and is usually believed to be dominated by magnetic dipole radiation. However, in recent years it has become apparent that millisecond pulsar spin-downs exhibit a cutoff whose frequency dependence is quadrupolar rather than dipolar [164]. The implied minimum quadrupole is about 10^{-9} times the moment of inertia, consistent with buried magnetic fields of order 10^{11} G, consistent with the fields of young pulsars and with theoretical predictions [156, 165]. The buried magnetic field may survive for a long time under the accreted material [166]. Millisecond pulsars which are observed regularly in radio or EM waves can be timed precisely enough to allow narrow, deep GW searches. Based on previous examples, the sensitivity depth of such a search can be conservatively estimated as $500\,\mathrm{Hz}^{-1/2}$ for a year of observation [148] and scales as the square root of the observation time. Then assuming an ellipticity of 10^{-9} [164]

and taking data from the ATNF pulsar catalog [167], the GW amplitude is simple to determine and compare to the search sensitivities of various networks. In table 1 of this paper we quote numbers from [162] of millisecond pulsars detectable with various networks with one year of observation and for years of observation to detect 25 millisecond pulsars. The WP plots these numbers in its figure 2 and figure 4. These numbers only include currently known pulsars. By the time CE is operational the square kilometer array, next generation very large array, and other instruments are expected to detect several new pulsars for each one currently known [168, 169]. Thus the number of detectable pulsars should improve accordingly. Conversely, non-detection would severely constrain the theory that millisecond pulsars' original magnetic fields survive buried under accreted material.

All sky broadband continuous GW surveys for yet unknown neutron stars are another popular type of search [147, 148]. In this case, recent population simulations [170] for the ET indicate that it might detect more than 100 sources on its own in an all sky survey. With its better sensitivity, a 40 km CE will detect even more than ET. Any new continuous GW source detected by such surveys will be followed up with a year or more of observation, resulting in arcsecond sky localization (the diffraction limit for two astronomical units' aperture) even with one interferometer, and a frequency measurement to a precision of tens of nHz [171]. With such precise guidance, the source is likely to be detected by EM pulsar searches.

The combination of continuous GWs and EM observations will open new windows into neutron star interiors and for a population distinct from the progenitors of binary mergers [172]. The ratio of GW frequency to spin frequency immediately yields insight into the GW emission mechanism (mass quadrupole, free procession, or *r*-mode). In the case of a mass quadrupole it might reveal the timescale of any coupling between crust and core leading to glitches (see below), and in the case of *r*-modes it can yield a measure of the neutron star's compactness to a few percent [173] and thus on the EoS in a low-temperature regime inaccessible to colliders. In some cases GW parallax arising from a 2×1 AU baseline over a period of six months can yield a distance measurement [174], and in others, the distance can be obtained from EM astronomy. With the distance the magnitude of the quadrupole can be measured, and long-term timing may indicate whether a mass quadrupole is sustained by elastic or magnetic forces [175]. A large elastic quadrupole is only possible if the 'neutron' star has an exotic composition [176], a magnetic quadrupole measurement yields an approximation of the star's internal magnetic field, and an *r*-mode saturation amplitude is tied to viscosity and other microphysics of the stellar interior [177].

5.3.2. Core collapse supernovae. Core-collapse supernovae generate short bursts of GWs from rapid motions of high density matter in their central regions [146]. Unlike binary mergers, these motions cannot be predicted with sufficient precision for the use of matched filtering to detect the signals; but other techniques exist for detecting less modeled bursts. Simulations indicate that the most common events (with little rotation) will be detectable only in the Milky Way even with CE, with uncommon events detectable in the Magellanic Clouds and very rare events perhaps detectable further away [178]. Therefore the overall detection rate is expected to be of order one over the planned fifty-year lifetime of the CE facilities. Even one detected supernova would be a tremendous opportunity for multi-messenger astronomy, as Supernova 1987A was before GW astronomy existed. On the GW side, CE's improved sensitivity over the current generation of detectors would lead to improved waveform reconstruction [179]. This would provide a unique window into the explosion's central engine [146], revealing for example the EoS of a newly formed protoneutron star via frequency measurements of f-mode and g-mode oscillations driven by fallback accretion [180] or diagnosing the formation of a

rapidly rotating BH [181]. It would also allow measurement of the progenitor core's angular momentum distribution in cases of rapid rotation [182]. Neutrinos should be detected coincident with the GW emission and improve detection confidence and parameter estimation [146], for example revealing the spin of the core through their modulation frequency [183]. In some extreme cases (collapsars), even disk outflow instabilities or the cocoon of material carved out by a jet of escaping material could emit a stochastic burst of GWs [184, 185]. Such events could be detectable at great distances corresponding to a rate of order ten per year [185].

5.3.3. Starquakes. GWs can also be emitted in bursts from less than a second to minutes in duration by the many quasinormal modes of NSs triggered by impulsive events (starquakes) observed electromagnetically as pulsar glitches or magnetar flares (possibly accompanied by fast radio bursts) [145]. Both pulsars and magnetars are relatively young, drawn from a different population than the progenitors of most binary mergers. Quasinormal modes include the f-modes, which radiate almost all their excitation energy as GWs within of order one second. Pulsar glitches may also be followed by signals of up to weeks in duration as the crust and core slowly readjust [186]. Even aided by the sky location and EM trigger time, current GW observatories can detect such events in much of our galaxy only in the most optimistic scenarios [187, 188]. Extrapolating from recent searches [188] indicates that CE can detect short GW bursts with energy comparable to the EM energy of moderate magnetar flares or large pulsar glitches over a substantial fraction of our galaxy. The frequencies and damping times of modes contain information on the cold neutron star EoS [189]. Combined with x-ray observations, they can constrain the internal magnetic fields of NSs [190]. Detection of a long post-glitch signal would provide information on the viscous coupling between crust and core [191]. For the short bursts especially, it is important to have multiple XG observatories to improve detection confidence.

5.4. Fundamental physics and precision measurement of the Hubble constant

The improved sensitivity of the CE detectors in comparison to the current generation of GW detector networks results not only in more detections up to larger distances but also in a large number of signals with high SNRs, which are of immense importance for testing fundamental physics, general relativity and precise measurements of cosmological parameters.

5.4.1. Testing general relativity and fundamental physics. The most general approach to testing general relativity involves the introduction of deviation parameters in the amplitude and phase of the GW binary inspiral waveform and constraining these parameters using observations [192]. These deviation parameters are usually theory-agnostic but they can be mapped to specific theories if needed [193]. To a good approximation, constraints on these deviation parameters scale inversely with SNR ρ. When multiple GW observations are combined, the constraints on the deviation parameters also improve,

$$\sigma \propto \frac{1}{\rho} \longrightarrow \sum_{i=1}^{N} \frac{1}{\sigma^2} \propto \sum_{i=1}^{N} \rho^2 \tag{7}$$

where N is the number of GW events and σ is the standard deviation for a fiducial deviation parameter. The bounds on the deviation parameter will be affected by both, the number of signals detected by the network as well as the SNR with which these signals are detected. In table 1, we report the effective SNR ($\sum \rho^2$) corresponding to BBH systems for different

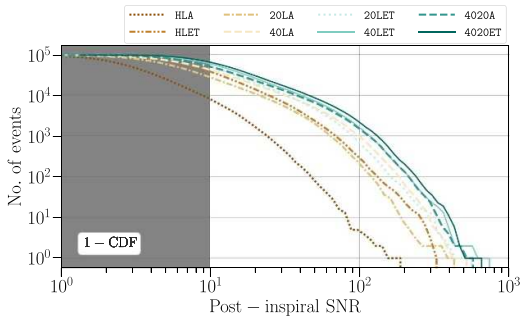

Figure 15. The scaled CDF plots for the post-inspiral SNRs corresponding to the local BBH population.

detector networks. Just going from the A$^\sharp$ network to one containing a CE detector improves the effective SNR by $\sim 4-7$ times, improving the constraints by $\sim 2-3$ times. Having at least two XG detectors in the network increases the effective SNR by two orders of magnitude compared to the A$^\sharp$ network, leading to $\sim$10 times improvement in the bounds on deviation parameters. In table 1 and figure 15, we also report the number of BBH events with *post-inspiral* SNR greater than 100 and the effective post-inspiral SNR for each network. The post-inspiral SNR is calculated by performing the SNR calculation beginning at the ISCO (innermost stable circular orbit) frequency, instead of starting at $f_{\rm low}$. Thus, it has contributions from the merger and the ringdown phases. While the network with three A$^\sharp$ detectors is only expected to detect $\mathcal{O}(10)$ events with post-inspiral SNR greater than 100, a network with CE20 will detect $\mathcal{O}(100)$ and CE40 will detect $\mathcal{O}(1000)$ such events every year. These events will allow testing general relativity in the strong-field regime close to merger and using quasinormal modes that describe the ringdown phase to test the nature of black holes [194].

These estimates can be extended to specific alternate theories of gravity (see [195] for a comprehensive study). Constraints on both the dipole radiation as well as the time variation of the gravitational constant G scale inversely with SNR. However, we should note that both these effects appear at low PN orders ($-$1PN and $-$4PN, respectively) and are better constrained using multiband observations with LISA [196], instead of only using terrestrial networks. On the other hand, Lorentz violation with non-commutative theories of gravity and parity violation with the dynamical Chern-Simon theory affect the GW phasing at 2PN, but the constraints on these theories scale with $\rho^{-1/4}$. Moreover, theories that predict a massive graviton have a leading order effect on GW phase at 1PN. While the constraint on the mass of the graviton scale as $\rho^{-1/2}$ with SNR, they also scale as $D_0^{-1/2}$, where D_0 is the cosmological distance. Thus, GWs from objects that are farther away can provide tighter bounds on the mass of graviton. In table 1, we list the number of BNS and BBH mergers that occur beyond $z \geqslant 5$ and can be detected. For the BNS case, we see that only those networks that contain a 40 km CE can detect such far-away mergers. The number of detections increase by 7 times when the network includes both CE40 and CE20 along with an A$^\sharp$ detector, compared to only containing the CE40 with two A$^\sharp$ detectors. For BBH systems, the number of detections corresponding to systems that lie beyond $z = 5$ increases by two orders of magnitude when only one of the CE detectors is included, compared to a network with only A$^\sharp$ detectors. Further, figure 6 shows that these distant events can be detected with SNR $\sim$100 with CE detectors. Thus, GW networks with CE detectors will allow testing general relativity and fundamental physics for both theory-agnostic and theory-specific tests to unprecedented precision.

5.4.2. Measuring the Hubble constant with golden dark sirens and bright sirens. Detecting GWs from compact binary mergers allows the estimation of the luminosity distance and the sky position associated with the source. As GW observations provide the distance to the source without the need for external distance calibrators, GW sources are often referred to as standard candles. Under the construct of ΛCDM cosmology,

$$\begin{aligned} D_L &= \frac{1+z}{H_0}\int_{1/(1+z)}^{1}\frac{\mathrm{d}x}{x^2\sqrt{\Omega_\Lambda+\Omega_m x^{-3}}} \\ &= \frac{1+z}{H_0}\int_{1/(1+z)}^{1}\frac{\mathrm{d}x}{x^2\sqrt{1-\Omega_m\left(1-x^{-3}\right)}}, \end{aligned} \tag{8}$$

where Ω_m is the matter density, Ω_Λ is the dark energy density, and we have used $\Omega_\Lambda = 1 - \Omega_m$. Thus, having obtained the distance to the source, if the redshift associated with the source can also be estimated, then these two quantities together can allow us to measure cosmological parameters, like the Hubble constant (H_0). The utility of GWs in measuring H_0 also becomes important in light of the Hubble tension [197, 198], which is the $4\sigma - 6\sigma$ discrepancy between the measurements of H_0 using data from the early and the late epochs of the Universe [199, 200], although systematics could explain, at least some of, the difference in the two measurements [201]. Using GWs to constrain H_0 is independent of the previously mentioned approaches and can help resolve the Hubble tension by measuring H_0 to better than 2% precision.

Various approaches have been proposed to measure the redshift, and as a result, H_0, using GW observations. The NS(s) in BNS and NSBH mergers can undergo tidal disruption before the merger and lead to the generation of EM counterparts like kilonovae and short-gamma ray bursts, among others. Detecting these EM counterparts allows us to pinpoint the location of the merger and uniquely identify the host galaxy. Photometric or spectroscopic measurements of the galaxy provide the redshift associated with the source. This is referred to as the bright siren method. The BNS merger GW170817 [107–109, 202] was the first event that was used to measure H_0 with the bright siren approach, giving $H_0 = 70^{+12}_{-8}\,\mathrm{km\,s^{-1}\,Mpc^{-1}}$ [203].

In the absence of EM counterparts, as will be the case for BBH and most NSBH mergers, the sky localization of the source can be utilized to obtain redshift measurement. The first such approach was proposed in [204], also called the statistical dark siren approach. It involves combining the H_0 estimates from all the galaxies that lie within the localization volume associated with an event, for all the eligible detections. In doing so, the true value of H_0 can be isolated from the noise and inferred. Combining eight well-localized dark siren events, [205] obtain $H_0 = 79.8^{+19.1}_{-12.8}\,\mathrm{km\,s^{-1}\,Mpc^{-1}}$. These bounds are expected to get better with more detections. The capabilities of different detector networks w.r.t. 3D localization was discussed in section 4.3. In comparison to the HLA network, the inclusion of XG detectors in the network results in drastically better localization estimates.

Among these dark siren events, there will also be a fraction of events that are so well localized in the sky that only one galaxy can lie in that sky patch [206]. This would ensure unique identification of the host galaxy and the associated redshift can be obtained. Such events are called golden dark siren events. In figure 16, we show the accuracy with which H_0 can be estimated using the golden dark siren approach and the bright siren approach for different detector networks. We follow [50, 207] to categorize those BBH and NSBH events as golden dark sirens for which $z \leqslant 0.1$ and $\Delta\Omega \leqslant 0.04\,\mathrm{deg}^2$. To calculate the fractional errors in H_0, we convert the luminosity distance errors to H_0 errors using equation (8). Following [207], the errors in the redshift measurement are neglected, but we take into account the uncertainty in

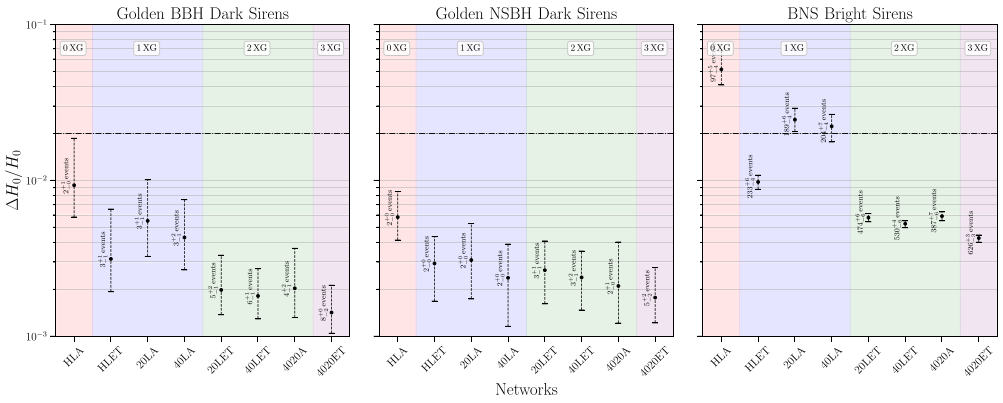

Figure 16. The accuracy in H_0 measurement using the bright siren approach with BNS mergers and the golden dark siren approach with BBH and NSBH mergers. The dotted black horizontal line in the three plots marks the 2% precision threshold for H_0 measurement, which is adequate to resolve the H_0 tension. Alongside each error bar, we also mention the number of events that were used to obtain the corresponding bound on H_0.

the value of Ω_m. Specifically, Planck gives $\Omega_m = 0.315 \pm 0.007$ [200] and the SH0ES measurement of q_0 is used to give $\Omega_m = 0.327 \pm 0.016$ [199]. This information is included in the Fisher analysis by applying a Gaussian prior on Ω_m standard deviation given by

$$\sigma_{\Omega_m} = \sqrt{\sigma^2_{\text{Planck}} + \sigma^2_{\text{SH0ES}}} = 0.017. \tag{9}$$

The Fisher matrix obtained by combining estimates from N golden dark siren events is given by

$$\Gamma_{ij} = \sum_{k=1}^{N} \frac{1}{\sigma^2_{D_L}} \left(\frac{\partial D_L}{\partial \theta_i}\right) \left(\frac{\partial D_L}{\partial \theta_j}\right)\Bigg|_k + \delta_{i2}\delta_{j2} \frac{1}{\sigma^2_{\Omega_m}}, \tag{10}$$

where $\boldsymbol{\theta} = (H_0, \Omega_m)$ and δ_{ij} refers to the Kronecker delta. From figure 2, we see that the chosen redshift distribution allows for 10 BBH and 20 NSBH mergers within $z = 0.1$ every year. To avoid making conclusions based on a specific set of events, we perform 100 realizations of the Universe and calculate the combined estimates for each of these realizations. Figure 16 shows the median error in H_0 and the error bars portray the 68% confidence interval. It is important to note that not all realizations of the Universe may contain golden dark siren detections. Hence, figure 16 only considers the realizations where at least two golden dark sirens are detected. This may lead to inflated expectations regarding the capabilities of the less sensitive 0 XG and 1 XG detector networks.

For the bright siren approach, we consider those BNS for which $z \leqslant 0.3$ and $\Delta\Omega \leqslant 10\,\text{deg}^2$. The redshift range takes into account the redshift up to which a kilonova can be observed using the Rubin or the Roman telescope and the sky-area cut-off matches the FOV of the Rubin observatory. We also assume a 20% duty-cycle due to the time-sensitive follow-up required for this method. While the same duty-cycle is used for all the detectors, networks with XG detectors will detect more events that can be followed up. Thus, we are implicitly assuming that the EM facilities will improve in the future and will be able to keep up with the GW detections. Following the same steps as for the golden dark siren case, we estimate the fractional errors

in H_0 using the bright siren approach, which is also shown in figure 16. For both the bright siren and the golden dark siren cases, we multiply the errors by a factor of $\sqrt{2}$, to account for systematic effects that have not been included in this work.

For figure 16, we see that using the golden dark siren events, the tension in H_0 could be resolved without any XG detectors, with the A$^\sharp$ network achieving sub-percent precision in the span of 1 year. With XG detectors, the bounds on H_0 improve by a factor of $2-8$, depending on the number of XG detectors in the network. In addition, we note that networks with at least 2 XG detectors are able to achieve 0.2% precision with a handful of events. This shows that for each event, individually, H_0 can be measured to the level of 1% or better (assuming Ω_m is known). This also allows for the study of possible anisotropy in H_0 measurements, which would point to the breakdown of ΛCDM cosmology.

Using the bright siren method with BNS detections, we see that the A$^\sharp$ network will be unable to measure H_0 well enough to resolve the tension. However, networks with 2 or more XG detectors will be able to measure H_0 to sub-percent precision. Also, note that the best detector network, 4020ET, achieves a precision of 0.004 with $\sim$630 events, i.e. with $\sim$2 detection per day. We expect that the future EM facilities will be capable of following up on these events at the stated frequency.

It is important to note that the actual constraints on H_0 will be even better if the bounds from BBH, NSBH and BNS events are combined. However, the fact that H_0 can be measured precisely by each of these compact binary mergers will be important as it would allow us to check the consistency of the inferred value of H_0 from the different types of mergers, and, consequently, different approaches. Inconsistency will help isolate, and correct for, any systematic effects that might have been ignored when inferring the value of H_0, or point to new physics.

5.4.3. Measuring the ΛCDM with NS tides. BNS have an intrinsic mass scale and can only exist in a narrow range of masses. This mass scale is imprinted in the tidal interaction between the component NSs. Therefore, if the nuclear EoS is known, one can determine the source-frame masses by a measurement of the tidal deformability. This, in turn, would allow the measurement of the redshift directly from a GW observation because it is the redshifted mass that is inferred from the point-particle approximation of the waveform. Such a method was first proposed in [208] and further explored in [209, 210]. The measurement of H_0 using a known relationship between the tidal parameter and source-frame mass was explored in [211–213] while [214] showed that one can simultaneously estimate both the nuclear EoS and H_0 using future observatories. A measurement of the dark energy EoS was explored in [215, 216].

In this section, we explore the potential of different XG configurations to constrain the expansion history of the Universe assuming that the nuclear EoS is known. It is found in [212] that up to a 15% uncertainty in the knowledge of the EoS does not affect the measurement of the Hubble constant in a meaningful manner. We use the TaylorF2 waveform model augmented with the 5PN and 6PN tidal terms in the phase, terminating the signal at the ISCO frequency corresponding to the total mass of the binary. Additionally, we assume the APR4 EoS for the NS. We fit the logarithm (base 10) of the tidal deformability as a function of the mass of the NS using a fifth-order polynomial given by

$$\log_{10}\Lambda(m) = -5.60m^5 + 43.2m^4 - 132m^3 + 199m^2 - 151m + 49.2, \qquad (11)$$

where m is in units of $\mathrm{M}_\odot$. We verify that the fit reproduces the slope of the curve accurately with maximum errors at a few percent around the double Gaussian from which the neutron

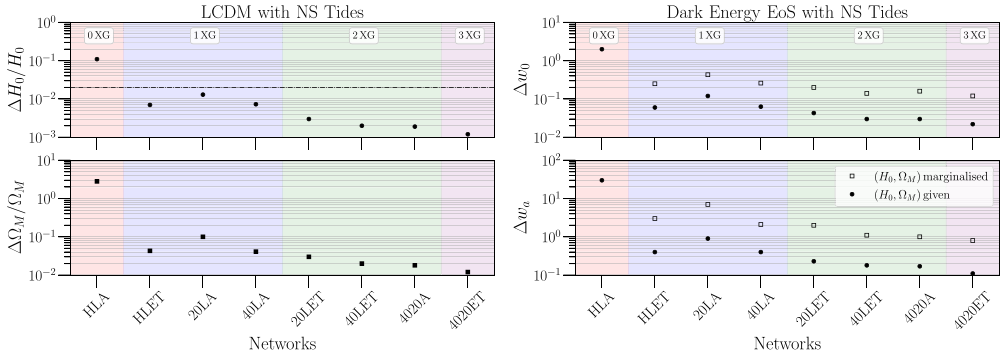

Figure 17. *Left:* the fractional uncertainty in the Hubble constant H_0 and the dark matter energy density parameter Ω_M with BNS mergers for the various network configurations under consideration. *Right:* the uncertainty in the dark energy EoS parameters w_0 and w_a for the various network configurations under consideration. We plot the constraints obtained keeping H_0 and Ω_M as model parameters but marginalizing over them (empty squares) and assuming that they are known precisely from other experiments (black circles).

star masses are drawn. This is crucial because it is the slope of the curve that contributes to the Fisher errors on the redshift.

The Fisher errors from the d_L–z space are then propagated to the space of cosmological parameters, $\vec{\phi}$, via another Fisher matrix given by [217]

$$\mathcal{G}_{ij} = \sum_{k=1}^{N} \frac{1}{\sigma^2_{d_L,k}} \frac{\partial d^k_L(z)}{\partial \phi^i} \frac{\partial d^k_L(z)}{\partial \phi^j}, \tag{12}$$

where N is the total number of observations in the catalog and $\sigma^2_{d_L,k}$ is the total variance in the luminosity distance for the kth event given by

$$(\sigma_{d_L})^2 = \left(\sigma^h_{d_L}\right)^2 + \left(\sigma^z_{d_L}\right)^2. \tag{13}$$

Here, $\sigma^h_{d_L}$ is the contribution to the luminosity distance error due to the error in the GW amplitude while $\sigma^z_{d_L}$ is that due to the error in the redshift measurement, given by

$$\sigma^z_{D_L} = \left|\frac{\partial D_L}{\partial z}\right| \sigma_z. \tag{14}$$

In writing equation (12), we have neglected the correlations in the d_L–z space for simplicity.

The results for H_0 and Ω_M are shown in the left panel of figure 17. It is observed that H_0 and dark matter energy density cannot be simultaneously constrained in the absence of any XG detectors. With at least 1 XG detector, H_0 can be determined at the percent level while Ω_M can be measured to an accuracy of $5\% - 10\%$. Of particular note is that an XG network consisting of CE20 is significantly worse than its 40 km counterpart and the ET observatory. With a network of 2 XG detectors, the errors decrease by a factor of $2-4$ while a full XG network consisting of 3 XG detectors further reduces the errors by another 50%.

Table 12. Relative rate of strong lensing detections per year for seven detector networks and variable binary compact object population models. The strong lenses are generated using galaxies drawn from the SDSS galaxy catalog [see reference 218].

Detector configuration	Local population	Population III	Primordial black holes	Binary neutron stars
HLET	6.9×10^{-3}	2.3×10^{-3}	2.0×10^{-3}	2.7×10^{-4}
20LA	6.6×10^{-4}	2.2×10^{-3}	2.1×10^{-3}	1.5×10^{-4}
40LA	7.3×10^{-4}	2.4×10^{-3}	2.1×10^{-3}	2.4×10^{-4}
40LET	7.9×10^{-4}	2.5×10^{-3}	2.2×10^{-3}	2.4×10^{-4}
20LET	7.3×10^{-4}	2.3×10^{-3}	2.2×10^{-3}	2.5×10^{-4}
4020A	7.6×10^{-4}	2.5×10^{-3}	2.2×10^{-3}	2.4×10^{-4}
4020ET	8.1×10^{-4}	2.5×10^{-3}	2.3×10^{-3}	2.3×10^{-4}

5.4.4. Measuring the dark energy with NS tides. In various dark energy models, Ω_Λ is not a constant but evolves with the redshift. The dependence commonly takes the form

$$\Omega_\Lambda(z) = \Omega_{\Lambda,0} \exp 3 \int_0^z \frac{\mathrm{d}z'}{1+z'} [1 + w_\Lambda(z')], \tag{15}$$

for different dark energy models where $w_\Lambda(z)$ is the dark energy EoS parameterized in terms of w_0 and w_a as

$$w_\Lambda(z) = w_0 + w_a \frac{z}{1+z}. \tag{16}$$

The results for the dark energy EoS parameters are shown in the right panel of figure 17. In the absence of any XG detectors, dark energy EoS parameters cannot be measured. We see similar factors of improvement with the addition of each XG detector. Notably, if the ΛCDM parameters are marginalized over instead of assumed to be given from other experiments, the constraints on the dark energy EoS parameters worsen by a factor of $5-10$.

5.4.5. GW lensing. Gravitational lensing, a captivating phenomenon predicted by Einstein's theory of general relativity, bends light and gravitational radiation as they pass near massive intervening objects. The advent of XG observatories usher in a new era of gravitational lensing exploration, as it is projected that approximately one in a thousand BBHs and one in a few thousand BNSs will be strongly lensed, resulting in an annual detection rate of around $\mathcal{O}(50-100)$ lensed events (see table 12). Such lensed detections have the potential to achieve highly precise localization of BBHs with sub-arcsecond accuracy, identify new subpopulations of lensed systems, probe the fundamental properties of GWs, reconstruct gravitational lenses using GW signals, perform cosmographic measurements at submillisecond timing precision, develop comprehensive models of lens populations, and conduct multifaceted studies involving multiple messenger signals—see [219, 220] and references therein. Embracing this research frontier with XG observatories not only advances GW astronomy but can also pave the way for groundbreaking discoveries that enhance our knowledge of gravity, astrophysics, and the intricacies of the Universe.

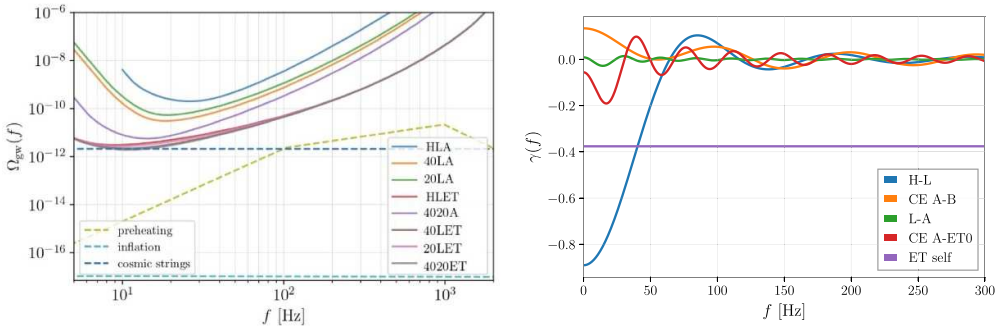

Figure 18. *Left:* power-law integrated (PI) curves showing the sensitivity of the various detector networks considered in this work to the stochastic gravitational-wave background. Any background whose spectrum crosses the PI curve would be detected with SNR = 3 after one year of observing time. Dashed lines show the expected backgrounds for cosmic strings ($G\mu = 10^{-11}$ with fiducial model parameters from [221]), preheating (for hybrid inflation occurring at 10^9 GeV as calculated in [222]), and standard slow-roll inflation. *Right:* overlap reduction functions for various detector pairs considered here, normalized so that $\gamma(f) = 1$ for co-located and co-aligned L-shaped detectors.

5.5. Physics beyond the standard model

5.5.1. Stochastic backgrounds. The sensitivity of a given XG network to the stochastic GW background of primordial origin quantifies its ability to probe early-Universe physics. Typical stochastic background searches assume that the background is Gaussian, isotropic, stationary, and unpolarized, so the optimal search strategy is to look for excess correlated power between pairs of detectors [223, 224]. In this case, the sensitivity of the pair depends primarily on the detector PSDs and geometry, quantified via the overlap reduction function, $\gamma(f)$ [225]. Co-located and co-aligned L-shaped detectors have $\gamma(f) = 1$, while for detectors separated by large distances and large relative angles, $\gamma(f)$ is an oscillatory function that asymptotes to zero at large frequencies, penalizing the sensitivity of that detector baseline. The overlap reduction functions for several detector baselines considered in this document are shown in the right panel of figure 18.

The strength of the stochastic background is typically parameterized in terms of

$$\Omega_{\rm GW}(f) \equiv \frac{1}{\rho_c}\frac{{\rm d}\rho_{\rm GW}}{{\rm d}\ln f} = \Omega_\alpha \left(\frac{f}{f_{\rm ref}}\right)^\alpha, \tag{17}$$

where $\rho_{\rm GW}$ is the energy density in GWs and ρ_c is the critical energy density needed to close the Universe. For a given value of the power-law index α, the background amplitude that would be detectable with SNR ρ and an observing time T is given by

$$\Omega_\alpha = \frac{\rho}{\sqrt{2T}}\left[\int_{f_{\rm min}}^{f_{\rm max}} {\rm d}f \frac{(f/f_{\rm ref})^{2\alpha}}{\Omega_{\rm eff}^2(f)}\right]^{-1/2} \tag{18}$$

$$\Omega_{\rm eff} = \frac{10\pi^2}{3H_0^2} f^3 S_{\rm eff}(f)\,. \tag{19}$$

The effective strain noise power spectral density is given by

$$S_{\rm eff} = \left[\sum_{I=1}^{M}\sum_{J>I}^{M} \frac{\gamma_{IJ}^2(f)\sin^2\beta_I \sin^2\beta_J}{P_{n,I}(f)\,P_{m,J}(f)}\right]^{-1/2}, \tag{20}$$

where the indices I, J indicate the interferometer, β is the opening angle between the arms of each interferometer, and P_n is the noise PSD.

The last row of table 1 gives the background amplitude that would be detectable with SNR = 3 after one year of observing for each of the eight networks considered in this document at a reference frequency of 25 Hz for $\alpha = 0$, which is the theoretical expectation for backgrounds produced by vanilla inflation [226]. The left panel of figure 18 shows the power-law integrated (PI) curves [227] for each network, for which a stochastic background that crosses or lies tangent to the PI curve would be detected with SNR = 3 after 1 yr of observing.

Because ET consists of three nearly co-located detectors and has the best projected sensitivity at low frequencies, the networks including ET are not penalized as strongly by the geometric $\gamma(f)$ factor and thus have the best projected sensitivity to the stochastic background. We neglect the effect of correlated noise, which may be significant for the co-located ET detectors [228, e.g.]. The exact sensitivity of the proposed XG networks will change due to the change in the overlap reduction function once the locations and orientations of the detectors are finalized, but the numbers quoted here are meant to be representative of XG detector capabilities.

It is worth noting that these values of $\Omega_{\rm GW}$ are calculated assuming that the primordial background can be perfectly separated from the foreground of merging compact binaries. New methods that exploit the statistical differences between the two signals are being developed to ensure this is possible by the time that XG data become available [229–233].

5.5.2. Bosonic asymmetric dark matter. The next generation of GW detectors are expected to observe $\sim 10^6$ BNS mergers per year with precise measurements of their effective tidal deformability. If neutron stars accumulate ambient dark matter, their EoS would deviate from that of pure neutron stars, in turn leading to a deviation in the effective tidal deformability of the binary system. The accumulation of dark matter particles in NS cores due to accretion over long timescales could potentially lead to the formation of a mini BH, destabilizing the NS and resulting in its implosion to form a BH without significantly increasing its mass. When this process occurs in neutron stars in coalescing binaries, one or both stars might be converted to a BH before they merge. Hence, the total rate of mergers of compact objects in the mass range $1-2\,M_\odot$ would have relative contributions majorly from BNS, BBH and significantly lower from NSBH systems. The precise measurement of the effective tidal deformability parameter with the XG detectors, we would be able to distinguish between the sub-populations of compact mergers since the tidal deformability of BHs is zero, while NSs have non-zero values for the tidal deformability. This distinguishability using matter properties is essential in ascertaining the relative rates of BNS and BBH mergers. However, the rates are also informed by the collapse time of the NS to BH which in turn depends on the mass and scattering cross-section of the dark matter particles. Therefore, GW observations of BBHs and BNSs can potentially constrain particle properties of dark matter through the observed rates of different binary populations in the mass range of $1-2\,M_\odot$.

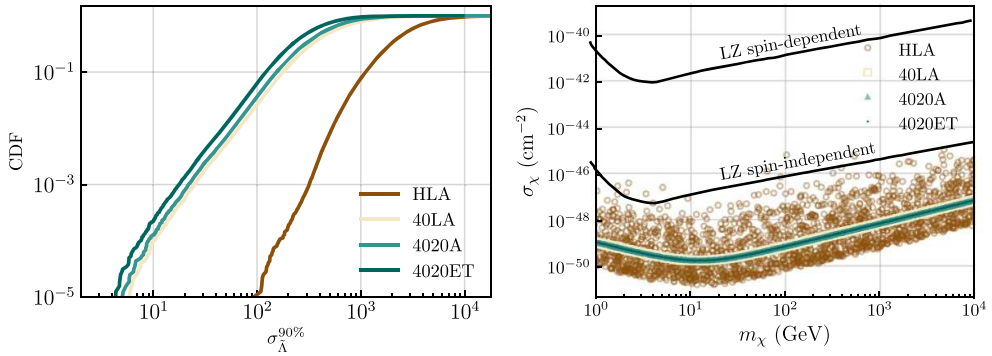

Figure 19. *Left:* cumulative distribution function (CDF) of the error in the measurement of effective tidal deformability in four representative detector networks with and without cosmic explorer. *Right:* comparison between the constraints obtained for $m_\chi \in [1, 10^4]$ GeV assuming an ambient DM density of $\rho_\chi = 1$ Gev cm^{-3} for representative detector networks with the latest constraints from the direct detection experiment, LZ [234].

In the left panel of figure 19, we show the capability of a subset of detector networks considered in the study to measure the effective tidal deformability of merging binaries. The addition of a single CE to the network drastically reduces the measured error - 0.001% of events are detected with an error $\sigma_{\tilde{\Lambda}}^{90\%} \sim eq 100$ in the HLA network, while the same fraction of events are detected with $\sigma_{\tilde{\Lambda}}^{90\%} < 10$ in networks with at least one CE. The right panel in the same figure shows the effect of measured errors on the effective tidal deformability on the inferred dark matter constraints. For an assumed threshold of $\sigma_{\tilde{\Lambda}}^{90\%} = 50$, we derive the upper limits for the dark matter particle mass and scattering cross-section with baryons. We also present the upper limits for WIMPs reported by Lux–Zeplin experiment (LZ [234–236]) to show how competitive these constraints can be with leading dark matter experiments.

5.5.3. Ultra-light boson clouds around rotating black holes. Axions are ultralight bosons hypothesized to solve the strong-CP problem in QCD. If axions or other ultra-light scalar or vector ultralight bosons exist, they could appear spontaneously near rotating black holes and be bound to them if their Compton wavelength is comparable to the BH size [237–239]. They could extract mass and energy from BHs over time, building up a macroscopic dark-matter 'cloud' via a superradiance process [239, 240] which might be easier to detect with vector (i.e. spin 1) bosons with near-term detectors [241–243]. The so-called 'gravitational atom' could then emit quasi-monochromatic, persistent, GWs via boson-boson annihilation [244]. Current detectors are able to detect the presence of boson cloud systems at the galactic center in the most recent observing run, for young spinning black holes (less than 10^5 years) [245], but with the advent of XG observatories, those prospects will improve by a factor of 10-20. In figure 20, we plot the distance reach, computed according to an analytic expression, equation (57) given in [246], as a function of ultralight boson mass, in the small gravitational fine-structure constant α limit ($\alpha < 0.1$), assuming a uniform distribution of spins between

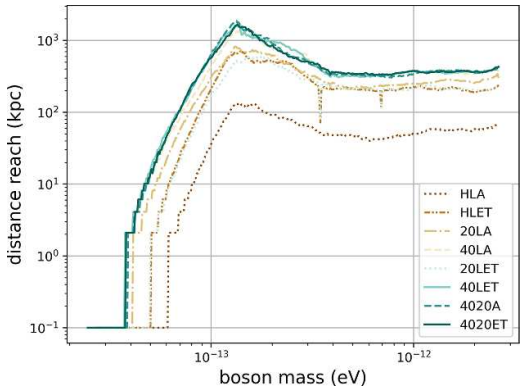

Figure 20. Astrophysical distance reach as a function of axion mass for ultralight boson clouds that could form around rotating black holes. Different colors correspond to different detectors.

[0.2, 0.9], a log-uniform distribution of ages between $[10^3, 10^7]$ years, a coherence length of 10 days, and a Kroupa distribution [247] for black hole masses between [5, 100]$M_\odot$. This distance corresponds to detecting at least 5% of black holes located at that distance away with a particular boson cloud. The improvements relative to the current detector era are immense, and are derived for a *semi-coherent* all-sky search for boson cloud systems with fast-Fourier-transform length of $T_{\rm FFT} = 10$ days and a threshold on our detection statistic, the critical ratio, of 3.4, as done in a similar analysis for ET design comparisons [27].

6. Conclusions

In this paper, we compared the relative performance of eight different GW observatory networks composed of A$^\sharp$ LIGO, Virgo, KAGRA, LIGO-India, CE and ET. The spirit of this study was to understand which key science goals enumerated in the CE White paper [13] can be accomplished with networks that have no XG observatories and how adding one, two or three such observatories would strengthen the network. In particular, we have explored the role of upgraded LIGO-Livingston and LIGO-India operating at A$^\sharp$ sensitivity in tandem with one or two next CE observatories and/or ET. As summarized in table 1 there is great value in operating an A$^\sharp$ LIGO when only one or two XG observatories are operating. Such a scenario could arise either because of scheduling or one or more of the XG observatories are in the commissioning or upgrade mode. A network composed of two CE observatories (one with 40 km arms and one with 20 km arms) and ET will deliver all the science goals identified in the White paper [13]; such a network will be two orders-of-magnitude better with respect to almost every science metric considered in this study and will have an unprecedented discovery potential, observing BH binaries from epochs when the first stars were still being assembled and BNSs from redshifts when the star formation was at its peak.

Data availability statement

The data that support the findings of this study are openly available at the following URL/DOI: https://doi.org/10.5281/zenodo.8087733.

Acknowledgment

We thank the members of the Cosmic Explorer Project and the Scientific Advisory Committee for their input and feedback. We thank Kara Merfeld for pointing out the omission of the assumption for binary neutron stars that leads to more mass-symmetric binaries. I G, A D, B S S, R K, and D S were supported by NSF Grant Numbers AST-2006384, AST-2307147, PHY-2012083, PHY-2207638, PHY-2308886, and PHYS-2309064 to B.S.S. S B acknowledges support from the Deutsche Forschungsgemeinschaft, DFG, Project MEMI number BE 6301/2-1. K G A acknowledges support from the Department of Science and Technology and Science and Engineering Research Board (SERB) of India via the following grants: Swarnajayanti Fellowship Grant DST/SJF/PSA-01/2017-18 and Core Research Grant CRG/2021/004565 K G A, E B and B S S acknowledge the support of the Indo-US Science and Technology Forum through the Indo-US Centre for Gravitational-Physics and Astronomy, grant IUSSTF/JC-142/2019. A B and K K acknowledge support from NSF award PHY-2207264. E B is supported by NSF Grants No. AST-2006538, PHY-2207502, PHY-090003 and PHY-20043, and by NASA Grant Nos. 20-LPS20-0011 and 21-ATP21-0010. E B acknowledges support from the ITA-USA Science and Technology Cooperation program (CUP: D13C23000290001), supported by the Ministry of Foreign Affairs of Italy (MAECI). M B acknowledges support from DOE under Award Number DE- SC0022348 G L acknowledges NSF award PHY-2208014, Nicholas and Lee Begovich, and the Dan Black Family Trust. A Corsi acknowledges support from NSF grant PHYS-2011608. AHN acknowledges support from NSF grant PHY-2309240. OAH and HP acknowledge support by grants from the Research Grants Council of Hong Kong (Project Nos. CUHK 2130822 and 4443086), and the Direct Grant for Research from the Research Committee of The Chinese University of Hong Kong. T G F L acknowledge support by grants from the Research Foundation—Flanders (G086722N, I002123N) and KU Leuven (STG/21/061). D E M, B J J S, and L S acknowledge the support of the Australian Research Council Centre of Excellence for Gravitational Wave Discovery (OzGrav), Project No. CE170100004. C P acknowledges research support from the Italian Istituto Nazionale di Fisica Nucleare (INFN). B J O, A P, and B R acknowledge support from NSF grants PHY-1912625, PHY-2309305, and AST-1907975. JDR acknowledges support from NSF grant PHY-2207270. J R S and G L acknowledge support from NSF Grant 2308985, Nicholas and Lee Begovich, and the Dan Black Family Trust. S V acknowledges support from NSF award PHY-2207387.

Table 13. We list the eight other network configurations, this time with detectors at A+ sensitivities as well.

Number of XG Observatories	Network Name	Detectors in the network
1 XG	20 $L^{\dagger}H^{\dagger}$	CE-C 20 km, LLO (A+), LHO (A+)
	20 $L^{\dagger}A^{\dagger}$	CE-A 20 km, LLO (A+), LAO (A+)
	40 $L^{\dagger}H^{\dagger}$	CE-C 40 km, LLO (A+), LHO (A+)
	20LH	CE-C 20 km, LLO, LHO
	40LH	CE-A 40 km, LLO, LHO
2 XG	4020 $L^{\dagger}$	CE-C 40 km, CE-A 20 km, LLO (A+)
	4020 L	CE-C 40 km, CE-A 20 km, LLO
	4040 L	CE-C 40 km, CE-A 40 km, LLO

Appendix A. Science metrics for other network configurations

Other than the networks discussed in section 2, we also examine the capabilities of eight other detector networks listed in table 13. These networks contain detectors at A+ sensitivities as well. They were chosen to fulfill two objectives- first, to show the capabilities of A+ detectors with CE observatories, and second, to assess the potential of a three-detector network contained in the US. For the latter, as CE-A and CE-B are very close to LHO and LLO, respectively, we introduce a new *fiducial* location for CE, called CE-C, located in Lake Michigan, at the latitude of $45^{\circ}10'3.67''$, the longitude of $-87^{\circ}03'46.2''$, with the $x-$arm oriented 250.824° counter-clockwise relative to the local east. Additionally, as the networks are taken to be located in the US (except 20 $L^{\dagger}A^{\dagger}$), we do not consider Virgo and KAGRA detectors in our networks. However, it is important to note that a five-detector network including Virgo and KAGRA at A+ sensitivities will be extremely proficient in precise localization of binary mergers, playing a crucial role in fulfilling multimessenger objectives in the late 2020 s [49, 248]. The science capabilities of the eight new networks are listed in table 14.

Table 14. Similar to table 1, but with networks at A+ sensitivities as well. The eight networks used here are described in table 13.

	Network Performance							
	1 XG					2 XG		
Science Goal Requirements	20 $L^{\dagger}H^{\dagger}$	20 $L^{\dagger}A^{\dagger}$	40 $L^{\dagger}H^{\dagger}$	20LH	40LH	4020 $L^{\dagger}$	4020 L	4040 L
BHs and NSs throughout cosmic time								
Measure mass function, determine formation scenarios:								
$N_{\rm BNS}$/yr, $z \geqslant 1$, $\delta z/z \leqslant 0.2$, $\delta m_1/m_1 \leqslant 0.3$	0	0	0	0	0	1	3	10
Detect the (injected) second Gaussian feature:								
$N_{\rm BNS}$/yr, $m_1 \geqslant 1.5\,{\rm M}_{\odot}$, $\delta m_1/m_1 \leqslant 0.1$	5	4	15	6	21	41	52	72
Unveiling the elusive population of IMBH:								
$N_{\rm IMBBH}$/yr, $z \geqslant 3$, $\delta z/z \leqslant 0.2$, $\delta m_1/m_1 \leqslant 0.2$	48	100	88	130	180	500	530	580
High-z BBH formation channels and mass function:								
$N_{\rm BBH}$/yr $z \geqslant 10$, $\delta z/z \leqslant 0.2$ $\delta m_1/m_1 \leqslant 0.2$	3	0	24	5	30	79	85	129
MMA and dynamics of dense matter								
GW170817-like golden sample:								
$N_{\rm BNS}$/yr $z \leqslant 0.06$, $\Delta\Omega \leqslant 0.1\,{\rm deg}^2$	0	0	0	0	0	0	0	0
r-process and kilonova-triggered follow up:								
$N_{\rm BNS}$, $z \leqslant 0.1$, $\Delta\Omega \leqslant 1\,{\rm deg}^2$	0	0	0	0	0	0	1	4
Jet afterglows, large-FOVs or small-FOV mosaicking:								
$N_{\rm BNS}$/yr, $0.1 < z \leqslant 2$, $\Delta\Omega \leqslant 10\,{\rm deg}^2$	0	85	1	7	8	95	210	430
Mapping GRBs to progenitors up to star-formation peak:								
$N_{\rm BNS}$/yr, $z > 2$, $\Delta\Omega \leqslant 100\,{\rm deg}^2$	0	0	0	0	0	0	0	2
Pre-merger alerts 10 min before merger								
$N_{\rm BNS}$/yr, $\Delta\Omega \leqslant 100\,{\rm deg}^2$	0	0	0	0	0	7	10	30
NS EoS constraints:								
$N_{\rm BNS}$/yr, SNR$\geqslant 100$	28	37	230	31	230	340	350	640
$N_{\rm BNS}$/yr, $\Delta R < 0.1$ km	4	0	36	20	64	140	180	270

(Continued.)

Table 14. (Continued.)

New probes of extreme astrophysics								
Pulsars with ellipticity 10^{-9} detectable in 1 year	3	3	5	3	5	9	9	20
Fundamental physics and precision cosmology								
Constrain graviton mass:								
$N_{\rm BNS}$/yr, $z \geqslant 5$	0	0	160	0	180	640	640	2600
$N_{\rm BBH}$/yr, $z \geqslant 5$	2173	2169	3925	2232	3951	4431	4446	4962
Probing rare events:								
$N_{\rm BBH}$/yr, SNR > 100	1200	1200	4800	1300	4900	6800	6800	10 500
$N_{\rm BBH}$/yr, SNR > 1000	1	1	1	1	1	5	5	9
Precision tests of GR (IMR and QNM):								
BBH root sum square total SNR	9700	9800	16 500	9900	17 000	19 000	19 000	23 000
BBH root sum square post-inspiral SNR	5200	5300	8200	5400	8300	9700	9700	12 000
$N_{\rm BBH}$/yr, post-inspiral SNR > 100	243	251	1111	281	1158	1685	1706	2663
Cosmology and tests of GR:								
$N_{\rm BNS}$/yr, $z \leqslant 0.5$, $\delta d_L/d_L \leqslant 0.1$ and $\Delta\Omega \leqslant 10\,{\rm deg}^2$	0	4	0	5	7	18	60	95
$N_{\rm BBH}$/yr, $\delta d_L/d_L \leqslant 0.1$, $\Delta\Omega \leqslant 1\,{\rm deg}^2$	1	43	2	13	19	120	180	350
Lensed BNS events/yr:	62	61	160	64	170	210	210	290
Physics beyond the standard model								
Stochastic signal $\Omega_{\rm GWBG}$ in units of 10^{-10}	0.6	1.1	0.35	0.3	0.18	0.01	0.01	0.005
Primordial black hole mergers: $N_{\rm pBBH}$/yr, $z > 25$, $\Delta z/z < 0.2$:	0	0	0	0	0	3	3	9
Pop III black hole mergers $z > 10$, $\Delta z/z < 0.1$: $N_{\rm PopIII}$/yr:	0	0	0	0	1	32	39	98
Max distance (Mpc) to detectable axion clouds in BHs	0.9	0.9	1.4	1.0	1.6	1.6	1.8	1.5

Appendix B. Data release

As mentioned in section 3, we simulate one-year populations for BBH, BNS, NSBH, IMBBH, primordial BH and Pop-III BBH systems. We make the populations available on Zenodo [249], along with an iPython notebook, called `intructions.ipynb`, that demonstrates how one can use the available data. The data files contain the intrinsic and extrinsic parameters that describe the systems, as well as the SNR and the measurement errors on some of these parameters.

ORCID iDs

Ish Gupta https://orcid.org/0000-0001-6932-8715
Ananya Bandopadhyay https://orcid.org/0000-0002-5116-844X
Matthew Evans https://orcid.org/0000-0001-8459-4499
Evan D Hall https://orcid.org/0000-0001-9018-666X
Rahul Kashyap https://orcid.org/0000-0002-5700-282X
Andrew L Miller https://orcid.org/0000-0002-4890-7627
Cristiano Palomba https://orcid.org/0000-0002-4450-9883
Binod Rajbhandari https://orcid.org/0000-0001-7568-1611
Jocelyn Read https://orcid.org/0000-0002-3923-1055
Joseph D Romano https://orcid.org/0000-0003-4915-3246
Salvatore Vitale https://orcid.org/0000-0003-2700-0767
Lisa Barsotti https://orcid.org/0000-0001-9819-2562
Emanuele Berti https://orcid.org/0000-0003-0751-5130
Hsin-Yu Chen https://orcid.org/0000-0001-5403-3762
Peter Fritschel https://orcid.org/0000-0003-1983-3187
Geoffrey Lovelace https://orcid.org/0000-0002-7084-1070
Bram J J Slagmolen https://orcid.org/0000-0002-2471-3828
Joshua R Smith https://orcid.org/0000-0003-0638-9670

References

[1] Aasi J *et al* (LIGO Scientific) 2015 Advanced LIGO *Class. Quantum Grav.* **32** 074001
[2] Acernese F *et al* (VIRGO) 2015 Advanced Virgo: a second-generation interferometric gravitational wave detector *Class. Quantum Grav.* **32** 024001
[3] Abbott R *et al* (LIGO Scientific, VIRGO and KAGRA) 2021 GWTC-3: compact binary coalescences observed by LIGO and Virgo during the second part of the third observing run (arXiv:2111.03606 [gr-qc])
[4] Abbott B P *et al* (KAGRA, LIGO Scientific, Virgo and VIRGO) 2018 Prospects for observing and localizing gravitational-wave transients with Advanced LIGO, Advanced Virgo and KAGRA *Living Rev. Relativ.* **21** 3
[5] Akutsu T *et al* (KAGRA) 2021 Overview of KAGRA: calibration, detector characterization, physical environmental monitors and the geophysics interferometer *PTEP* **2021** 05A102
[6] Iyer B, Souradeep T, Unnikrishnan C, Dhurandhar S, Raja S and Sengupta A 2011 LIGO-India, proposal of the consortium for Indian Initiative in Gravitational-wave Observations (IndIGO) *Technical Report* M1100296-v2 (LIGO-India) (available at: https://dcc.ligo.org/LIGO-M1100296/public)
[7] Fritschel P, *et al* 2022 Report from the LSC Post-O5 study group *Technical Report* T2200287 (LIGO) (available at: https://dcc.ligo.org/LIGO-T2200287/public)
[8] Evans M *et al* 2021 A horizon study for cosmic explorer: science, observatories, and community (arXiv:2109.09882 [astro-ph.IM])
[9] Punturo M *et al* 2010 The Einstein telescope: a third-generation gravitational wave observatory *Class. Quantum Grav.* **27** 194002

[10] Hild S *et al* 2011 Sensitivity studies for third-generation gravitational wave observatories *Class. Quantum Grav.* **28** 094013
[11] E S Team 2011 Einstein gravitational wave telescope conceptual design study (available at: https://doi.org/10.5281/zenodo.3911261) (eT-0106C-10)
[12] ET Steering Committee 2020 ET design report update 2020 *Technical Report* ET-0007A-20 (Einstein Telescope) (available at: https://apps.et-gw.eu/tds/?content=3&r=17245)
[13] Evans M *et al* 2023 Cosmic explorer: a submission to the NSF MPSAC ngGW subcommittee (arXiv:2306.13745 [astro-ph.IM])
[14] Prakash A, Gupta I, Breschi M, Kashyap R, Radice D, Bernuzzi S, Logoteta D and Sathyaprakash B S 2023 Detectability of QCD phase transitions in binary neutron star mergers: Bayesian inference with the next generation gravitational wave detectors (arXiv:2310.06025 [gr-qc])
[15] Hall E D and Evans M 2019 Metrics for next-generation gravitational-wave detectors *Class. Quantum Grav.* **36** 225002
[16] Ashton G *et al* 2019 BILBY: a user-friendly Bayesian inference library for gravitational-wave astronomy *Astrophys. J. Suppl.* **241** 27
[17] Ashton G and Talbot C 2021 Bilby-MCMC: an MCMC sampler for gravitational-wave inference *Mon. Not. R. Astron. Soc.* **507** 2037
[18] Romero-Shaw I M *et al* 2020 Bayesian inference for compact binary coalescences with bilby: validation and application to the first LIGO–Virgo gravitational-wave transient catalogue *Mon. Not. R. Astron. Soc.* **499** 3295
[19] Kandhasamy S and Bose S 2023 LIGO-India observatory coordinate system for GW analyses *Technical Report* T2000158 (LIGO) (available at: https://dcc.ligo.org/LIGO-T2000158-v1/public)
[20] Althouse W, Jones L and Lazzarini A 2009 Determination of global and local coordinate axes for the LIGO sites *Technical Report* T980044 (LIGO) (available at: https://dcc.ligo.org/LIGO-T980044/public)
[21] LIGO Scientific Collaboration L1 calibrated sensitivity spectra (available at: https://dcc.ligo.org/LIGO-G2100675/public) (Accessed 27 March 2024)
[22] Barsotti L*et al* The A+ design curve (available at: https://dcc.ligo.org/LIGO-T1800042/public) (Accessed 27 March 2024)
[23] Kuns K*et al* The A♯ design curve (available at: https://dcc.ligo.org/LIGO-T2300041/public) (Accessed 27 March 2024)
[24] Einstein Telescope Design Team ET-D Design Curve (available at: https://tds.virgo-gw.eu/?content=3&r=14065) (Accessed 27 March 2024)
[25] Kuns K *et al* (Cosmic Explorer) Cosmic explorer strain sensitivity (available at: https://dcc.cosmicexplorer.org/CE-T2000017/public) (Accessed 27 March 2024)
[26] Adhikari R X *et al* 2019 Astrophysical science metrics for next-generation gravitational-wave detectors *Class. Quantum Grav.* **36** 245010
[27] Branchesi M *et al* 2023 Science with the Einstein telescope: a comparison of different designs (arXiv:2303.15923 [gr-qc])
[28] Abbott R *et al* (KAGRA, VIRGO and LIGO Scientific) 2023 Population of merging compact binaries inferred using gravitational waves through GWTC-3 *Phys. Rev.* X **13** 011048
[29] Vecchio A 2004 LISA observations of rapidly spinning massive black hole binary systems *Phys. Rev.* D **70** 042001
[30] Wysocki D, Lange J and O'Shaughnessy R 2019 Reconstructing phenomenological distributions of compact binaries via gravitational wave observations *Phys. Rev.* D **100** 043012
[31] Madau P and Dickinson M 2014 Cosmic star formation history *Ann. Rev. Astron. Astrophys.* **52** 415
[32] Talbot C, Smith R, Thrane E and Poole G B 2019 Parallelized inference for gravitational-wave astronomy *Phys. Rev.* D **100** 043030
[33] Abbott R *et al* (LIGO Scientific and Virgo) 2021 Population properties of compact objects from the second LIGO-Virgo gravitational-wave transient catalog *Astrophys. J. Lett.* **913** L7
[34] Ng K K Y, Vitale S, Farr W M and Rodriguez C L 2021 Probing multiple populations of compact binaries with third-generation gravitational-wave detectors *Astrophys. J. Lett.* **913** L5
[35] Ng K K Y, Franciolini G, Berti E, Pani P, Riotto A and Vitale S 2022 Constraining High-redshift stellar-mass primordial black holes with next-generation ground-based gravitational-wave detectors *Astrophys. J. Lett.* **933** L41

[36] Farr W M and Chatziioannou K 2020 A population-informed mass estimate for pulsar J0740+6620 *Res. Notes Am. Astron. Soc.* **4** 65
[37] Akmal A, Pandharipande V R and Ravenhall D G 1998 The equation of state of nucleon matter and neutron star structure *Phys. Rev.* C **58** 1804
[38] Abbott R *et al* (LIGO Scientific, KAGRA and VIRGO) 2021 Observation of gravitational waves from two neutron star–black hole coalescences *Astrophys. J. Lett.* **915** L5
[39] Vallisneri M 2008 Use and abuse of the Fisher information matrix in the assessment of gravitational-wave parameter-estimation prospects *Phys. Rev.* D **77** 042001
[40] Balasubramanian R, Sathyaprakash B S and Dhurandhar S V 1996 Gravitational waves from coalescing binaries: detection strategies and Monte Carlo estimation of parameters *Phys. Rev.* D **53** 3033
Balasubramanian R, Sathyaprakash B S and Dhurandhar S V 1996 *Phys. Rev.* D **54** 1860 (erratum)
[41] Magee R and Borhanian S 2022 Observing scenarios for the next decade of early warning detection of binary neutron stars *Astrophys. J.* **935** 139
[42] Rodriguez C L, Farr B, Farr W M and Mandel I 2013 Inadequacies of the fisher information matrix in gravitational-wave parameter estimation *Phys. Rev.* D **88** 084013
[43] Mandel I, Berry C P L, Ohme F, Fairhurst S and Farr W M 2014 Parameter estimation on compact binary coalescences with abruptly terminating gravitational waveforms *Class. Quantum Grav.* **31** 155005
[44] Dupletsa U, Harms J, Ng K K Y, Tissino J, Santoliquido F and Cozzumbo A 2024 Validating prior-informed Fisher-matrix analyses against GWTC Data (arXiv:2404.16103 [gr-qc])
[45] Borhanian S 2021 GWBENCH: a novel Fisher information package for gravitational-wave benchmarking *Class. Quantum Grav.* **38** 175014
[46] LIGO Scientific Collaboration 2018 LIGO algorithm library—LALSuite, free software (GPL) (available at: https://doi.org/10.7935/GT1W-FZ16)
[47] García-Quirós C, Colleoni M, Husa S, Estellés H, Pratten G, Ramos-Buades A, Mateu-Lucena M and Jaume R 2020 Multimode frequency-domain model for the gravitational wave signal from nonprecessing black-hole binaries *Phys. Rev.* D **102** 064002
[48] Dietrich T, Samajdar A, Khan S, Johnson-McDaniel N K, Dudi R and Tichy W 2019 Improving the NRTidal model for binary neutron star systems *Phys. Rev.* D **100** 044003
[49] Gupta I, Borhanian S, Dhani A, Chattopadhyay D, Kashyap R, Villar V A and Sathyaprakash B S 2023 Neutron star-black hole mergers in next generation gravitational-wave observatories *Phys. Rev.* D **107** 124007
[50] Borhanian S, Dhani A, Gupta A, Arun K G and Sathyaprakash B S 2020 Dark sirens to resolve the Hubble–Lemaître tension *Astrophys. J. Lett.* **905** L28
[51] Graham M J *et al* 2020 Candidate electromagnetic counterpart to the binary black hole merger gravitational wave event S190521g *Phys. Rev. Lett.* **124** 251102
[52] Gupta I 2024 Inferring small neutron star spins with neutron star-black hole mergers (arXiv:2402.07075 [astro-ph.HE])
[53] LSST Rubin observatory system & lsst survey key numbers (available at: www.lsst.org/scientists/keynumbers) (Accessed 3 October 2022)
[54] Ivezić v *et al* (LSST) 2019 LSST: from science drivers to reference design and anticipated data products *Astrophys. J.* **873** 111
[55] Scaramella R *et al* (Euclid) 2022 Euclid preparation - I. The Euclid wide survey *Astron. Astrophys.* **662** A112
[56] Rau A *et al* 2013 The hot and energetic universe: the wide field imager (WFI) for Athena+ (arXiv:1308.6785)
[57] Hounsell R *et al* 2018 Simulations of the WFIRST supernova survey and forecasts of cosmological constraints *Astrophys. J.* **867** 23
[58] Chase E A, O'Connor B, Fryer C L, Troja E, Korobkin O, Wollaeger R T, Ristic M, Fontes C J, Hungerford A L and Herring A M 2022 Kilonova detectability with wide-field instruments *Astrophys. J.* **927** 163
[59] Murphy E J *et al* 2018 The ngVLA Science Case and Associated Science Requirements *Science With a Next Generation Very Large Array* (*Astronomical Society of the Pacific Conference Series* vol 517) ed E Murphy p 3
[60] NASA's High Energy Astrophysics Science Archive Research Center Chandra x-ray observatory: mission characteristics (available at: https://heasarc.gsfc.nasa.gov/docs/chandra/chandra.html) (Accessed 3 October 2022)

[61] Gaskin J A *et al* 2019 Lynx x-ray observatory: an overview *J. Astron. Teles. Instrum. Syst.* **5** 021001
[62] Burrows D N *et al* 2000 Swift x-ray telescope *Proc. SPIE* **4140** 64–75
[63] Bundy K *et al* 2019 FOBOS: a next-generation spectroscopic facility at the W. M. Keck observatory (arXiv:1907.07195)
[64] Johns M, McCarthy P, Raybould K, Bouchez A, Farahani A, Filgueira J, Jacoby G, Shectman S and Sheehan M 2012 Giant magellan telescope: overview *Proc. SPIE* **8444** 84441H
[65] Perley R A, Chandler C J, Butler B J and Wrobel J M 2011 The expanded very large array: a new telescope for new science *Astrophys. J.* **739** L1
[66] Ronchini S, Branchesi M, Oganesyan G, Banerjee B, Dupletsa U, Ghirlanda G, Harms J, Mapelli M and Santoliquido F 2022 Perspectives for multimessenger astronomy with the next generation of gravitational-wave detectors and high-energy satellites *Astron. Astrophys.* **665** A97
[67] Maggiore M *et al* 2020 Science case for the Einstein telescope *J. Cosmol. Astropart. Phys.* JCAP03(2020)050
[68] Kalogera V *et al* 2021 The next generation global gravitational wave observatory: the science book (arXiv:2111.06990 [gr-qc])
[69] Bailes M *et al* 2021 Gravitational-wave physics and astronomy in the 2020s and 2030s *Nature Rev. Phys.* **3** 344
[70] Zevin M, Bavera S S, Berry C P L, Kalogera V, Fragos T, Marchant P, Rodriguez C L, Antonini F, Holz D E and Pankow C 2021 One channel to rule them all? constraining the origins of binary black holes using multiple formation pathways *Astrophys. J.* **910** 152
[71] Wong K W K, Breivik K, Kremer K and Callister T 2021 Joint constraints on the field-cluster mixing fraction, common envelope efficiency and globular cluster radii from a population of binary hole mergers via deep learning *Phys. Rev.* D **103** 083021
[72] Stevenson S and Clarke T A 2022 Constraints on the contributions to the observed binary black hole population from individual evolutionary pathways in isolated binary evolution *Mon. Not. R. Astron. Soc.* **517** 4034
[73] Godfrey J, Edelman B and Farr B 2023 Cosmic cousins: identification of a subpopulation of binary black holes consistent with isolated binary evolution (arXiv:2304.01288)
[74] Fryer C L, Belczynski K, Wiktorowicz G, Dominik M, Kalogera V and Holz D E 2012 Compact remnant mass function: dependence on the explosion mechanism and metallicity *Astrophys. J.* **749** 91
[75] Fryer C L, Olejak A and Belczynski K 2022 The effect of supernova convection on neutron star and black hole masses *Astrophys. J.* **931** 94
[76] Olejak A, Fryer C L, Belczynski K and Baibhav V 2022 The role of supernova convection for the lower mass gap in the isolated binary formation of gravitational wave sources *Mon. Not. R. Astron. Soc.* **516** 2252
[77] van Son L A C, de Mink S E, Renzo M, Justham S, Zapartas E, Breivik K, Callister T, Farr W M and Conroy C 2022 No Peaks without valleys: the stable mass transfer channel for gravitational-wave sources in light of the neutron star-black hole mass gap *Astrophys. J.* **940** 184
[78] Schneider F R N, Podsiadlowski P and Laplace E 2023 Bimodal black-hole mass distribution and chirp masses of binary black-hole mergers (arXiv:2305.02380)
[79] Fryer C 2023 GW compact remnant mass constraints as probes of the supernova engine (available at: https://dcc.cosmicexplorer.org/CE-P2300002/public)
[80] Choksi N, Volonteri M, Colpi M, Gnedin O Y and Li H 2019 The star clusters that make black hole binaries across cosmic time *Astrophys. J.* **873** 100
[81] Safarzadeh M, Berger E, Ng K K Y, Chen H-Y, Vitale S, Whittle C and Scannapieco E 2019 Measuring the delay time distribution of binary neutron stars. II. Using the redshift distribution from third-generation gravitational wave detectors network *Astrophys. J. Lett.* **878** L13
[82] Chruślińska M 2022 Chemical evolution of the Universe and its consequences for gravitational-wave astrophysics (arXiv:2206.10622)
[83] Woosley S E 2017 Pulsational pair-instability supernovae *Astrophys. J.* **836** 244
[84] van Son L, Broekgaarden F, Vitale S and Callister T 2023 What we need from XG observatories to unveil the birth, life and death of massive stars—Part 3: stellar death (available at: https://dcc.cosmicexplorer.org/CE-P2300016/public)
[85] Kimball C *et al* 2021 Evidence for hierarchical black hole mergers in the second LIGO–Virgo gravitational wave catalog *Astrophys. J. Lett.* **915** L35

[86] Gerosa D and Fishbach M 2021 Hierarchical mergers of stellar-mass black holes and their gravitational-wave signatures *Nat. Astron.* **5** 749
[87] Greene J E, Strader J and Ho L C 2020 Intermediate-mass black holes *Ann. Rev. Astron. Astrophys.* **58** 257
[88] Mishra T, Szczepanczyk M, Klimenko S, Bhaumik S, Bartos I, Fulda P and Gayathri V 2023 Probing black hole growth with intermediate mass black holes (available at: https://dcc.cosmicexplorer.org/CE-P2300011/public)
[89] Carr B J and Hawking S W 1974 Black holes in the early universe *Mon. Not. R. Astron. Soc.* **168** 399
[90] Bird S, Cholis I, Mu noz J B, Ali-Haïmoud Y, Kamionkowski M, Kovetz E D, Raccanelli A and Riess A G 2016 Did LIGO detect dark matter? *Phys. Rev. Lett.* **116** 201301
[91] Raidal M, Spethmann C, Vaskonen V and Veermäe H 2019 Formation and evolution of primordial black hole binaries in the early universe *J. Cosmol. Astropart. Phys.* JCAP02(2019)018
[92] Franciolini G, Iacovelli F, Mancarella M, Maggiore M, Pani P and Riotto A 2023 Searching for primordial black holes with the Einstein telescope: impact of design and systematics *Phys. Rev.* D **108** 043506
[93] Santoliquido F, Mapelli M, Iorio G, Costa G, Glover S C O, Hartwig T, Klessen R S and Merli L 2023 Binary black hole mergers from Population III stars: uncertainties from star formation and binary star properties *Mon. Not. R. Astron. Soc.* **524** 307
[94] Madau P and Rees M J 2001 Massive black holes as population III remnants *Astrophys. J. Lett.* **551** L27
[95] Volonteri M and Bellovary J 2012 Black holes in the early Universe *Rept. Prog. Phys.* **75** 124901
[96] Natarajan P 2014 Seeds to monsters: tracing the growth of black holes in the Universe *Gen. Relativ. Gravit.* **46** 1702
[97] Valiante R, Colpi M, Schneider R, Mangiagli A, Bonetti M, Cerini G, Fairhurst S, Haardt F, Mills C and Sesana A 2020 Unveiling early black hole growth with multifrequency gravitational wave observations *Mon. Not. R. Astron. Soc.* **500** 4095
[98] Li L-X and Paczynski B 1998 Transient events from neutron star mergers *Astrophys. J. Lett.* **507** L59
[99] Goodman J 1986 Are gamma-ray bursts optically thick? *Astrophys. J. Lett.* **308** L47
[100] Eichler D, Livio M, Piran T and Schramm D N 1989 Nucleosynthesis, neutrino bursts and gamma-rays from coalescing neutron stars *Nature* **340** 126
[101] Kobayashi S and Mészáros P 2003 Gravitational radiation from gamma-ray burst progenitors *Astrophys. J.* **589** 861
[102] Belczynski K, Perna R, Bulik T, Kalogera V, Ivanova N and Lamb D Q 2006 A study of compact object mergers as short gamma-ray burst progenitors *Astrophys. J.* **648** 1110
[103] Nakar E and Piran T 2011 Detectable radio flares following gravitational waves from mergers of binary neutron stars *Nature* **478** 82
[104] Piran T, Nakar E and Rosswog S 2013 The electromagnetic signals of compact binary mergers *Mon. Not. R. Astron. Soc.* **430** 2121
[105] Metzger B D 2020 Kilonovae *Living Rev. Relativ.* **23** 1
[106] Kyutoku K, Shibata M and Taniguchi K 2021 Coalescence of black hole–neutron star binaries *Living Rev. Relativ.* **24** 5
[107] Abbott B P (LIGO Scientific Collaboration and Virgo Collaboration) 2017 GW170817: observation of gravitational waves from a binary neutron star inspiral *Phys. Rev. Lett.* **119** 161101
[108] Abbott B P *et al* (LIGO Scientific Collaboration and Virgo Collaboration) 2017 Multi-messenger observations of a binary neutron star merger *Astrophys. J.* **848** L12
[109] Abbott B P *et al* (LIGO Scientific Collaboration and Virgo Collaboration) 2017 Gravitational waves and gamma-rays from a binary neutron star merger: GW170817 and GRB 170817A *Astrophys. J. Lett.* **848** L13
[110] Arcavi I *et al* 2017 Optical emission from a kilonova following a gravitational-wave-detected neutron-star merger *Nature* **551** 64
[111] Coulter D A *et al* 2017 Swope Supernova Survey 2017a (SSS17a), the optical counterpart to a gravitational wave source *Science* **358** 1556
[112] Drout M R *et al* 2017 Light curves of the neutron star merger GW170817/SSS17a: Implications for r-process nucleosynthesis *Science* **358** 1570
[113] Goldstein A *et al* 2017 An ordinary short gamma-ray burst with extraordinary implications: Fermi-GBM detection of GRB 170817A *Astrophys. J.* **848** L14

[114] Fong W *et al* 2017 The electromagnetic counterpart of the binary neutron star merger LIGO/Virgo GW170817. VIII. A comparison to cosmological short-duration gamma-ray bursts *Astrophys. J.* **848** L23
[115] Hallinan G *et al* 2017 A radio counterpart to a neutron star merger *Science* **358** 1579
[116] Haggard D, Nynka M, Ruan J J, Kalogera V, Cenko S B, Evans P and Kennea J A 2017 A deep chandra x-ray study of neutron star coalescence GW170817 *Astrophys. J.* **848** L25
[117] Kasliwal M M *et al* 2017 Illuminating gravitational waves: a concordant picture of photons from a neutron star merger *Science* **358** 1559
[118] Margutti R *et al* 2017 The electromagnetic counterpart of the binary neutron star merger LIGO/Virgo GW170817. V. Rising x-ray emission from an Off-axis Jet *Astrophys. J.* **848** L20
[119] Smartt S J *et al* 2017 A kilonova as the electromagnetic counterpart to a gravitational-wave source *Nature* **551** 75
[120] Pian E *et al* 2017 Spectroscopic identification of r-process nucleosynthesis in a double neutron-star merger *Nature* **551** 67
[121] Troja E *et al* 2017 The x-ray counterpart to the gravitational-wave event GW170817 *Nature* **551** 71
[122] Villar V A *et al* 2017 The combined ultraviolet, optical and near-infrared light curves of the kilonova associated with the binary neutron star merger GW170817: unified data set, analytic models and physical implications *Astrophys. J.* **851** L21
[123] Lazzati D, Perna R, Morsony B J, Lopez-Camara D, Cantiello M, Ciolfi R, Giacomazzo B and Workman J C 2018 Late time afterglow observations reveal a collimated relativistic jet in the ejecta of the binary neutron star merger GW170817 *Phys. Rev. Lett.* **120** 241103
[124] Mooley K P, Deller A T, Gottlieb O, Nakar E, Hallinan G, Bourke S, Frail D A, Horesh A, Corsi A and Hotokezaka K 2018 Superluminal motion of a relativistic jet in the neutron-star merger GW170817 *Nature* **561** 355
[125] Lazzati D 2020 Short duration gamma-ray bursts and their outflows in light of GW170817 *Front. Astron. Space Sci.* **7** 78
[126] Andreoni I *et al* 2022 Target-of-opportunity observations of gravitational-wave events with Vera C. Rubin observatory *Astrophys. J. Suppl.* **260** 18
[127] Petrov P, Singer L P, Coughlin M W, Kumar V, Almualla M, Anand S, Bulla M, Dietrich T, Foucart F and Guessoum N 2022 Data-driven expectations for electromagnetic counterpart searches based on LIGO/Virgo public alerts *Astrophys. J.* **924** 54
[128] Margalit B and Metzger B D 2019 The multi-messenger matrix: the future of neutron star merger constraints on the nuclear equation of state *Astrophys. J.* **880** L15
[129] Sarin N and Lasky P D 2021 The evolution of binary neutron star post-merger remnants: a review *Gen. Relativ. Grav.* **53** 59
[130] Hotokezaka K, Nissanke S, Hallinan G, Lazio T J W, Nakar E and Piran T 2016 Radio counterparts of compact binary mergers detectable in gravitational waves: a simulation for an optimized survey *Astrophys. J.* **831** 190
[131] Troja E, Rosswog S and Gehrels N 2010 Precursors of short gamma-ray bursts *Astrophys. J.* **723** 1711
[132] Rowlinson A and Anderson G E 2019 Constraining coherent low-frequency radio flares from compact binary mergers *Mon. Not. R. Astron. Soc.* **489** 3316
[133] Curtin A P *et al* 2022 Limits on fast radio burst-like counterparts to gamma-ray bursts using CHIME/FRB (arXiv:2208.00803)
[134] Moroianu A, Wen L, James C W, Ai S, Kovalam M, Panther F H and Zhang B 2023 An assessment of the association between a fast radio burst and binary neutron star merger *Nat. Astron.* **7** 579–89
[135] Sachdev S *et al* 2020 An early-warning system for electromagnetic follow-up of gravitational-wave events *Astrophys. J. Lett.* **905** L25
[136] Banerjee B *et al* 2023 Pre-merger alert to detect the very-high-energy prompt emission from binary neutron-star mergers: Einstein telescope and cherenkov telescope array synergy *Astron. Astrophys.* **678** A126
[137] Sabatucci A, Benhar O, Maselli A and Pacilio C 2022 Sensitivity of neutron star observations to three-nucleon forces *Phys. Rev.* D **106** 083010
[138] Rose H, Kunert N, Dietrich T, Pang P T H, Smith R, Van Den Broeck C, Gandolfi S and Tews I 2023 Revealing the strength of three-nucleon interactions with the proposed Einstein Telescope *Phys. Rev.* C **108** 025811

[139] Chatziioannou K, Haster C-J and Zimmerman A 2018 Measuring the neutron star tidal deformability with equation-of-state-independent relations and gravitational waves *Phys. Rev.* D **97** 104036
[140] Yagi K and Yunes N 2017 Approximate universal relations for neutron stars and quark stars *Phys. Rept.* **681** 1
[141] Kashyap R, Dhani A and Sathyaprakash B 2022 Systematic errors due to quasiuniversal relations in binary neutron stars and their correction for unbiased model selection *Phys. Rev.* D **106** 123001
[142] Huxford R, Kashyap R, Borhanian S, Dhani A and Sathyaprakash B S 2023 The accuracy of neutron star radius measurement with the next generation of terrestrial gravitational-wave observatories (arXiv:2307.05376 [gr-qc])
[143] Dietrich T, Radice D, Bernuzzi S, Zappa F, Perego A, Brügmann B, Chaurasia S V, Dudi R, Tichy W and Ujevic M 2018 CoRe database of binary neutron star merger waveforms *Class. Quantum Grav.* **35** 24LT01
[144] Essick R, Vitale S and Evans M 2017 Frequency-dependent responses in third generation gravitational-wave detectors *Phys. Rev.* D **96** 084004
[145] Glampedakis K and Gualtieri L 2018 Gravitational waves from single neutron stars: an advanced detector era survey *Astrophys. Space Sci. Libr.* **457** 673
[146] Kalogera V *et al* 2019 The yet-unobserved multi-messenger gravitational-wave Universe (arXiv:1903.09224 [astro-ph.HE])
[147] Riles K 2023 Searches for continuous-wave gravitational radiation *Living Rev. Relativ.* **26** 3
[148] Wette K 2023 Searches for continuous gravitational waves from neutron stars: a twenty-year retrospective (arXiv:2305.07106 [gr-qc])
[149] Shklovskii I S 1969 Possible causes of the secular increase in pulsar periods *Astron. Zh. (Soviet Astron.)* **46** 715
[150] Andersson N 1998 A New class of unstable modes of rotating relativistic stars *Astrophys. J.* **502** 708
[151] Lindblom L, Owen B J and Morsink S M 1998 Gravitational radiation instability in hot young neutron stars *Phys. Rev. Lett.* **80** 4843
[152] Dreissigacker C, Prix R and Wette K 2018 Fast and accurate sensitivity estimation for continuous-gravitational-wave searches *Phys. Rev.* D **98** 084058
[153] Jaranowski P, Krolak A and Schutz B F 1998 Data analysis of gravitational - wave signals from spinning neutron stars. 1. The Signal and its detection *Phys. Rev.* D **58** 063001
[154] Bildsten L 1998 Gravitational radiation and rotation of accreting neutron stars *Astrophys. J.* **501** L89
[155] Hutchins T J and Jones D I 2023 Gravitational radiation from thermal mountains on accreting neutron stars: sources of temperature non-axisymmetry *Mon. Not. R. Astron. Soc.* **522** 226
[156] Melatos A and Payne D J B 2005 Gravitational radiation from an accreting millisecond pulsar with a magnetically confined mountain *Astrophys. J.* **623** 1044
[157] Andersson N, Kokkotas K D and Stergioulas N 1999 On the relevance of the r mode instability for accreting neutron stars and white dwarfs *Astrophys. J.* **516** 307
[158] Papaloizou J and Pringle J E 1978 Gravitational radiation and the stability of rotating stars *Mon. Not. R. Astron. Soc.* **184** 501
[159] Wagoner R V 1984 Gravitational radiation from accreting neutron stars *Astrophys. J.* **278** 345
[160] Watts A, Krishnan B, Bildsten L and Schutz B F 2008 Detecting gravitational wave emission from the known accreting neutron stars *Mon. Not. R. Astron. Soc.* **389** 839
[161] Abbott R *et al* (LIGO Scientific, KAGRA and VIRGO) 2022 Model-based cross-correlation search for gravitational waves from the low-mass x-ray binary scorpius X-1 in LIGO O3 data *Astrophys. J. Lett.* **941** L30
[162] Owen B J, Rajbhandari B and Pearce A 2023 Detectability of continuous gravitational waves and starquakes from the near future to the era of cosmic explorer (in preparation)
[163] Manchester R N 2017 Millisecond pulsars, their evolution and applications *J. Astrophys. Astron.* **38** 42
[164] Woan G, Pitkin M D, Haskell B, Jones D I and Lasky P D 2018 Evidence for a minimum ellipticity in millisecond pulsars *Astrophys. J. Lett.* **863** L40
[165] Palomba C 2000 Pulsars ellipticity revised *Astron. Astrophys.* **354** 163
[166] Vigelius M and Melatos A 2009 Resistive relaxation of a magnetically confined mountain on an accreting neutron star *Mon. Not. R. Astron. Soc.* **395** 1985

[167] Manchester R N, Hobbs G B, Teoh A and Hobbs M 2005 The Australia telescope national facility pulsar catalogue *Astron. J.* **129** 1993
[168] Smits R, Kramer M, Stappers B, Lorimer D R, Cordes J and Faulkner A 2009 Pulsar searches and timing with the square kilometre array *Astron. Astrophys.* **493** 1161
[169] Beasley A *et al* 2019 Multiwavelength astrophysics in the era of the ngVLA and the US ELT program *Bull. Am. Astron. Soc.* **51** 88
[170] Pagliaro G, Alessandra Papa M, Ming J, Lian J, Tsuna D, Maraston C and Thomas D 2023 Continuous gravitational waves from Galactic neutron stars: demography, detectability and prospects (arXiv:2303.04714)
[171] Jaranowski P and Krolak A 1999 Data analysis of gravitational wave signals from spinning neutron stars. 2. Accuracy of estimation of parameters *Phys. Rev.* D **59** 063003
[172] Jones D I 2021 Learning from the frequency content of continuous gravitational wave signals (arXiv:2111.08561 [astro-ph.HE])
[173] Idrisy A, Owen B J and Jones D I 2015 *R*-mode frequencies of slowly rotating relativistic neutron stars with realistic equations of state *Phys. Rev.* D **91** 024001
[174] Sieniawska M, Jones D I and Miller A L 2023 Measuring neutron star distances and properties with gravitational-wave parallax *Mon. Not. R. Astron. Soc.* **521** 1924
[175] Lu N, Wette K, Scott S M and Melatos A 2022 Inferring neutron star properties with continuous gravitational waves (arXiv:2209.10981 [gr-qc])
[176] Owen B J 2005 Maximum elastic deformations of compact stars with exotic equations of state *Phys. Rev. Lett.* **95** 211101
[177] Arras P, Flanagan E E, Morsink S M, Schenk A K, Teukolsky S A and Wasserman I 2003 Saturation of the R mode instability *Astrophys. J.* **591** 1129
[178] Srivastava V, Ballmer S, Brown D A, Afle C, Burrows A, Radice D and Vartanyan D 2019 Detection prospects of core-collapse supernovae with supernova-optimized third-generation gravitational-wave detectors *Phys. Rev.* D **100** 043026
[179] Szczepańczyk M and Zanolin M 2022 Gravitational waves from a core-collapse supernova: perspectives with detectors in the late 2020s and early 2030s *Galaxies* **10** 70
[180] Radice D, Morozova V, Burrows A, Vartanyan D and Nagakura H 2019 Characterizing the gravitational wave signal from core-collapse supernovae *Astrophys. J. Lett.* **876** L9
[181] Ott C D, Reisswig C, Schnetter E, O'Connor E, Sperhake U, Loffler F, Diener P, Abdikamalov E, Hawke I and Burrows A 2011 Dynamics and gravitational wave signature of collapsar formation *Phys. Rev. Lett.* **106** 161103
[182] Abdikamalov E, Gossan S, DeMaio A M and Ott C D 2014 Measuring the angular momentum distribution in core-collapse supernova progenitors with gravitational waves *Phys. Rev.* D **90** 044001
[183] Takiwaki T and Kotake K 2018 Anisotropic emission of neutrino and gravitational-wave signals from rapidly rotating core-collapse supernovae *Mon. Not. R. Astron. Soc.* **475** L91
[184] Siegel D M, Agarwal A, Barnes J, Metzger B D, Renzo M and Villar V A 2022 Super-kilonovae" from massive collapsars as signatures of black hole birth in the pair-instability mass gap *Astrophys. J.* **941** 100
[185] Gottlieb O, Nagakura H, Tchekhovskoy A, Natarajan P, Ramirez-Ruiz E, Banagiri S, Jacquemin-Ide J, Kaaz N and Kalogera V 2022 Jetted and turbulent stellar deaths: new LVK-detectable gravitational wave sources (arXiv:2209.09256)
[186] Moragues J, Modafferi L M, Tenorio R and Keitel D 2023 Prospects for detecting transient quasi-monochromatic gravitational waves from glitching pulsars with current and future detectors *Mon. Not. R. Astron. Soc.* **519** 5161
[187] Corsi A and Owen B J 2011 Maximum gravitational-wave energy emissible in magnetar flares *Phys. Rev.* D **83** 104014
[188] Abbott B P *et al* (LIGO Scientific and Virgo) 2019 Search for transient gravitational-wave signals associated with magnetar bursts during advanced LIGO's second observing run *Astrophys. J.* **874** 163
[189] Andersson N and Kokkotas K D 1998 Towards gravitational wave asteroseismology *Mon. Not. R. Astron. Soc.* **299** 1059
[190] Ho W C G, Jones D I, Andersson N and Espinoza C M 2020 Gravitational waves from transient neutron star f -mode oscillations *Phys. Rev.* D **101** 103009
[191] Melatos A, Douglass J A and Simula T P 2015 Persistent gravitational radiation from glitching pulsars *Astrophys. J.* **807** 132

[192] Yunes N and Pretorius F 2009 Fundamental theoretical bias in gravitational wave astrophysics and the parameterized post-Einsteinian framework *Phys. Rev.* D **80** 122003
[193] Yunes N, Yagi K and Pretorius F 2016 Theoretical physics implications of the binary black-hole mergers GW150914 and GW151226 *Phys. Rev.* D **94** 084002
[194] Bhagwat S, Pacilio C, Pani P and Mapelli M 2023 Landscape of stellar-mass black-hole spectroscopy with third-generation gravitational-wave detectors *Phys. Rev.* D **108** 043019
[195] Perkins S E, Yunes N and Berti E 2021 Probing fundamental physics with gravitational waves: the next generation *Phys. Rev.* D **103** 044024
[196] Gupta A, Datta S, Kastha S, Borhanian S, Arun K G and Sathyaprakash B S 2020 Multiparameter tests of general relativity using multiband gravitational-wave observations *Phys. Rev. Lett.* **125** 201101
[197] Verde L, Treu T and Riess A G 2019 Tensions between the early and the late Universe *Nat. Astron.* **3** 891
[198] Di Valentino E, Mena O, Pan S, Visinelli L, Yang W, Melchiorri A, Mota D F, Riess A G and Silk J 2021 In the realm of the Hubble tension—a review of solutions *Class. Quantum Grav.* **38** 153001
[199] Riess A G *et al* 2022 A comprehensive measurement of the local value of the hubble constant with 1 km s^{-1} Mpc^{-1} uncertainty from the hubble space telescope and the SH0ES team *Astrophys. J. Lett.* **934** L7
[200] Aghanim N *et al* (Planck Collaboration) 2020 Planck 2018 results. VI. Cosmological parameters *Astron. Astrophys.* **641** A6
Aghanim N *et al* (Planck Collaboration) 2021 *Astron. Astrophys.* **652** C4 (erratum)
[201] Sharon A, Kushnir D, Yuan W, Macri L and Riess A 2023 Reassessing the Constraints from SH0ES extragalactic cepheid amplitudes on systematic blending bias (arXiv:2305.14435 [astro-ph.CO])
[202] Abbott B P *et al* (LIGO Scientific and Virgo) 2017 Estimating the contribution of dynamical ejecta in the kilonova associated with GW170817 *Astrophys. J. Lett.* **850** L39
[203] Abbott B P *et al* (LIGO Scientific, Virgo, 1M2H, Dark Energy Camera GW-E, DES, DLT40, Las Cumbres Observatory, VINROUGE and MASTER) 2017 A gravitational-wave standard siren measurement of the Hubble constant *Nature* **551** 85
[204] Schutz B F 1986 Determining the hubble constant from gravitational wave observations *Nature* **323** 310
[205] Palmese A, Bom C R, Mucesh S and Hartley W G 2023 A standard siren measurement of the hubble constant using gravitational-wave events from the first three LIGO/Virgo observing runs and the DESI legacy survey *Astrophys. J.* **943** 56
[206] Nishizawa A 2017 Measurement of hubble constant with stellar-mass binary black holes *Phys. Rev.* **D96** 101303
[207] Gupta I 2023 Using grey sirens to resolve the Hubble–Lemaître tension *Mon. Not. R. Astron. Soc.* **524** 3537
[208] Messenger C and Read J 2012 Measuring a cosmological distance-redshift relationship using only gravitational wave observations of binary neutron star coalescences *Phys. Rev. Lett.* **108** 091101
[209] Messenger C, Takami K, Gossan S, Rezzolla L and Sathyaprakash B S 2014 Source redshifts from gravitational-wave observations of binary neutron star mergers *Phys. Rev.* X **4** 041004
[210] Li T G F, Del Pozzo W and Messenger C 2015 Measuring the redshift of standard sirens using the neutron star deformability *13th Marcel Grossmann Meeting on Recent Developments in Theoretical and Experimental General Relativity, Astrophysics and Relativistic Field Theories* pp 2019–21
[211] Del Pozzo W, Li T G F and Messenger C 2017 Cosmological inference using only gravitational wave observations of binary neutron stars *Phys. Rev.* D **95** 043502
[212] Chatterjee D, Hegade KR A, Holder G, Holz D E, Perkins S, Yagi K and Yunes N 2021 Cosmology with love: measuring the hubble constant using neutron star universal relations *Phys. Rev.* D **104** 083528
[213] Shiralilou B, Raaiijmakers G, Duboeuf B, Nissanke S, Foucart F, Hinderer T and Williamson A 2022 Measuring hubble constant with dark neutron star-black hole mergers (arXiv:2207.11792 [astro-ph.CO])
[214] Ghosh T, Biswas B and Bose S 2022 Simultaneous inference of neutron star equation of state and the Hubble constant with a population of merging neutron stars *Phys. Rev.* D **106** 123529

[215] Wang B, Zhu Z, Li A and Zhao W 2020 Comprehensive analysis of the tidal effect in gravitational waves and implication for cosmology *Astrophys. J. Suppl.* **250** 6
[216] Jin S-J, Li T-N, Zhang J-F and Zhang X 2022 Precisely measuring the Hubble constant and dark energy using only gravitational-wave dark sirens (arXiv:2202.11882 [gr-qc])
[217] Heavens A F, Seikel M, Nord B D, Aich M, Bouffanais Y, Bassett B A and Hobson M P 2014 Generalized fisher matrices *Mon. Not. R. Astron. Soc.* **445** 1687
[218] Wierda A R A C, Wempe E, Hannuksela O A, Koopmans L e V E and Van Den Broeck C 2021 Beyond the detector horizon: forecasting gravitational-wave strong lensing *Astrophys. J.* **921** 154
[219] Abbott R *et al* (LIGO Scientific and VIRGO) 2021 Search for lensing signatures in the gravitational-wave observations from the first half of LIGO–Virgo's third observing run *Astrophys. J.* **923** 14
[220] Abbott R *et al* (LIGO Scientific, VIRGO and KAGRA) 2023 Search for gravitational-lensing signatures in the full third observing run of the LIGO-Virgo network (arXiv:2304.08393 [gr-qc])
[221] Sanidas S A, Battye R A and Stappers B W 2012 Constraints on cosmic string tension imposed by the limit on the stochastic gravitational wave background from the European pulsar timing array *Phys. Rev.* D **85** 122003
[222] Easther R, Giblin J, Giblin Jr J T and Lim E A 2007 Gravitational wave production at the end of inflation *Phys. Rev. Lett.* **99** 221301
[223] Allen B and Romano J D 1999 Detecting a stochastic background of gravitational radiation: Signal processing strategies and sensitivities *Phys. Rev.* D **59** 102001
[224] Romano J D and Cornish N J 2017 Detection methods for stochastic gravitational-wave backgrounds: a unified treatment *Living Rev. Relativ.* **20** 2
[225] Flanagan E E 1993 The Sensitivity of the laser interferometer gravitational wave observatory (LIGO) to a stochastic background and its dependence on the detector orientations *Phys. Rev.* D **48** 2389
[226] Christensen N 2019 Stochastic gravitational wave backgrounds *Rept. Prog. Phys.* **82** 016903
[227] Thrane E and Romano J D 2013 Sensitivity curves for searches for gravitational-wave backgrounds *Phys. Rev.* D **88** 124032
[228] Aasi J *et al* (LIGO Scientific and VIRGO) 2015 Searching for stochastic gravitational waves using data from the two colocated LIGO Hanford detectors *Phys. Rev.* D **91** 022003
[229] Sharma A and Harms J 2020 Searching for cosmological gravitational-wave backgrounds with third-generation detectors in the presence of an astrophysical foreground *Phys. Rev.* D **102** 063009
[230] Biscoveanu S, Talbot C, Thrane E and Smith R 2020 Measuring the primordial gravitational-wave background in the presence of astrophysical foregrounds *Phys. Rev. Lett.* **125** 241101
[231] Renzini A I, Goncharov B, Jenkins A C and Meyers P M 2022 Stochastic gravitational-wave backgrounds: current detection efforts and future prospects *Galaxies* **10** 34
[232] Zhou B, Reali L, Berti E, Çalışkan M, Creque-Sarbinowski C, Kamionkowski M and Sathyaprakash B S 2022 Subtracting compact binary foregrounds to search for subdominant gravitational-wave backgrounds in next-generation ground-based observatories (arXiv:2209.01310)
[233] Zhong H, Ormiston R and Mandic V 2023 Detecting cosmological gravitational wave background after removal of compact binary coalescences in future gravitational wave detectors *Phys. Rev.* D **107** 064048
[234] Aalbers J *et al* (LZ) 2022 First dark matter search results from the LUX-ZEPLIN (LZ) experiment (arXiv:2207.03764 [hep-ex])
[235] Akerib D S *et al* (LZ) 2020 Projected WIMP sensitivity of the LUX-ZEPLIN dark matter experiment *Phys. Rev.* D **101** 052002
[236] Akerib D S *et al* (LZ) 2020 The LUX-ZEPLIN (LZ) Experiment *Nucl. Instrum. Methods* A **953** 163047
[237] Arvanitaki A, Dimopoulos S, Dubovsky S, Kaloper N and March-Russell J 2010 String axiverse *Phys. Rev.* D **81** 123530
[238] Arvanitaki A, Baryakhtar M and Huang X 2015 Discovering the QCD axion with black holes and gravitational waves *Phys. Rev.* D **91** 084011
[239] Arvanitaki A, Baryakhtar M, Dimopoulos S, Dubovsky S and Lasenby R 2017 Black hole mergers and the QCD axion at advanced LIGO *Phys. Rev.* D **95** 043001

[240] Brito R, Cardoso V and Pani P 2015 Superradiance: new frontiers in black hole physics *Lect. Notes Phys.* **906** 1
[241] Baryakhtar M, Lasenby R and Teo M 2017 Black hole superradiance signatures of ultralight vectors *Phys. Rev.* D **96** 035019
[242] Siemonsen N and East W E 2020 Gravitational wave signatures of ultralight vector bosons from black hole superradiance *Phys. Rev.* D **101** 024019
[243] Jones D, Sun L, Siemonsen N, East W E, Scott S M and Wette K 2023 Methods and prospects for gravitational wave searches targeting ultralight vector boson clouds around known black holes (arXiv:2305.00401 [gr-qc])
[244] Brito R, Ghosh S, Barausse E, Berti E, Cardoso V, Dvorkin I, Klein A and Pani P 2017 Gravitational wave searches for ultralight bosons with LIGO and LISA *Phys. Rev.* D **96** 064050
[245] Abbott R *et al* (LIGO Scientific, Virgo and KAGRA) 2022 All-sky search for gravitational wave emission from scalar boson clouds around spinning black holes in LIGO O3 data *Phys. Rev.* D **105** 102001
[246] Astone P, Colla A, D'Antonio S, Frasca S and Palomba C 2014 Method for all-sky searches of continuous gravitational wave signals using the frequency-Hough transform *Phys. Rev.* D **90** 042002
[247] Kroupa P 2001 On the variation of the initial mass function *Mon. Not. R. Astron. Soc.* **322** 231
[248] Borhanian S and Sathyaprakash B S 2022 Listening to the Universe with next generation ground-based gravitational-wave detectors (arXiv:2202.11048 [gr-qc])
[249] Gupta I 2023 Cosmic Explorer MPSAC Dataset (available at: https://doi.org/10.5281/zenodo.8087733)